SULFATE REDUCING BIOREACTOR DEPENDENCE ON ORGANIC SUBSTRATES FOR LONG-TERM REMEDIATION OF ACID MINE DRAINAGE: FIELD EXPERIMENTS

by

Evan Robert Walters

B.S., Southern Illinois University, 2011

A Thesis
Submitted in Partial Fulfillment of the Requirements for the
Master of Science Degree

Department of Geology
in the Graduate School
Southern Illinois University Carbondale
December 2013

THESIS APPROVAL

SULFATE REDUCING BIOREACTOR DEPENDENCE ON ORGANIC SUBSTRATES FOR LONG-TERM REMEDIATION OF ACID MINE DRAINAGE: FIELD EXPERIMENTS

By

Evan Robert Walters

A Thesis Submitted in Partial

Fulfillment of the Requirements

for the Degree of

Masters of Science

in the field of Geology

Approved by:

Dr. Liliana Lefticariu, Chair

Dr. Kelly Bender

Dr. Justin Filiberto

Graduate School
Southern Illinois University Carbondale
October 24, 2013

AN ABSTRACT OF THE THESIS OF

Evan Robert Walters, for the Masters of Science degree in Geology, presented on October 24th, 2013 at Southern Illinois University Carbondale.

TITLE: SULFATE REDUCING BIOREACTOR DEPENDENCE ON ORGANIC SUBSTRATES FOR LONG-TERM REMEDIATION OF ACID MINE DRAINAGE: FIELD EXPERIMENTS

MAJOR PROFESSOR: Dr. Liliana Lefticariu

Coal-generated acid mine drainage (AMD) is characterized by low-pH waters with excessive loads of dissolved species such as SO_4, Fe, Al and Mn along with other elements of environmental concern (i.e. Cd, As, Cr, Ni, Pb, Se and Cu). To mitigate this problem, anaerobic sulfate reducing bioreactors (ASRB) have been implemented as a technology for passive treatment systems that utilize low-cost organic substrates to stimulate biologically enhanced contaminant sequestration. Previous work has identified the establishment of diverse microbial communities in which a hierarchal chain of substrate degradation processes is essential in developing sustainable environments to produce long-lived sulfate-reducing microbial (SRM) populations. In this study, to determine the optimal mixture of substrate types, alternating ratios of herbaceous (ie. leaves, grass, spent brewing grains) and ligneous (i.e. maple wood chips and saw dust) reactor matrices were tested.

Five bioreactors along with one control reactor containing only limestone were constructed at the Tab-Simco abandoned mine land (AML) site in southern Illinois, USA. The field experiments were monitored over ~ one year (377 days) to evaluate the physical, geochemical and microbiological parameters which dictate ASRB efficiency in remediation of AMD contaminants. Results from this experiment documented contaminant removal in all reactors. However, the bioreactors established SRM populations that contributed to enhanced removal of SO_4, Fe, and trace metals (i.e. Cu, Cd, Zn, Ni). Geochemical assessment of the

aqueous environments established within the bioreactors suggested multiple pathways of contaminant sequestration. This included the formation of Fe-oxyhydroxide precipitates, adsorption, co-precipitation (e.g. Zn/Ni-Ferrites) and bio-induced sulfide mineralization. Activity of the SRMs was dependent on temperature, with bioreactors exhibiting decreases in both effluent sulfide concentrations and ^{34}S-depletion of sulfate during low-T months (i.e. T < 10°C).

Overall, maximum remediation of dissolved constituents SO_4, Fe, Al and Mn was obtained in the predominantly herbaceous bioreactors. Extrapolation of our results to the full-scale Tab-Simco bioreactor indicated that, over the course of one year, the herbaceous bioreactors would remove ~75,600 kg SO_4, 21,800 kg Fe, 8000 kg Al, and 77 kg Mn. This represents a 21.7 wt%, 41.5 wt%, 9.4 wt% and 81.8 wt% increase in SO_4, Fe, Al and Mn removal over dominantly ligneous bioreactors, respectively. Although the overall Fe removal within the limestone control reactor reached 44.5 mol%; removal of 19.5 mol% SO_4 and 36.9 mol% Al from influent AMD were significantly less when compared to the bioreactors.

These results imply that ASRB technologies are promising in remediation of coal-generated AMD and increasing herbaceous content of bioreactors can significantly enhance contaminant sequestration. However, geochemical results also displayed seasonal variation in redox gradients within our field ASRB's which may induce dissolution of the redox sensitive phases produced within bioreactors. Furthermore, optimal microbial-mediated sulfate reduction may be inhibited by the high surface areas of the abundant Fe/Al-oxyhydroxides which dominate the system. Therefore, to enhance ASRB remediation capacity, future designs must optimize not only the organic carbon substrate but also include a pretreatment phase in which the bulk of dissolved Fe/Al-species are removed from the influent AMD prior to entering the bioreactor.

ACKNOWLEDGMENTS

This research was supported by the U.S. Department of the Interior grant S11AC20018 AS through the Office of Surface Mining Reclamation and Enforcement (OSM) Applied Science Program.

TABLE OF CONTENTS

LIST OF TABLES

LIST OF FIGURES

CHAPTER 1

INTRODUCTION

1.1. Acid Mine Drainage

1.1.1. Abandoned Mine Lands

Prior to Federal laws, the Clean Water Act of 1972 and the Surface Mining Control and Reclamation Act of 1977, discharges from coal mining operations in the U.S. were regulated with varying degrees of success by state governance (IDNR OSMRE, 2013; SMCRA, 1977). Negligent pre-law mining practices have led to widespread abandoned mine lands (AML) and in some cases long-term natural water contamination. In the late 1970's over 200,000 acres of land had been documented as being "affected" by coal mining activities in the state of Illinois alone (FWPCA, 2002). In response to the enactment of the Surface Mining Control and Reclamation Act of 1977, the Illinois Department of Natural Resources Office of Surface Mining Reclamation and Enforcement (IDNR OSMRE) has been working hard to recover the land and aquatic ecosystems that have been negatively impacted by coal-derived pollution. Utilizing various remediation technologies, OSMRE has been able to restore over 9,000 acres of Illinois land, yet at a staggering cost of roughly 146 million dollars (FWPCA, 2002). Additionally, the cost of rehabilitation is not a static value for most AML sites, as many require active treatment or future maintenance which adds to the overall net price. Therefore, it has become prudent to test and develop indelible remediation technologies at an inexpensive initial investment.

1.1.2. Acid Mine Drainage Generation

AML could contribute to high concentrations of pollutants within natural water systems through rapid weathering of newly exposed rock. In most cases, meteoric water flushes through mine refuse piles, open pits, and underground excavation sites advancing weathering rates of inorganic constituents within rocks. Acidic, metal laden water produced by weathering of sulfide-bearing waste rock tailings is commonly known as acid mine drainage (AMD). Specifically, coal-derived AMD occurs from weathering of both inorganic and organic material which promotes the mobilization of anions (e.g., SO_4^{2-}, Cl^-, F^-) and metals (Fe, Al, Cd, Sr, Ni, Cu, Co, Mn, Zn, As) into both ground and surface waters (Freitas et al., 2011; Gammons et al., 2010). Most notably the dissolution of pyrite FeS_2, the most common sulfide mineral associated with coal and waste rocks, causes the mobilization of Fe^{2+} and SO_4^{2-} in high concentrations (Doulati Ardejani et al., 2010; Nieto et al., 2013). Sulfide oxidation is typically the main concern in AMD remediation plans since it can result in pH decreases and the subsequent release of additional trace metals into the aqueous system. The following general reaction describes pyrite oxidation under oxic conditions (Neculita et al., 2007):

$$FeS_{2(s)} + 3.5O_{2(aq)} + H_2O_{(l)} \longrightarrow Fe^{2+} + 2H^+_{(aq)} + 2SO_4^{2-}{}_{(aq)} \quad (1)$$

Further oxidation of the ferrous iron (Fe^{2+}) involves consumption of dissolved oxygen and protons in solution producing the ferric ion (Fe^{3+}) (Wang et al., 2013a):

$$4Fe^{2+} + O_{2(aq)} + 4H^+ \longrightarrow 4Fe^{3+} + 2H_2O_{(l)} \quad (2)$$

Abiotic Fe^{2+}oxidation rates measured in laboratory experiments under low-pH conditions similar to those found in AMD settings have been reported as negligible. However, in natural environments microorganisms such as *Acidothiobacillus ferrooxydans* are exceptionally capable of catalyzing Fe^{2+}oxidation, thus significantly increasing the Fe^{2+} oxidation rates (Wang et al.,

2013a). Consequently, Fe^{3+} in solution can participate in multiple reactions such as hydrolysis (e.g., reaction 3), mineral phase formations/transformations (e.g., reaction 4), as well as acting as a powerful oxidant for additional pyrite dissolution (e.g. reaction 5). Each of these reactions causes an increase in proton (H^+) concentrations in solution resulting in further dissolution of pyrite and mobilization of additional metal contaminants in solution.

Hydrolysis (Daoud & Karamanev, 2006)**:**

$$Fe^{3+} + 2H_2O \longrightarrow Fe(OH)_3 + 3H^+ \quad (3)$$

Jarosite Formation (Daoud & Karamanev, 2006)**:**

$$K^+ + 3Fe^{3+} + 6H_2O + 2HSO_4^{2-} \longrightarrow KFe_3(SO_4)_2(OH)_6 + 8H^+ \quad (4)$$

Pyrite Oxidation (Hubbard et al., 2009; Nordstrom et al., 2000)**:**

$$FeS_2(s) + 14Fe^{3+} + 8H_2O \longrightarrow 15Fe^{2+} + 2SO_4^{2-} + 16H^+ \quad (5)$$

These stoichiometric schemes (reaction 3-5) demonstrate the variety of reactions in which dissolved iron species can participate. In terms of AMD, the overall pyrite oxidation reaction and acid generation is represented by the following generalized equation (Bigham & Nordstrom, 2000):

$$4FeS_2(s) + 15O_2 + 14H_2O \longrightarrow 4Fe(OH)_3 + 8SO_4^{2-} + 16H^+ \quad (6)$$

Since pyrite is a common mineral in Illinois basin coal deposits and found in relatively large quantities in the waste-rock materials, the weathering of pyrite under aerobic conditions can be the dominant source of acidic waters loaded with metals for prolonged periods of time (Nieto et al., 2013). Depending on specific physical and chemical conditions (e.g. pH, Eh, temperature of the waters, and saturation indices (SI) of associated minerals), the dissolved metals can remain in solution and travel far from the original source of contamination (Olías et al., 2006; Olías et al., 2004; Heikkinen, 2002).

1.1.3. Environmental Concerns and Regulations

Proper ecosystem rehabilitation after exploitation of coal and mineral systems has developed into a relevant issue due to modern environmental concerns. The United States Environment Protection Agency (USEPA) recognizes that each AML site presents a unique set of regulatory requirements due to the sites location and AMD geochemistry (USEPA, 2004). Surface waters impacted by AMD have been shown to cause enormous decreases in macro-invertebrate and fish densities when compared to unaffected local waters (Bott et al., 2012). Declines in these freshwater species are attributed to the high concentrations of dissolved sulfate and metals present in the AMD discharges. Additionally, transport and deposition of AMD-associated precipitates throughout natural water systems have been correlated with negatively disturbing local benthic communities (DeNicol & Stapleton, 2002). As a result, to ensure the preservation of natural wild life, it is of utmost importance to design remediation systems that remove high amounts of dissolved contaminants, while retaining AMD associated precipitates from entering adjacent waterways (Gray, 1997).

1.1.4. AMD Remediation Technologies

Preventing direct mobilization of contaminants from the source rock (i.e. coal seam) is always considered as an initial means for the mitigation of AML. Of these “source control” technologies, most involve the inhibition of oxidation and dissolution processes by sealing the reactive surfaces with protective barriers such as anoxic waters, organic substrate or clay minerals (Johnson & Hallberg, 2005). Still these options remain only viable in very specific situations in which hydrogeology, accessibility, and the spatial arrangement of the problematic source rock provides a manageable source control scenario. In many abandoned coal mines in

Illinois, such as in the case of Tab-Simco (Behum et al., 2011), underground flooding and sealing is not a possible option due to the large uncertainty in the location of all shafts and audits (Smith, 2002). Since the potential for source control is not feasible at this AML site, the treatment of its drainage must afford a means to which contaminants expelled from seeps are sequestered in close proximity with minimal propagation into the adjacent creek.

As drainage seeps are characterized by acidic solutions containing high concentrations of dissolved species, undoubtedly long-lived remediation options require prolonged alkalinity production and successive mineral precipitation. To achieve this, treatment options can incorporate abiotic mineralization, biologic mineralization, or both combined into an "active" or "passive" type system. Active abiotic treatment such as sodium hydroxide (NaOH) addition involves intense monitoring, maintenance, and the continued replenishment of expensive chemicals (Oncel et al., 2013). Furthermore, active chemical treatment typically produces a high volume hydrated-iron sludge that is difficult to contain, proving the technology to be less than ideal for sites that are spatially constricted (Johnson & Hallberg, 2005; Skousen, 2002). Active biologic systems, such as off-line sufidogenic bioreactors utilize mixed cultures of heterotrophic sulfate reducing microorganisms (SRM). In these systems biologically mediated sulfate reduction and hydrogen sulfide production can be optimized for selective recovery of trace metals (Johnson & Hallberg, 2005). Similarly, this technology involves a high operating cost in which intricately engineered systems are carefully managed to maintain optimal conditions for the microbial communities by the continuous addition of expensive chemicals (Ňancucheo et al., 2012). Consequently, multiple remediation plans for AML sites have executed the use of passive treatment which includes reducing and alkalinity producing systems (RAPS) that integrate both biogenic and abiotic components.

Anaerobic sulfate reducing bioreactors (ASRB) can function as passive systems in which the influent drainage is continuously treated with no operational supervision. As mentioned previously, success of these systems require the development of reducing and alkaline environments and, as a result, consist of a top compost layer underlain by limestone aggregate. In essence, the compost layer provides substrate to influence consumption of dissolve oxygen via microbial degradation of organic material, while the limestone aggregate maintains alkalinity (Behum et al., 2011; McCauley et al., 2009; Neculita et al., 2007). This promising technology often succeeds in providing short-term, low-cost systems for treatment of acid mine discharges. Still long-term treatment efficiency (>10a) is not readily accomplished and costly maintenance is required to keep these systems working effectively (Zagury et al., 2007). Ancillary data on the technological limitations is essential for future designs of long-term and effective ASRB treatment systems.

1.2. Tab-Simco AML Site

1.2.1. Geology and Mining History

Tab-Simco is an abandoned coal mine comprised of a distinct 12 hectare (ha) "U" shaped hill that rises 37 meters above the surrounding lowland and is located approximately 6 km SE of Carbondale, Illinois (Behum et al., 2011). Two separate Spoon formation coals of the Kewanee group were mined underground between 1890 and 1955, and then later surface-mined in the 1960's and 1970's (Behum et al., 2010). These coals are part of the southwestern portion of the Illinois basin, a Pennsylvanian age system that spans roughly 53,000 square miles throughout Illinois, Western Kentucky, and Southwestern Indiana (Archer, 1996). Illinois coals are typically characterized as having high pyritic sulfur content with minerals containing potentially toxic

chemical elements. Sulfur content of coals in the Illinois basin has been recorded to have values ranging from as low as 0.5 to more than 7 wt%, which depict the heterogenic nature of coals in this basin (Korose et al., 2010; Affolter et al., 2002). At the Tab-Simco abandoned mine the ~2.5 m thick Murphysboro coal seam is the lower of the two seems with a shale unit that ranges from 3 to 8 meters of thickness overlaying it. Above the shale unit is the discontinuous Mt. Rorah coal seam with thicknesses ranging from 0 to 1.5 m thick. The coals are capped by fine-medium grain permeable pyritic-sandstone, that is jointed and highly fractured, with thickness measuring up to 10 meters (Smith, 2002). Under the "U" shaped upland remnant, 12 ha of the Murphysboro and 3 ha of the Mt.Rorah coal seams were room-and-pillar mined. Based on incomplete maps of the operation, the upper and lower seams of the underground works were probably connected by more than one vertical shaft (Smith, 2002).

1.2.2. Hydrology

At the Tab-Simco site, stripping operations during the 1960 and 1970's produced multiple break-ins into the lower underground works, contributing to large volumes of material from the upper seam being exposed to oxygenated rain water (Behum et al., 2010). Data taken from weir hydrographs showed that ~60 vol% of total precipitation in the area is surface run-off, while ~35 vol% of precipitation infiltrates the upper mine works, forming a large mine pool containing seasonal volumes of contaminated water ranging from 40,000-77,000 m^3 (Smith, 2002). The remaining 5 vol% of total precipitation in the area flows through the base of the sandstone cap rock and is expelled at the northern high wall as a non-contaminated seep (Smith, 2002). The mine pool is located 3-5 m above the local water table in the lower mine works. Within the lower mine works, an area of ~150,000 m^3 in which 2/3 is void space is hydraulically

interconnected. Seasonal variations in precipitation have been documented to produce fluctuation in the average volume of the mine pool recording ~42,000 m^3 in December and ~ 80,000 m^3 in May (Smith, 2002). Therefore, ~25 vol% of the lower mine works is subjected to annual wet and dry cycles providing a large surface area for oxidation to occur during the dry seasons and dissolution during wet seasons (Smith, 2002). Even with annual dry and wet seasons, the floodplain adjacent to the Tab-Simco site experiences a relatively consistent base flow of ~150 m^3/day (150,000 L/day) of acid mine drainage exiting from five seeps with pH values ranging between 2.3 to 2.9 (Smith, 2002).

1.2.3. The Site Prior to Reclamation

Less than 50 years after mining activity ceased at Tab-Simco, persistent drainage from the underground works had seeped down-dip (Northward) into the floodplain, producing a 4 ha (9.88 acre) "kill zone" (Figure 1) (Behum et al., 2010). Furthermore, the proliferation of these mine waters had also contaminated the northern flowing Sycamore Creek, 2 km downstream (Smith, 2002). This "kill zone" consisted of acidic iron-rich sediments (Ochre) that were 0.3 m thick and annulled of indigenous plants.

Figure 1: Photograph of acidic iron oxide (Ochre) sediment deposited at the Tab-Simco AML site in southern Illinois. View is taken in a north-easterly direction from the location of the main AMD seep. (Photo taken by Behum, 2004)

1.2.4. Treatment System

In 2007, the Illinois Department of Natural Resources (OSMRE) constructed a passive-type treatment system, that on average treats 1.35 liters per second (LPS) of acid mine drainage produced from the Tab-Simco abandoned coalmine (Behum et al., 2010). Among other contaminants detected within the AMD, the Tab-Simco site has notably high concentrations of dissolved iron Fe (900 mg/L), Al (200 mg/L), Mn (40 mg/L), SO_4 (5000 mg/L), along with an average pH and total acidity of 2.7 and 1,816 (mg/L CCE) respectively (Behum et al., 2011; Current Study). In order to passively sequester such high SO_4 loads, while also minimizing metal contaminants, a remediation system involving an anaerobic sulfate reducing bioreactor was constructed in 2007 (Behum et al., 2010, 2011; Burns et al., 2012).

The treatment system funnels AMD from the main seep through an open limestone channel to promote calcite ($CaCO_3$) dissolution and bicarbonate (HCO_3^-) formation, causing a pH increase before entering the bioreactor. The bioreactor itself is a 0.3 ha (0.75 acre) pond

consisting of three distinct layers: (1) top layer representing a shallow acid impoundment, (2) middle section consisting of a 6-foot thick mixture of organic material (% v/v: 53% woodchips, 27% straw, 11% seasoned municipal compost (yard waste), and 9% agricultural ground limestone) underlain by (3) bottom layer which contains limestone with embedded drainpipes that transports "treated" water out of the reactor (Behum et al., 2011, 2010; Burns et al., 2012). Effluent from the bioreactor enters into meandering channels of limestone (oxidation cells/wetland), which provide a secondary treatment system to further produce alkalinity and promote additional metal precipitation. Finally, treated waters then travel from the oxidation cells into the northern flowing Sycamore Creek (Figure 2).

Amplification of DNA sequences within the microbial communities using 16S rRNA and dsrAB primers determined the presence of iron oxidizing bacteria (Betaproteobacteria) capable of thriving in low pH (2.0-4.0) conditions (Burns et al., 2012). Betaproteobacteria measured in the AMD were recognized to aid in promoting a ~51.5 mol% removal of iron via FeOOH precipitation, prior to entering Sycamore creek (Burns et al., 2012). This displays the significance of microbial-induced mineralization, which drives further research in developing optimal bioremediation strategies with respect to acid mine drainage.

Figure 2: North-easterly view of the treatment system built at the Tab-Simco abandoned mine land site (Photo taken by author, February 2013).

1.2.5. Bioreactor Treatment Efficacy

During the first two years of operation, the Tab-Simco bioreactor displayed relatively high metal removal with contaminant removal percentages up to 75.6 mol% Fe, 99.6 mol% Al, 97.1 mol% Ni, and 93.4 mol% Zn (Behum et al., 2010). However, due to the site constrains, the size of Tab-Simco bioreactor was smaller than recommended for high SO_4^{2-} (0.61 moles/m^3/day) and metal (0.232 moles/m^3/day) loading measured in the AMD (Behum et al., 2010). As the system matured over five years, metal and SO_4^{2-} removal efficiency began to decline along with the pH of the bioreactor effluent. If left unabated, persistent decline of the system could not only cause negligible remediation of the incumbent AMD seeps, but also induce re-dissolution of newly formed precipitates which could further decrease the quality of the AMD drainage.

As the physical, chemical, and biological conditions change in time, mineral precipitates formed within the bioreactor during the treatment process are subject to re-crystallization, phase transformation, and dissolution/precipitation processes (Jolivet et al., 2004; Kim et al., 2008;

Zhu et al., 2012). These processes can result in re-mobilization of the previously sequestered species in solution, producing extremely contaminated plumes of AMD that could be detrimental to the local ecosystem. Additionally, over time exhaustion of organic material and decrease in alkalinity can greatly disrupt biologic activity within bioreactors causing declines in metal sequestration via bio-induced mineralization (Neculita et al., 2008).

Although rehabilitation of the present system via excavation of current material and the subsequent input of fresh substrate is an obvious remedy to the current issue, this approach can cause a dramatic increase in the net cost of the technology. Thus, it is important to quantify the contribution of biological and abiotic processes to improving quality of coal-generated AMD, in order to predict the performance of sulfate-reducing bioreactors in natural settings. Previous work has identified contaminant retention time, exhaustion of organic substrates, precipitate-induced reduction of reactive surface area, and degeneration of system permeability as possible limiting factors to long-lived ASRB performance (Blowes et al., 2009; Lindsay et al., 2011; Neculita et al., 2008; Zagury et al., 2007). In the present study, bioreactor organic substrate amendments were used in field experiments to evaluate the efficiency of various organic carbon sources for passive in situ treatment of coal-generated AMD.

1.3. Experimental Design

1.3.1. Test Cells

Remediation testing within pilot-scale experiments can manipulate a system that is static, batch flow and sampling, or continuously flowing. Static systems contain a definite volume of acid mine drainage in which the water remains in the reactor for extended time periods until extracted for analysis (Cocos et al., 2002; Robinson-Lora & Brennan, 2010). This system

restricts one from obtaining data that can be directly applied to treatment systems, considering that there are no contaminant fluxes, yet it allows for good parameter control and easier interpretation of results. Additionally, a static system provides constraints on reaction kinetics for predicting the retention rates needed for optimal efficiency microbial communities in compost bioreactors. In the batch flow and sampling method, the AMD is introduced as set volumes (pore volumes) into the reactor through an inlet and the effluent water is sampled (Guo & Blowes, 2009). This system is useful because one can measure the chemical parameters of the influent and effluent while also determining the porosity of the substrate.

Although laboratory experiments provide many advantages in quantifying fundamental processes occurring within ASRB treatment technology, they fail to replicate the extreme physical (e.g. temperature, solar radiation, dynamic flow rates) and biochemical (e.g. dissolved constituents, reactive oxygen species, microorganisms) variations characteristic of actual AML sites. Quantifying the temporal transitions in remediation efficacy that occur in bioreactors exposed to these physicochemical variations is important for making rational decisions towards improving this technology. In order to properly test the dependence of ASRB technology on organic substrate composition, six test cells were constructed at the Tab-Simco AML site.

Although some field scenarios can be characterized as experiencing irregular plumes or surges of contaminated water; the Tab-Simco site exhibits year-around, continuous flow of AMD into the treatment system (Smith, 2002; Behum et al., 2011, 2010). Therefore, for the current study, it was practical to construct continuous-flow experiments at the Tab-Simco site in order to realistically replicate field processes. Continuous-flow reactors can establish a constant flow rate of AMD in and out of the system to adequately examine the dynamic biogeochemical processes occurring in the experimental treatment system. Typically sampling ports are located at the

influent and effluent portals of the reaction vessel, but have been also situated at designated increments on the actual reaction column (Bernardez et al., 2012). In the present study, reactors were constructed with graduated sampling ports, in order to quantify the microbial communities at various depths within.

1.3.2. Inoculation of Sulfate-Reducing Microorganisms

Sulfate-reducing microorganisms (SRM) are ubiquitous in natural and anthropogenic environments such as hydrothermal vents, mud volcanoes, sour whey digesters, spoiled foods, wastewater-treatment plants, and sewage-treatment plants (Gibson, 1990; Muyzer & Stams, 2008). Additionally these microorganisms exhibit immense phylogenic diversity in which many groups can utilize a wide range of metabolic growth pathways. In the presence of high sulfate concentrations many sulfate reducing prokaryotes will couple the reduction of this inorganic species to oxidation of low-molecular weight organic substrate. The process is illustrated by the following simplified reaction (Blowes et al., 2009):

$$SO_4^{2-} + 2CH_2O \longrightarrow H_2S + 2HCO_3^- \quad (7)$$

Previous studies have identified success in developing microbial communities capable of reducing high sulfate loads using livestock manure (LM) and sweet whey powder (SWP) as an inoculum (Christensen et al., 1996; Hanajima et al., 2011; Kadota & Ishida, 1972; Priha et al., 2013). Consequently, livestock manure (LM) and sweet whey powder (SWP) were substrates utilized in these experiments, as an initial inoculum, to establish diverse microbial communities in each experimental AMD treatment system.

1.3.3. Choice of Organic Substrate for Long-Term Remediation

Enhancing the performance of SRM communities for AMD treatment has been correlated to the use of low molecular weight (LMW) compounds glycerol and lactate (Bernardez et al., 2012; Coggon et al., 2012; Jong & Parry, 2003). These LMW organics are relatively soluble in aqueous solution and, therefore, could exhibit high mobility in passive treatment systems making them impractical for long-term use without continual input. As a result, these field experiments do not recognize simple substrates (i.e. lactate, ethanol and propionate) as the primary source for long-term remediation in passive treatment systems.

Microbial communities present in AMD treatment systems will establish as a response to the availability of organic substrates and the environmental conditions. For long-term AMD remediation using ASRB technology, sustaining high levels of biologic activity is important and can depend on cultivating diverse microbial communities which are capable of participating in a hierarchal chain of degradation processes. Hydrolytic microorganisms are capable of breaking down polymeric molecules (proteins, lipids, cellulose, lignin and nucleic acids) through enzymatic hydrolysis of the polymeric linkages (Gibson, 1990; Muyzer & Stams, 2008). The bi-products (amino acids, sugars) are then fermented into intermediates (alcohols, lactate and pyruvate) that are readily accessible to SRM. Still, SRM will generally choose to use substrates that have a smaller molecular structure, such as volatile fatty acids (acetate, propionate, butyrate, lactate) in which high rates of sulfate reduction can be achieved. This is due to the higher degree of degradability characterized by these substrates (Gibson, 1990; Muyzer & Stams, 2008). Therefore, it is important for SRM to establish syntropic associations with other microorganisms within the system.

The choice of organic substrate is extremely important when designing a bio-augmentation system because the substrate effectively provides an electron-donor for SRM to reduce sulfate. Traditionally, organic matter is separated into simple and complex substrates in terms of the ease to which microorganisms can degrade it. Simple substrates are typically composed of volatile fatty acids and short-chain fatty acids, while complex substrates being longer chained polymers such as lignocellulose and hemicellulose. As previously mentioned, in terms of passive-flow bioreactors simple substrates such as methanol, ethanol and lactate are not practical due to their solubility and mobility in aqueous solution. To define substrate dependence for long-term bioreactor remediation efficacy variations in herbaceous (i.e. grass clippings, spent brewing grain, leaf compost) and ligneous (i.e. maple wood chips and sawdust) materials were tested.

When compared to ligneous material, herbaceous materials contain higher hemicellulose content which is less resistant to degradation processes. This is due to the amorphous structure of hemicellulose resulting from excessive ether linkages and hydrogen bonding sites that hold this polymer together (Lee et al., 2009). In contrast, lignin or lignocellulose is structurally crystalline and ridged compared to hemicellulose which results in a moderately impervious polymer in terms of short-term microbial degradation. The stability of lignin stems depends on the presence of exceptionally stable aromatic constituents primarily linked together by covalent carbon to carbon bonds along with the absence of numerous ether linkages as characterized in hemicellulose (Vanholme et al., 2010). Therefore, this study assesses the influence organic matter on the treatment efficiency of compost bioreactors by using different mixtures of herbaceous and ligneous materials as organic carbon sources for SRM.

1.4. Hypotheses Tested

1. Long-term treatment efficiency of a sulfate-reducing bioreactor is controlled by the availability and quality of the organic matter to support BSR processes. The optimal ratio of herbaceous vs. ligneous substrates in field scale bioreactors for long-term treatment can be defined by field experiments.
2. Excessive loads of dissolved chemical components in the influent AMD into each experimental reactor will cause a decline in remediation efficiency within a year of monitoring. This decline is related to the formation of coatings on the limestone and organic matter (OM), which reduces the capacity of the treatment system to generate alkalinity and maintain pH values optimal for biological processes and metal sulfide precipitation.
3. Bioreactors are more effective in long-term remediation of acid mine drainage than limestone only reactors.
4. Conducting experiments in the field will result in physical (e.g. temperature) and chemical (e.g., AMD composition) fluctuations that cannot be replicated in the laboratory, allowing the development of practical applications for actual remediation efforts.

1.5. Objectives Outlined

1. Construct six field-scale test reactors at the Tab-Simco abandoned coal-mine in southern, Illinois. Five mixtures containing varying ratios of herbaceous material (Leaf Compost (LC), Grass Clippings (GC), Spent Brewing Grain (SBG)) and ligneous material (Maple

Wood (MW), Maple Saw Dust (MSD). One control mixture representing a limestone settling pond.

2. Monitor the geochemistry, mineralogy, and microbiology of the drainage and solid precipitates for 12 months.
3. Evaluate the ability of different organic mixtures to support microbial processes (e.g., fermentation, sulfate reduction, iron reduction) and improve the overall quality of the AMD.

CHAPTER 2

MATERIALS AND METHODS

2.1. Experimental Design

2.1.1. Reactor Construction

Six 210 liter (55 gallon) polyethylene reactors (R1-R6) were constructed to house the six different mixtures selected for this research. The top of each barrel was cut open to allow AMD to passively flow into the reactor, simulating an acid impoundment (AI) analogous to the full-scale bioreactor at Tab-Simco. Three syringe extraction ports located 21 cm., 42 cm. and 63 cm. from the AI of each reactor. An effluent portal was installed 84 cm. below the AI of each reactor by drilling 1 ¼''-diameter holes along the sides of the barrels and inserting 1 ¼'' polypropylene bulkhead fittings to hold the ports in place. Bulkhead fittings had outer threaded diameters (OD) of 1 ¼'' which were mounted snugly into the drilled holes with the exterior of the reactor pressed up against a thick rubber gasket fitted onto the bulkhead screw. On the interior of the reactor a 1 ¼''-inner diameter (ID) coupling was wrenched tightly onto the bulkhead fitting creating a bulge in the exterior rubber gasket inducing an impermeable seal. Bulkhead fittings contained ½''-(ID) threaded female reducing connectors in which Teflon wrapped ½'' threaded male connectors with ½'' non-threaded female openings were screwed in place to house the sampling ports (syringe extraction, effluent). Extraction ports were constructed by cutting 4'' lengths of ½"-(OD) PVC piping (Sch.40) and placing ½''-(OD) silicone septa between one end of the PVC piping while sealing it into a non-treaded ½''-(ID) connector with Weld-On® PVC cement (Figure 3). These extraction ports were then fastened to the top three ½''-(ID) non-threaded female connectors on each reactor again with Weld-On® PVC cement. As for the effluent ports, perforated "+"-shaped ½''-PVC piping was fastened to the interior of lower bulkhead fitting to

evenly distribute the treated AMD as it exits the reactor (Figure 4). Finally, ½'' ball-valves were sealed with Weld-On® PVC cement to the effluent piping allowing a flow-rate of ~5 mL/min. to be maintained.

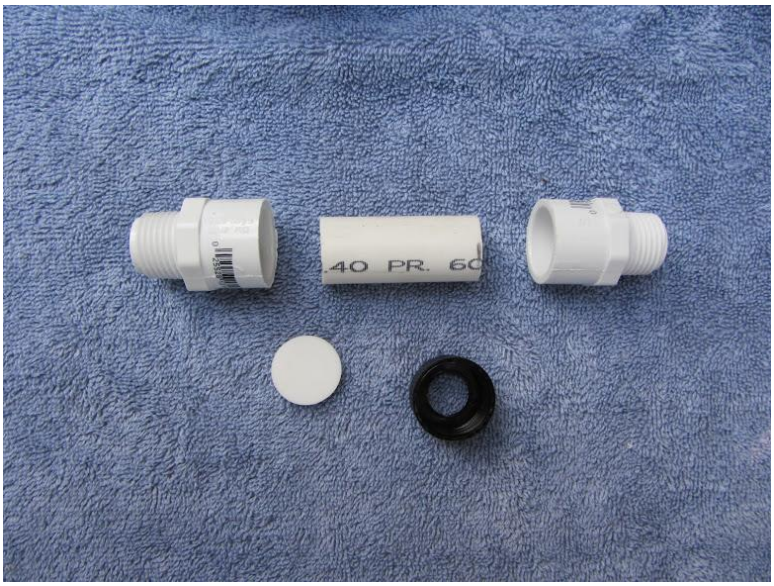

Figure 3: Components of extraction port for each reactor showing (1) two hybrid treaded/non-threaded PVC-connectors (top left/right), (2) one four inch length of ½''-(OD) PVC-piping (top middle) and (3) one ½''-(OD) silicone septum (bottom left). Silicon septum were placed on one end of the PVC-piping and inserted into the non-threaded side of one connector to allow syringe extraction.

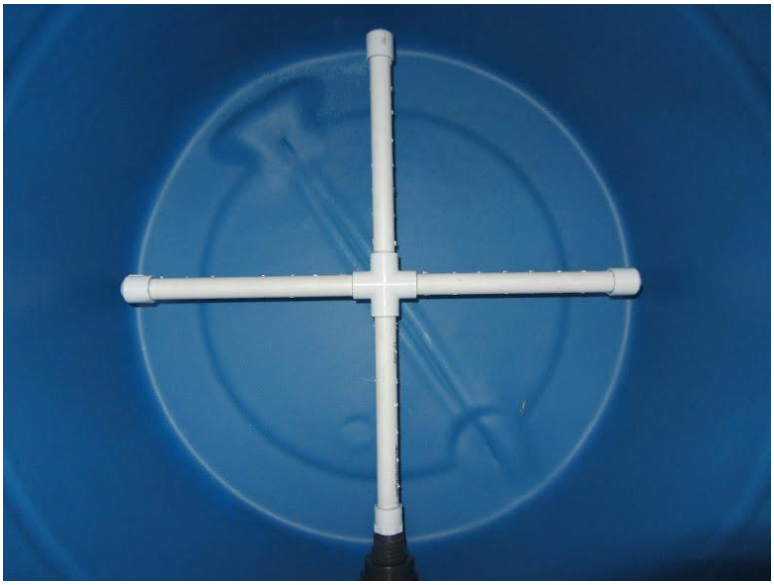

Figure 4: View downward into an assembled reactor displaying perforated "+"-shaped effluent drainage design to allow a spatially equivalent collection of fluid to exit the reactor.

2.1.2. Weir-System Construction

A weir system was built to impound the influent AMD which increased the hydrologic head and allowed gravity fed drainage from the Tab-Simco main seep into each separate reactor for the duration of the experiment (Figure 5). To create this system a 6’’-wide trench was excavated in the channel-way carrying the AMD influent to the large-scale bioreactor. This trench was dug roughly one foot in depth in a perpendicular orientation to the drainage flow-path. Inch thick ply-wood was then fitted into the trench to create a “dam” structure with a “V”-shaped etch at the top to allow drainage to spill over. Three six-foot fence beams were hammered into the ground along the weir on the side opposite of the flow-path to provide additional integrity to the structure. Quikrete® cement was then poured in the trench on both sides of the plywood to hold it into place. To transport the impounded AMD into each reactor a 2 ¼’’ hole was drilled into the plywood where a 2 ¼’’-(OD) bulkhead fitting with 1’’-(ID) thread was then fastened. A foot length of 1’’-(OD) PVC piping was perforated, dry-connected to the interior of the bulkhead fitting (i.e. impoundment side) and dry-capped to prevent frequent clogging by large particulate. On the down-stream side, ten-foot long 1’’-(OD) PVC piping was dry-connected to a 1’’-(ID) non-treaded female/threaded male hybrid connector and fastened to the exterior bulkhead fitting. Four of the ten foot long 1’’-(OD) PVC piping were dry-connected downstream by 1’’-(ID) dual non-threaded female fittings and held in place by six-foot fence post driven into the ground. As the piping extended further from the weir structure slight decreases in topographic elevation allowed a gain in PVC height while sustaining influent flow. To provide the final increase in PVC height needed to gravitationally feed the reactors a 1’’to ½’’-(ID) dual non-threaded female reducing elbow connector was added to decrease flow-path volume and increase flow-rate upwards (Figure 6). This allowed one foot of vertical elevation to

be added with ½’’-(OD) PVC piping giving the necessary height to passively feed each reactor. For ease of cleaning in the case of clogging, all PVC piping used in the weir system was dry-fitted to allow it to be quickly disassembled, cleaned and reassembled.

Figure 5: Photograph of weir constructed along with installed PVC to channel AMD into the test cells.

Figure 6: Photograph of 1’’-1/2’’ (ID) elbow reducing connector added prior to reactor test-cells to decrease flow-path volume and increase flow-rate upwards to provide the additional height required to gravitationally feed each reactor AMD influent.

2.1.3. Reactor Installation

Three wooden pallets were placed in the channel-way near the end of the influent PVC piping previously mentioned. Two reactors were place side-by-side on each pallet while ½''-(OD) PVC piping was extended out between each reactor set per pallet. Once the piping reached a set of reactors, non-threaded cross-fittings were added to transport AMD influent to each barrel with ½''-(ID) ball valves while also continuing the main PVC line downstream to feed the other reactors (Figure 7). Once all sets of reactors were fed influent by cross-fittings, the main line was seal-capped to create hydrologic back-pressure, ensuring a continual flow to all six reactors.

Figure 7: Photograph of reactors actively receiving AMD influent at the Tab-Simco AML site. A main PVC pipeline extends over the three pairs of reactors in which cross fittings allow AMD to be distributed in each reactor.

2.1.4. Reactor Composition

Predetermined mixtures of herbaceous (hemicellulose) and woody (ligneous) organic substrates with a total uncompressed volume of 125L were added to each of the five biologic reactors (Table 1). A 25 liter layer of limestone was added to the bottom of each reactor (R1-R6) to produce alkalinity while maintaining permeability. Reactor (R1) was designed as a control containing only limestone as its total solid volume, acting as an open limestone pond type system. The remaining 185 liters of reactor one was void space for the AMD influent to pool. Sediment sizes of limestone used ranged from cobbles (64-130mm), pebbles (2-64mm) and sand (0.0625-2mm) and were added in equal proportions within the total limestone volume. The following organic substrates were used in the remaining five reactors: leaf compost (LC), grass clippings (GC), spent brewing grain (SBG), maple wood chips (MWC) and maple sawdust (MSD). To test the longevity of ASRB's based on substrate composition, the organic material was classified as containing herbaceous (i.e. LC, GC and SBG) or ligneous (i.e. MWC and MSD) material as its composition and added to each biologic reactor in various proportions (Table 1). Within each bioreactor (R2-R6), 4 gallons of livestock manure and 2 gallons of whey powder were mixed into the organic material to inoculate sulfate reducing bacteria and provide an immediate source of low molecular weight organic compounds. At the top of the bioreactors, the remaining 54 liters were open to the surrounding atmosphere and provided space for the AMD to pool.

Table 1: Distribution of Organic Substances, Limestone and SRB Inoculum within Each Test Reactor

Substrate*	Reactor 1 Limestone	Reactor 2 (10:90)	Reactor 3 (30:70)	Reactor 4 (50:50)	Reactor 5 (70:30)	Reactor 6 (90:10)
LC**	0	4%	12%	20%	28%	36%
SBG**	0	2%	6%	10%	14%	18%
GC**	0	4%	12%	20%	28%	36%
Total Herbaceous	**0**	**10%**	**30%**	**50%**	**70%**	**90%**
MWC**	0	45%	35%	25%	15%	5%
MSD**	0	45%	35%	25%	15%	5%
Total Ligneous	**0**	**90%**	**70%**	**50%**	**30%**	**10%**
LS***	25	25	25	25	25	25
LM***	0	4	4	4	4	4
SWP***	0	2	2	2	2	2

*Leaf Compost (LC), Spent Brewing Grain (SBG), Grass Clippings (GC), Maple Wood Chips (MWC), Maple Sawdust (MSD), Limestone (LS), Livestock Manure (LM), Sweet Whey Powder (SWP)
** Expressed as volume % of the total compost volume
*** Number indicates liters of material added

2.2. Sampling and analytical procedures

2.2.1. Field Measurements

Field measurements (pH/ORP, Conductivity, Temperature, D.O.) were performed at (1) the AMD influent, (2) acid pond of each reactor and (3) effluent port of each reactor using a Hanna® multi-sensor probe. Free proton concentrations (i.e. pH) of samples were documented specifically with a Hanna HI769828-1 field probe (pH/ORP) calibrated to Orion (1.68, 4.01, 7.00) buffer solutions using guidelines described in the factory provided calibration manual (Hanna, 2012). Electric conductivity was measured using Hanna HI769828-3 stainless steel EC probe calibrated at a single point with 5000 μS/cm standard solution (Hanna Instruments® (HI9828-25). Solution oxidation reduction potential (ORP) was analyzed using factory calibrated Hanna HI769828-1 Ag/AgCl field probe at one custom point. Ranges for oxidation reduction potential fall between ±2000mV with ±1.0mV accuracy and resolution of 0.1mV (Hanna, 2012). As per manufacturer's requirement, ORP values were checked against pH prior to all sampling events and maintenance using reducing/oxidizing pretreatment solutions (HI 7091L and

HI7092L) was performed when necessary (Hanna, 2012). Dissolved oxygen (DO) was determined with a Hanna HI769828-2 amperometric field probe calibrated to on site atmospheric oxygen as 100% DO under manufacturer's requirements (Hanna, 2012). The membrane and electrolyte filling solution (HI 76409A/P & HI7042S) for the DO sensor was changed prior to each sampling event to ensure rapid response time and increased accuracy (Hanna, 2012). Temperature was also measured with the fore-mentioned field probe. AMD influent and effluent rates were quantified using a 10mL volumetric flask and timed on a stop watch.

2.2.2. Sample Collection

Samples were collected for dissolved species analyses from the AMD influent and effluent ports of each reactor (R1-R6) in 250mL polyethylene bottles with care to minimize exposure to atmospheric conditions (Myers, 2006). Three graduated sampling ports with silicone septa for syringe extraction of aqueous samples were placed on each reactor for microbial community analyses, at increasing depth from the acid pond. All samples collected on site were stored near field temperatures until alkalinity measurements were performed to prevent temperature induced partitioning of gaseous species into the aqueous phase (Rounds, 2012). Within 30 minutes of collection, samples arrived at the Southern Illinois University Carbondale geochemistry laboratory where further chemical analyses were carried out.

2.2.3. Laboratory Analyses

All laboratory equipment (i.e. glassware, sampling bottles, ect.) used during analytical processing was soaked in distilled water immediately after use until a thorough washing could be performed (Wilde, 2004). Washing involved scrubbing equipment for ten seconds with test tube

brush, rinsing with steady stream of distilled water for ten seconds followed by three flushing's with distilled water and an additional ten second rinse with distilled water. If visible scale had formed on laboratory equipment an overnight soak in 5% nitric acid (ACS certified) solution along with the previously outlined washing procedure was performed. In severe cases in which 5% nitric soak would not remove scale, a saturated solution of RoVer® rust remover (i.e. $NaHSO_3$ and $Na_2S_2O_4$) was prepared and samples were soaked overnight followed by the washing procedure. Upon arrival to the laboratory, samples were immediately filtered with 0.45μm cellulose acetate filter papers (Millpore® HAW) to ensure future analyses would represent dissolved constituents only.

2.2.3.1. Alkalinity

Once filtered, total alkalinity was performed using a Hach® digital titration test kit (Model AL-DT) to an end-point (pH=4.5) measured with the Hanna® multi-parameter probe previously described (Method 10244, 2011). Briefly, 25mL of sample was measured in a volumetric flask (class A) and transferred to a 100mL class A volumetric flask (VF). To wash out any residual sample, two 25mL portions of distilled water were added to the original 25mL volumetric flask (VF), swirled momentarily and then added to the 100mL VF containing sample. Next the 100mL VF was filled to the 100mL mark with distilled water; inverted ten times to mix and then added to a 250mL plastic beaker. Using the calibrated pH probe (Hanna HI769828-1), while stirring, 0.16N sulfuric acid was added drop-wise with a digital titrator (Item #1690001) until the sample pH reached 4.5 units at which the digit reading was recorded. Once the end-point was reached, total alkalinity as meq/L of $CaCO_3$ was calculated according to the method

guidelines. Immediately after alkalinity measurements filtered samples were refrigerated at ~8°C to slow down any reaction kinetics.

2.2.3.2. Dissolved Sulfide and Ferrous Iron

Dissolved sulfide and ferrous iron measurements were carried out on filtered samples within five hours of original raw sample collection to avoid oxidation of these species. Dissolved sulfide and ferrous iron were measured using a UV-VIS spectrophotometer (Hach® DR 3900) via USEPA methylene blue and 1-10 phenanthroline methods, respectively (SMEWW, 1980; USEPA, 2013). In short, samples were diluted for each measurement with distilled water separately to fall within the concentration range for optimal certainty. Typical dilution factors ranged between 1 to 20 and 50 to 300 for sulfide and ferrous iron, respectively. Once optimal dilution concentrations were achieved reagents were added to each sample according to outlined procedures and color was allowed to develop for the allotted time within each sample. After reaction periods expired and the spectrophotometer was zeroed with a blank, samples were transferred to quartz cuvettes (Item # 2495402), placed in the spectra holding cell and the concentration was measured relative to sample absorbance at the pre-programed wavelength.

2.2.3.3. Anions

Filtered samples were subsequently analyzed for dissolved anionic species (SO_4^{2-}, Cl^-, F^-) by means of ion chromatography (Dionex® ICS 2000) using an IonPac® AS18 anion-exchange column. Stock standard solutions were prepared by separately weighing ACS-certified sodium chloride (NaCl), anhydrous sodium sulfate (Na_2SO_4) and sodium fluoride (NaF) with a Mettler® AE100 balance. Crystalline standards were then transferred to a 100mL VF (class A) and

dissolved in MilliQ® (18MΩ) ultra-pure water. Serial dilutions of stock solutions were subsequently performed by pipetting sample into a class A volumetric flask with a 200 μL or 5mL Finnpipette® depending on the dilution factor required and flask used. Volumetric flasks were then filled using MilliQ®(18MΩ) ultra-pure water until the bottom of the meniscus reached the volumetric line. Standards were then inverted 10 times to mix, poured in Dionex® AS-DV sampling vials (P/N 068947) and prepared following manufacturer's requirements (Thermo Scientific, 2012). Serial dilutions of standards were prepared to develop a four point calibration curve (zero representing baseline drift) that fell within the optimal concentration range obtainable for an IonPac® AS18 anion-exchange column.

The high mole ration of sulfate and iron causes hydrated complexes (i.e. hexa-coordinated aquo complexes) to form between these species and, therefore, made it difficult to obtain sulfate values due to peak broadening on the chromatogram. To prevent the complex-induced thickening of the sulfate ion-exchange bands, samples were pretreated with 0.1M NaOH to remove dissolved iron species. Sodium hydroxide addition had an ancillary effect of precipitating dissolved sulfide from bioreactor samples which prevents any oxidative formation of sulfate species. Dilutions caused by sodium hydroxide additions were accounted for and factored in to the final dilution required to place species concentrations within the calibration curve. To confirm the accuracy of this technique, gravimetric analysis via $BaSO_4$ precipitation (Method 375.3 EPA, 1978) was performed on the same samples and compared to the values obtained through ion chromatography (Figure 8). Overall the gravimetric results were on average 14 mol% higher than that of the IC results which is consistent with the EPA method. EPA method 375.3, suggests that samples with high silica and organic content cause interferences resulting in overestimation of sulfate concentrations. Furthermore, charge-balance of each

sample identifies that sulfate concentrations are slightly over-estimated by gravimetric results and underestimated by IC results. As a result, it was determined that averaging the obtained results through both techniques would provide the most accurate sulfate values.

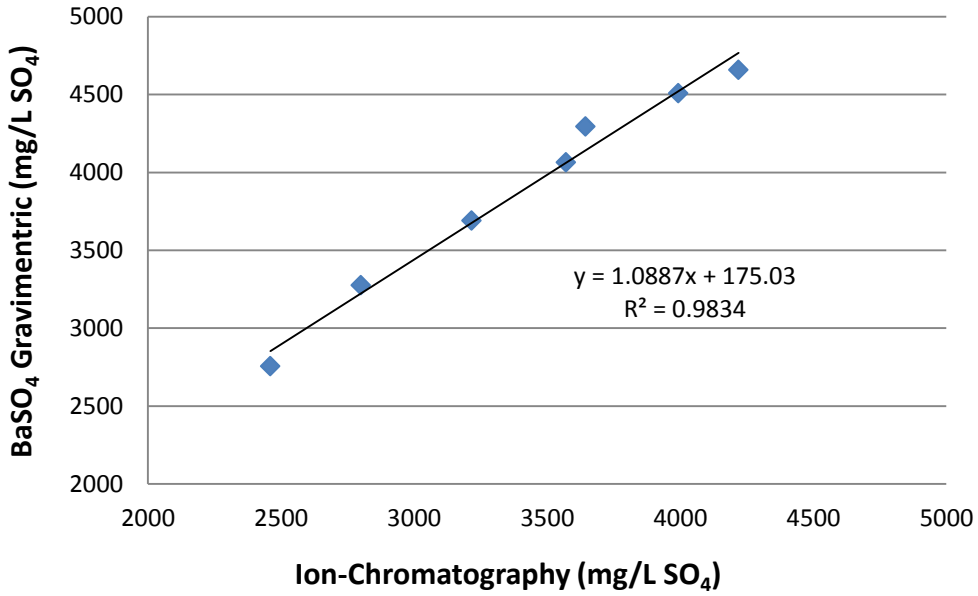

Figure 8: Comparison of sulfate values obtained from gravimetric analysis and ion chromatography.

Phosphate was measured using the vanadomolybdophosphoric acid colorimetric method (APHA, 2005). Briefly, ammonium metavanadate ($(NH_4)VO_3$) was prepared from vanadium pentoxide (V_2O_5) by placing 2 g of sodium carbonate (Na_2CO_3) under reflux in 15 mL of distilled water until completely dissolved. Next, while maintaining a warm solution, 3.5 g of V_2O_5 was added in small portions, converting it into soluble sodium vanadate, and exsolving carbon dioxide. After the reaction subsided (i.e. solution went from yellow to clear), 2.0 g of ammonium chloride was dissolved in 7.5 mL of distilled water and poured slowly into the hot sodium vanadate solution. The solution was allowed to cool to room temperature and then placed in an ice bath to enhance the formation of white ammonium metavanadate crystals ($(NH_4)VO_3$). The crystals were then vacuum filtered, washed with excessive amounts of distilled water,

scraped onto a clean watch glass and placed in an oven to dry at 100°C for 1 hour. Once dried, 1.25 g of ammonium metavanadate crystals were dissolved in 300 mL of distilled water that was brought to a boil under reflux conditions. Next, the ammonium metavanadate solution was cooled to room temperature and 330 mL of concentrated HCl (ACS certified) was added. A separate solution containing 25 g of ammonium molybdate $(NH_4)_6Mo_7O_{24}\cdot 4H_2O$ was dissolved in 300 mL distilled water and added to the ammonium metavanadate solution after the heat produced from the HCl addition had subsided. Finally, the 930 mL of reagent was brought to 1 L by adding distilled water in a 1 L (class A) volumetric flask.

A stock phosphate standard solution was prepared by dissolving ACS-certified sodium phosphate tribasic dodecahydrate ($Na_3PO_4\cdot 12H_2O$) crystals in MilliQ® (18MΩ) ultra-pure water. Serial dilution of the stock phosphate solution was performed to create a five-point calibration curve which was programmed on a UV-Vis spectrophotometer (Hach DR 3900). The program was set in the visible spectrum at a wavelength of 400 nm and calibrated to phosphate standards of (1.0, 5.0, 10.0, 15.0 and 20.0) mg/L-PO_4. Color development of both the standards and samples was achieved by adding 35 mL of sample to a 50 mL (class A) volumetric flask followed by a 10 mL addition of the vanadomolybdophosphoric acid reagent and filling the rest of the VF with distilled water. Blank samples were prepared by replacing the 35 mL of sample with distilled water. Color was allowed to develop for 15 minutes and the phosphate concentration was measured relative to its absorbance at 400 nm.

2.2.3.4. Cations

To preserve dissolved cations, immediately after samples were filtered, a 100 mL fraction of the filtrate was measured volumetrically and acidified to a 5 wt/v% nitric acid (ACS certified)

solution. Metal analyses (Fe, Mn, Cu, Sr, Cd, Ni, Zn, Ca, Mg, K) were perform via atomic absorption spectrophotometry (Z-2000 Tandem AA) using Teledyne plasma-pure® stock aqueous metal standards. Each stock metal standard contained 1000 ppm metal cation solvated in a 5 wt/v% nitric acid solution. Standards were prepared by pipetting each stock metal standard to a 1 L (class A) volumetric flask using a 200 μL or 5 mL Finnpipette® depending on final concentration required. Once addition of all metal standards was completed, MilliQ® (18MΩ) ultra-pure water containing 5 wt/v% nitric acid (ACS certified) was added until sample meniscus reached the 1 L mark. Depending on the optimal linear response of each metal cation up to five points of calibration (minimum of three) were created using separately prepared mixed-metal standard solutions following the fore-mentioned guidelines. MilliQ® (18MΩ) ultra-pure water containing 5 wt/v% nitric acid (ACS certified) was tested against MilliQ®(18MΩ) water without nitric acid and no difference in background absorbance was detected under all cathode lamps used for metal measurements. Therefore, nitric acid addition to samples did not account for increased absorbance of any metal and thus only a 5% dilution factor was accounted for in the results. Furthermore MilliQ®(18MΩ) ultra-pure water without nitric acid was used as a blank within the calibration curve primarily to prevent corrosive wear on the instrument from the continued aspiration of a 5 wt/v% nitric acid solution (Hitachi, 2004).

2.2.3.5. Sulfur Isotopes

After samples were filtered to 0.45 μm, a 50 mL fraction of filtrate was measured in a 50 mL VF (class A). Next, the sample was transferred to a 100 mL beaker, acidified to a pH of roughly 2.0 units (if needed), covered with a watch glass and placed on a hot plate until samples were warmed to 80°C. Then, barium sulfate precipitation was performed through drop-wise

addition of saturated barium chloride ($BaCl_2$) solution (Method 375.3 EPA, 1978). Once no visible precipitate was forming after the addition of $BaCl_2$, an excess of 1 mL $BaCl_2$ solution was added to ensure complete precipitation and solution was kept at 80°C for another hour. To promote crystal growth, samples were left on hot plate overnight at 45°C. Finally, barium sulfate ($BaSO_4$) crystals were separated from supernatant, dried in the oven at 100°C and sent to the mass spectrometry facility at Indiana University Bloomington for sulfur isotope analysis. A Finnigan MAT 252 mass spectrometer equipped with an elemental analyzer was used to determine sulfur isotopic compositions of the $BaSO_4$ precipitates mentioned previously using methods outline by: Lefticariu et al. (2006).

2.2.3.6. Aluminum

Aluminum concentrations were measured on a Hach DR9000 spectrophotometer using the acidified sample (5 wt/v% nitric) which was also prepared for AAS analyses. Since dilution factors of up to 300 were required to fall within the Aluminon® method (Hach, 2013) range (0.008 – 0.800 mg/L) it was unnecessary to raise the sample pH > 3.5 as recommended by the manufacturer. After samples were diluted to fall within the calibration range, one packet of ascorbic acid (C/N 1457799) was dissolved completely in 50 mL of sample. Next one AluVer 3® (C/N 1429099) reagent packet was added to the sample and inverted for one minute as the sample developed a red-orange color. A blank was prepared by transferring a 10 mL fraction of the colored sample to a quartz cuvette along with one Bleaching 3® (C/N 1429449) reagent package and swirled vigorously for 30 seconds. Finally, both the sample and blank were allowed to react for 15 minutes, followed by zeroing the instrument with the blank, and measuring the absorbance of the sample. Since fluoride ions interfere at all concentration levels, aluminum

concentrations were corrected for this interference as outlined in the manufacturer's method (Hach, 2013).

2.2.3.7. Microbiology

In collaboration with SIUC Department of Microbiology, pyrosequencing of the bacterial communities was performed on the samples collected at sampling ports and effluent portals of each reactor, a week after the experiment began and after 9 months of operation (Pugh, 2013). Duplicate DNA extractions where taken from both water and solids from each reactor. Solid DNA extraction was carried out using a FastDNA SPIN® Kit for Soil under manufacturer's protocol (Biomedicals, 2013). 16S rRNA gene pyrosequencing was performed on the resultant DNAs at Molecular Research (Shallowater, Texas). Evaluation of samples were conducted by Tag-encoded FLX amplicon pyrosequencing (bTEFAP) ran on a 70675 GS PicoTiter Plate using the Genome Sequencer FLX System (Roche), under methods described by: Shange et al. (2012). To effectively model bacterial communities present, sequences were sorted by operational taxonomic units (OTUs) at 3% sequence similarity. To complement the pyrosequencing results, fluorescent in situ hybridization (FISH) was carried out on samples to define the microbial diversity within each reactor at a Class and Domain level. Standard protocol outlined in Amann and Fuchs was carried out to properly identify microbial communities using the FISH technique (Amann & Fuchs, 2008).

CHAPTER 3

RESULTS

3.1. Physical and Chemical Parameters of the Experimental System

3.1.1. Temperature

Southern Illinois is described as a region of temperate climate that experiences extreme temperature fluctuations both annually and daily. For the duration of these experiments, all reactors had been exposed to temperatures between -13^{0}C (8^{0}F) and 35^{0}C (96^{0}F). Water temperatures measured in the field closely resembled the average daily recorded ambient air temperatures of the local area (Figure 9). Within any given sampling point, the average standard deviation in temperature between each reactor was ±0.54°C which was slightly greater than the instruments tolerance level of ±0.15°C.

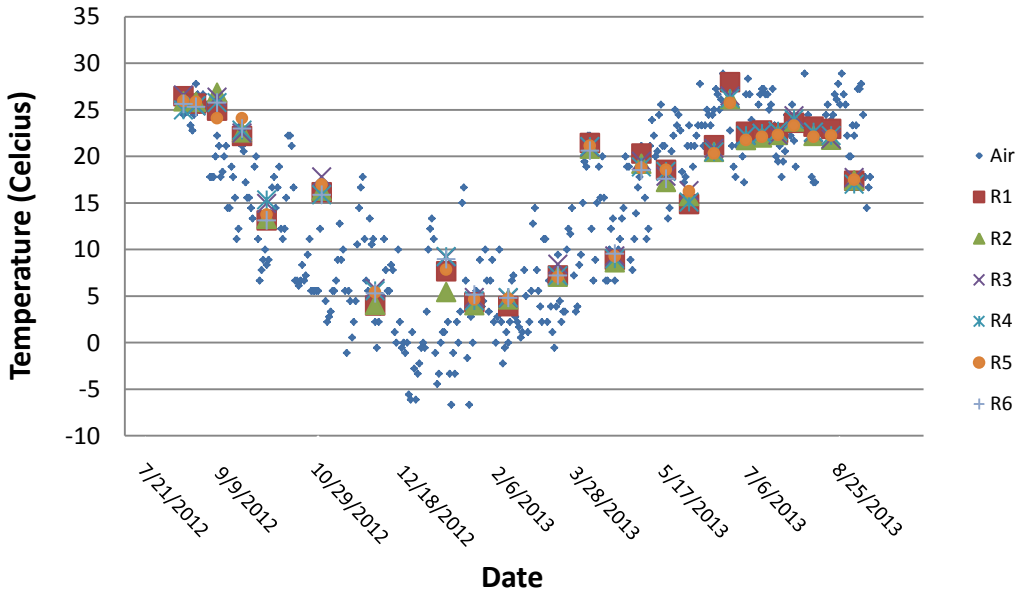

Figure 9: Effluent fluid temperatures recorded in each reactor along with average ambient air temperatures throughout the experiment. Averaged METAR reports were compiled for ambient air temperatures measured at Southern Illinois Airport (Carbondale/Murphysboro) during the course of this study. Air temperature data are from National Weather Service (www.weather.gov).

3.1.2. pH Values

Free proton concentrations were recorded in influent AMD, acid impoundments and effluent ports within each reactor. Influent pH values were relatively constant throughout the experiment with an average 2.80 (n= 26, 1σ = ± 0.15). Interestingly, the average pH values recorded in the acid pond of reactor R1 (limestone only) was 2.62 (n= 26, 1σ = ± 0.25), which was ~0.2 pH units ***lower*** than that of the influent AMD (Figure 10). Average effluent pH values for the reactor (R1) were also significantly stable for the duration of the twelve experimental months, with an average pH value of 3.34 (n= 26, 1σ = ± 0.4), which was ~0.5 units higher than the average pH values of the influent AMD (Figure 11). The pH temporal trends measured in the bioreactors were, however, very different. In all bioreactors (R2-R6), during the initial months of the experiments from August to early December, the effluent pH values increased from an initial pH value of ~4.5 to ~ 6.2. In the following four months (January 2013-April 2013) the dominantly ligneous (woody) reactors (R2, R3) displayed a substantial temporal decrease in pH values averaging 5.16 (n=12, 1σ = ± 0.47) in effluent relative to pH values of 5.8 (n=6, 1σ = ± 0.36) in R4, 5.77 (n=6, 1σ = ± 0.44) in R5 and 6.0 (n=6, 1σ = ± 0.37) in R6. During the last 4 months of the experiments (April 2013-August 2013), all bioreactors began to exhibit gradual decreases in effluent pH, reaching a pH plateau of ~4.0 at the beginning of July 2013. Overall, ligneous reactors (R2, R3) displayed an average effluent pH of 4.77 (n=52, 1σ = ± 0.65) while the herbaceous reactors (R5, R6) had an average pH of 5.11 (n=52, 1σ = ± 0.77). The average effluent pH value of 4.98 (n=26 1σ = ± 0.8) for reactor R4 (50:50 mixture, herbaceous: ligneous) fell between average pH values of the ligneous reactors (R2, R3) and herbaceous reactors (R5, R6).

Measurements taken from the acid impoundments (AI) at the top of the bioreactors (R2-R6) had displayed two peaks in pH values, the first one ~3 weeks (September 2012) after the experiment began and the second one ~14 weeks after commencement (November 2012). The first peak was measured in all bioreactors (R2-R5) while the second peak observed only in R3, R4 and R5 bioreactors. Starting in January 2013, measurements of the acid impoundment in all the bioreactors show a constant decrease in pH values. By the end of March 2013, the AI pH values became lower than the AMD influent pH values, a trend which is similar to that of the AI pH values measured in reactor R1. Since March 2013, the average AI pH values in all the biologic reactors (R2-R6) was 2.58 (n=75, 1σ = ± 0.3), while influent pH was 2.76 ((n=26, 1σ = ± 0.14). This change marks an average pH decrease of ~0.20 units of the AI from influent AMD for each bioreactor.

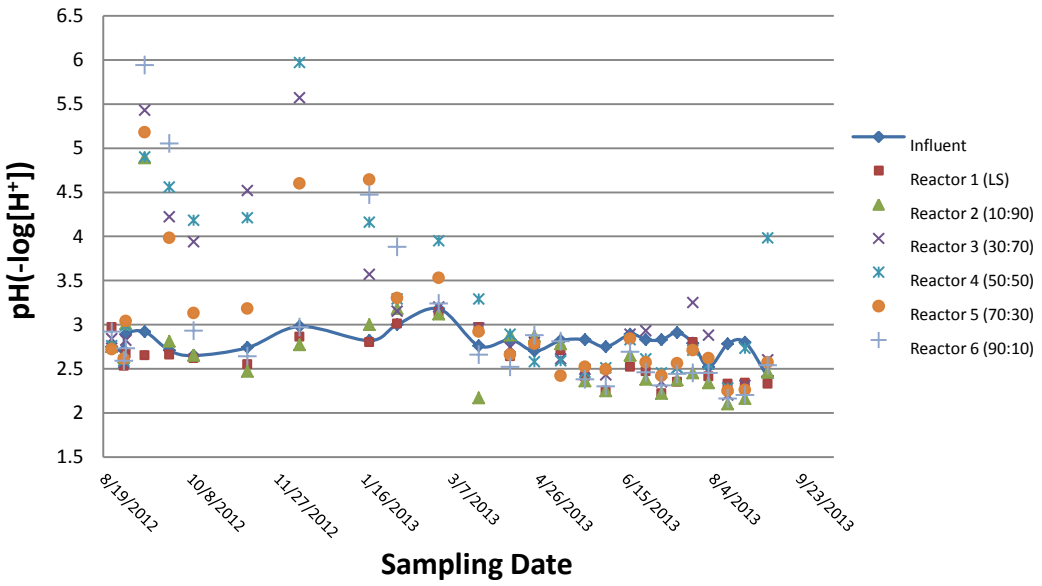

Figure 10: Free proton concentrations (pH) recorded at the AMD influent and acid impoundment of each reactor (R1-R6) during the course of the experiment.

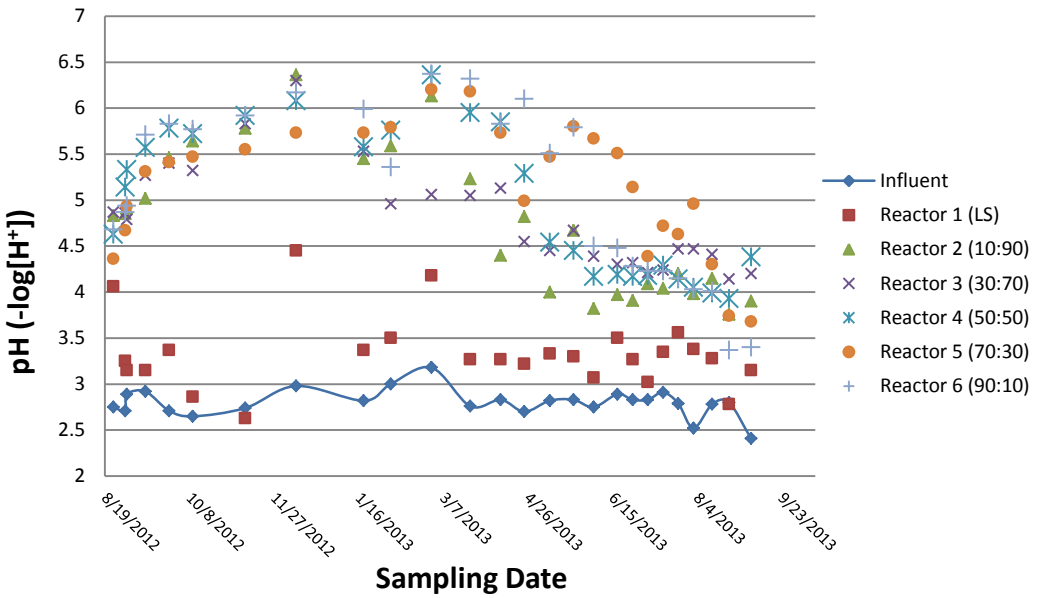

Figure 11: Free proton concentrations (pH) recorded at the AMD influent and effluent of each reactor (R1-R6) during the course of the experiment.

3.1.3 Alkalinity

Total alkalinity was measured in effluent samples that had display pH values greater than 4.5 during field measurement. As a consequence, influent AMD and the effluent of reactor R1 (LS) never reached pH values over 4.5 and thus were documented as each displaying no titratable alkalinity (Figure 12 & 13). Within the bioreactors (R2-R6), a large increase in alkalinity was most pronounced in R3, R4 and R5 with reactors R3 and R4 reaching alkalinity as high as 4200 mg/L as $CaCO_3$ during the second week of the experiments. Continued measurements identified that high levels of alkalinity were not maintained and the effluent alkalinity in the bioreactors (R2-R6) decreased to values below 500 mg/L as $CaCO_3$ by November 2012. From November 2012 to May 2013, notable differences in alkalinity values were measured, as ligneous (R2, R3), 50/50 mixture (R4) and herbaceous (R5, R6) had average alkalinity values of 97 mg/L (n=20, $1\sigma = \pm 97$mg/L), 132 mg/L (n=10, $1\sigma = \pm 93$mg/L) and 275 (n=20, $1\sigma = \pm 183$mg/L) mg/L as $CaCO_3$, respectively. Therefore, in terms of alkalinity

bioreactors with increased herbaceous content (i.e. R4, R5, R6) displayed greater neutralizing capacity relative to the bioreactors with dominantly woody substrate (i.e. R2, R3)

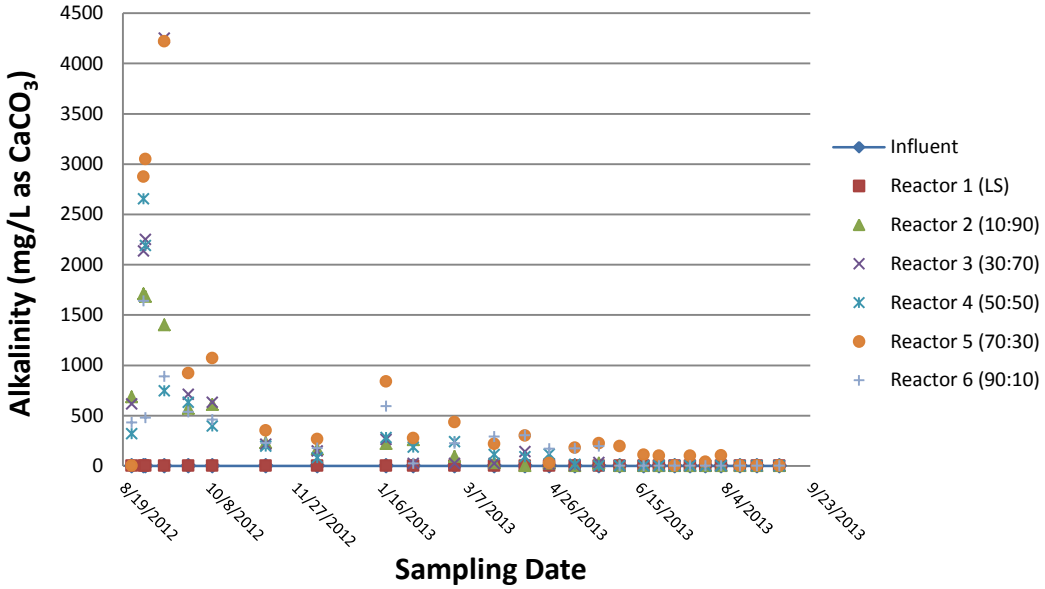

Figure 12: Total alkalinity (mg/L as $CaCO_3$) measured in the effluent of each reactor (R1-R6) during the course of this experiment.

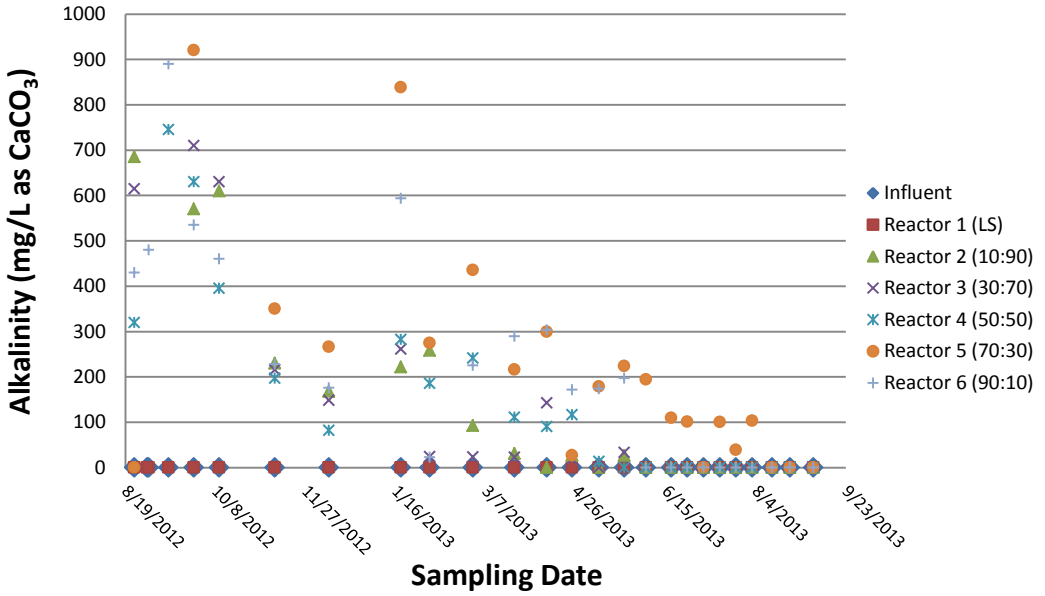

Figure 13: Rescaled view of Total alkalinity (mg/L as $CaCO_3$) measured in the effluent of each reactor (R1-R6) during the course of this experiment (only alkalinity values < 1000 mg/L as $CaCO_3$ are plotted). Notice that influent AMD and reactor 1 (limestone only) did not record pH > 4.5 and thus contained no titratable alkalinity.

3.1.4. Oxidation-Reduction Potential (ORP)

Throughout the duration of the experiments, the ORP values of samples taken from the effluent port of the limestone only reactor (R1) displayed similar trends to that of the AMD influent (Figure 14). During the initial six months (August, 2012-early February, 2013) the average ORP values measured in the AMD and R1 effluent were 128 (n=11, 1σ = ± 157mV) and 69 mV (n=11, 1σ = ± 110 mV), respectively. In the following months (late February - early September, 2013), the average ORP values had increased in both the AMD influent and R1 effluent to values of 370 mV (n=15, 1σ = ± 32 mV) and 300 mV (n=15 1σ = ± 69 mV), respectively.

For each bioreactor (R2-R6), a steady decline in ORP values was measured during the first month of the experiment, from an initial average value of 138 mV (n=5, 1σ = ± 4.4 mV) to average values lower than -100 mV, which subsequently leveled off near -139 mV until early December 2012. As the temperatures remained around 0^0C (i.e. January-March, 2013), the ORP values measured in the bioreactors began to increase to values similar to both the AMD influent and R1 with average ORP values of -42 mV (n=20, 1σ = ± 39 mV). In the spring and summer months (i.e. early April-September, 2013), a decline in ORP values was recorded in bioreactor (R2-R6) effluents, maintaining ORP values lower than -100 mV. Standard deviation of the measured ORP values between the bioreactors (R2-R6) during each sampling event was ±19 mV (n = 130) throughout the entire experiment, a value which is greater than the instrument tolerance of ±1 mV. The herbaceous reactors (R5, R6) maintained a lower redox potential averaging -154 mV (n=52, 1σ = ± 92 mV) relative to -150 mV (n=26, 1σ = ± 92 mV) in the 50/50 mixture (R4) and -145 mV (n=52, 1σ = ± 97 mV) in the ligneous reactors (R2, R3).

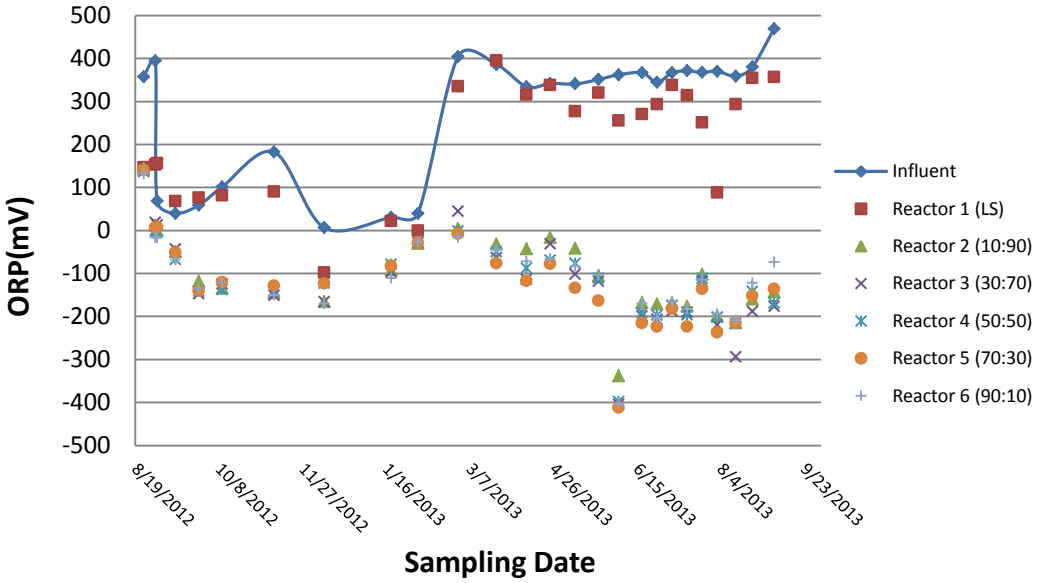

Figure 14: Redox potential of AMD influent and effluents of each reactor throughout the experiment. Redox values were recorded as ORP in millivolts (mV) as described in the instrument methodology.

3.1.5. Dissolved Oxygen

During these field experiments, large temporal fluctuations in influent AMD dissolved oxygen (DO) values were recorded. In order to better express the mobility of DO within each reactor (R1-R6), the DO values of the influent AMD were used as a baseline for comparison. The difference in measured DO values between of the influent AMD and the acid impoundments (eq.8) (R1-R6) is presented in Figure 15, and the difference in DO values between the acid impoundments (R1-R6) and the effluent (R1-R6) within each reactor (eq.9) is presented in Figure 16. The following equations were used to derive DO values plotted in each figure:

$$DO_{(Acid\ Impoundment)} - DO_{(Influent)} = \Delta DO_{(In \rightarrow AI)} \quad (8)$$

$$DO_{(Effluent)} - DO_{(Acid\ Impoundment)} = \Delta DO_{(AI \rightarrow Eff)} \quad (9)$$

Where $DO_{(Influent)}$, $DO_{(Acid\ Impoundment)}$ and $DO_{(Effluent)}$ represents the concentration of DO in ppm measured at the AMD influent, reactor acid impoundment and effluent, respectively. Thus, positive ΔDO values represent net increases in DO concentration while negative ΔDO values

coincide with net consumption of DO as AMD influent travels to the acid impoundments, through the reactors, and to the effluent ports of each reactor (R1-R6). Throughout the experiment, all the reactors (R1-R6) displayed similar values for $\Delta DO_{(In \rightarrow AI)}$ and $\Delta DO_{(AI \rightarrow Eff)}$.

For all reactors, during the first two months (August-October, 2012) of the experiment, there was an average decrease in DO measurements between the AMD influent and the acid impoundment ($\Delta DO_{(In \rightarrow AI)}$ = -2.71 ± 2.13 ppm, n=36). During the following five months (November 2012- March 2013), the DO measurements recorded an increase in DO from the influent to the acid impoundments of each reactor ($\Delta DO_{(In \rightarrow AI)}$ = +3.77 ± 1.58 ppm, n=36). During the final months of the experiment (May 2013 – early September 2013) an overall decrease of DO was once again measured ($\Delta DO_{(In \rightarrow AI)}$ = -1.11 ± 1.83 ppm, n=84).

In contrast, during the first two months (August – October 2012) of the experiments, a slight increase in DO was measured from the acid impoundments to the effluent ports of each reactor ($\Delta DO_{(AI \rightarrow Eff)}$ = +0.24 ± 0.77 ppm, n=36). During the following five months (November 2012-March 2013), a significant decrease in DO was recorded from the acid impoundments to the effluent ports ($\Delta DO_{(AI \rightarrow Eff)}$ = -7.63 ± 3.18 ppm, n=36) . In the final months of the experiment (May 2013 – early September 2013), an overall increase in DO was measured from the acid impoundment to the effluent port of each reactor ($\Delta DO_{(AI \rightarrow Eff)}$ = +0.87 ± 1.33 ppm, n=84 ppm). Overall, the herbaceous reactors (R5, R6) documented the highest consumption of DO from influent to the acid impoundments ($\Delta DO_{(In \rightarrow AI)}$ = -0.69 ± 3.00 ppm, n=52) while reactor R4 recorded the second highest ($\Delta DO_{(In \rightarrow AI)}$ = -0.61 ± 3.22 ppm, n=26) and the ligneous reactors (R2, R3) had the lowest consumption ($\Delta DO_{(In \rightarrow AI)}$ = -0.28 ± 3.34 ppm, n=52). From acid impoundments to effluent ports, reactor R4 (50/50) showed the highest average consumption of DO ($\Delta DO_{(In \rightarrow AI)}$ = -1.32 ± 4.20 ppm, n=26), followed by the herbaceous reactors (R5, R6)

($\Delta DO_{(In \rightarrow AI)}$ = -1.10 ± 4.10 ppm, n=52) and the ligneous reactors (R2, R3) ($\Delta DO_{(In \rightarrow AI)}$ = -1.03 ± 4.62 ppm, n=52).

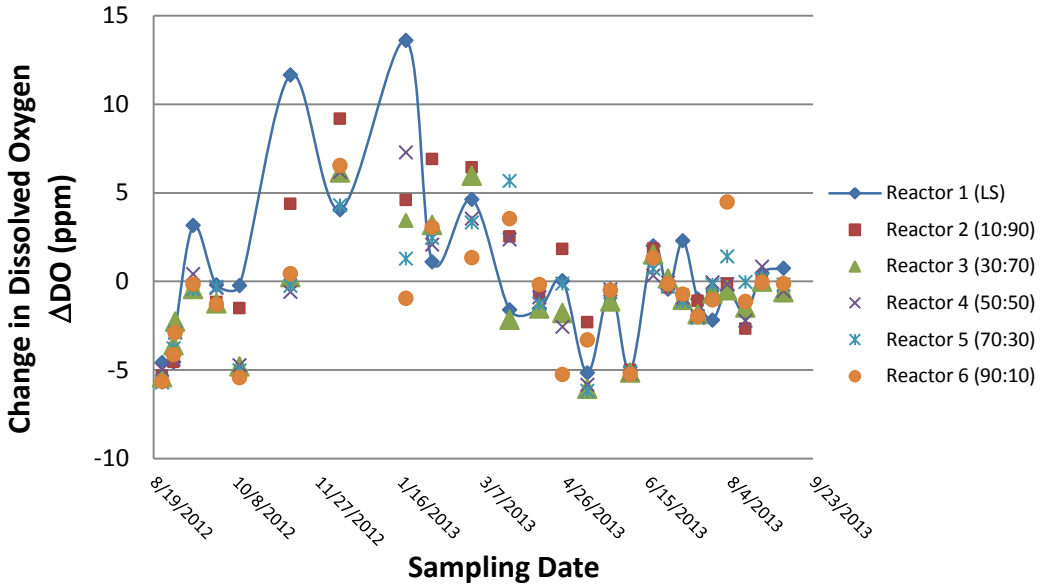

Figure 15: Changes in dissolved oxygen measurements (DO) from influent AMD to the acid impoundments of each reactor (R1-R6). Positive ΔDO correspond to a net increase in DO from influent while negative ΔDO indicates a net decrease.

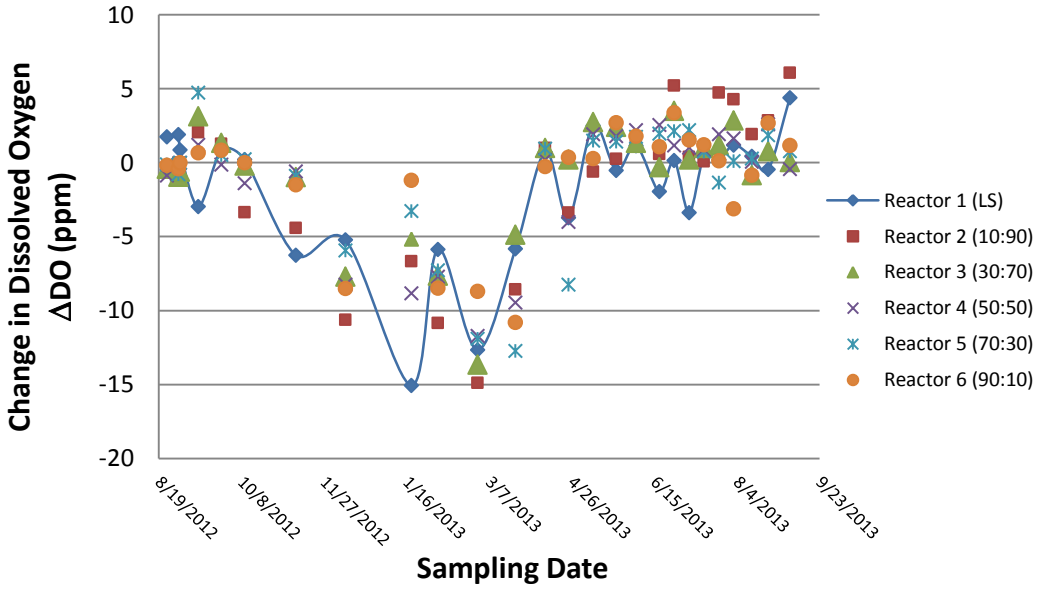

Figure 16: Changes in dissolved oxygen (DO) measurements from the acid impoundment to the respective effluent port of each reactor (R1-R6) as the experiment progressed. Positive ΔDO correspond to a net increase in DO from acid impoundments while negative ΔDO indicates a net decrease.

3.2. Major Anions and Metals

3.2.1 Sulfate

During these experiments, the concentration of dissolve sulfate varied significantly not only in the reactors' effluent but also in the AMD influent (Figure 17). In the AMD influent, high sulfate values of ~ 6000 mg/L were measured in August 2012 at the beginning of the experiments. This was due to a very hot summer with almost no precipitation, which favored increased weathering and high concentration of sulfate and metal in AMD influent. However, during the fall of 2012, the sulfate values in the AMD influent stabilized at ~ 5000 mg/L, and stay near this level until the end of the field experiments.

The sulfate concentrations in all the reactors (R1-R6) averaged 3363 mg/L SO_4^{2-} (n=24, $1\sigma = \pm$ 160 mg/L) during the first three weeks of operation. From late September-early December, 2012 the average sulfate concentrations recorded from the effluents of the bioreactors was 2118 mg/L SO_4^{2-} (n=20, $1\sigma = \pm$165 mg/L) while reactor R1 (LS) averaged 3425 mg/L SO_4^{2-} (n=4, $1\sigma = \pm$ 394 mg/L). Persistent exposure to low temperatures (T< 10°C) from January-March, 2013 resulted in increased sulfate concentrations measured in effluent of all reactors. During this time, the LS (R1), ligneous (R2,R3), 50/50 mixture (R4) and herbaceous (R5, R6) reactors recoded effluent sulfate concentrations of 4104mg/L SO_4^{2-} (n=4, $1\sigma = \pm$ 565 mg/L), 4030 mg/L SO_4^{2-} (n=8, $1\sigma = \pm$ 349 mg/L), 3828 mg/L SO_4^{2-} (n=4, $1\sigma = \pm$ 386 mg/L) and 3488 mg/L SO_4^{2-} (n=8, $1\sigma = \pm$ 321 mg/L), respectively. In the subsequent months (i.e. March-September, 2013), average sulfate concentrations increased to 4303 mg/L SO_4^{2-} (n=14, $1\sigma = \pm$ 358 mg/L) within effluent samples taken from reactor R1 yet decreased within the bioreactors. During this time the herbaceous reactors (R5, R6) recorded the lowest sulfate levels of 3476 mg/L SO_4^{2-} (n=28, $1\sigma = \pm$ 259 mg/L) while the ligneous (R2, R3) and 50/50 mixture (R4) had

significantly higher sulfate concentrations of 3864 mg/L (n=28, 1σ = ± 225 mg/L) and 3979 mg/L (n=14, 1σ = ± 414 mg/L), respectively.

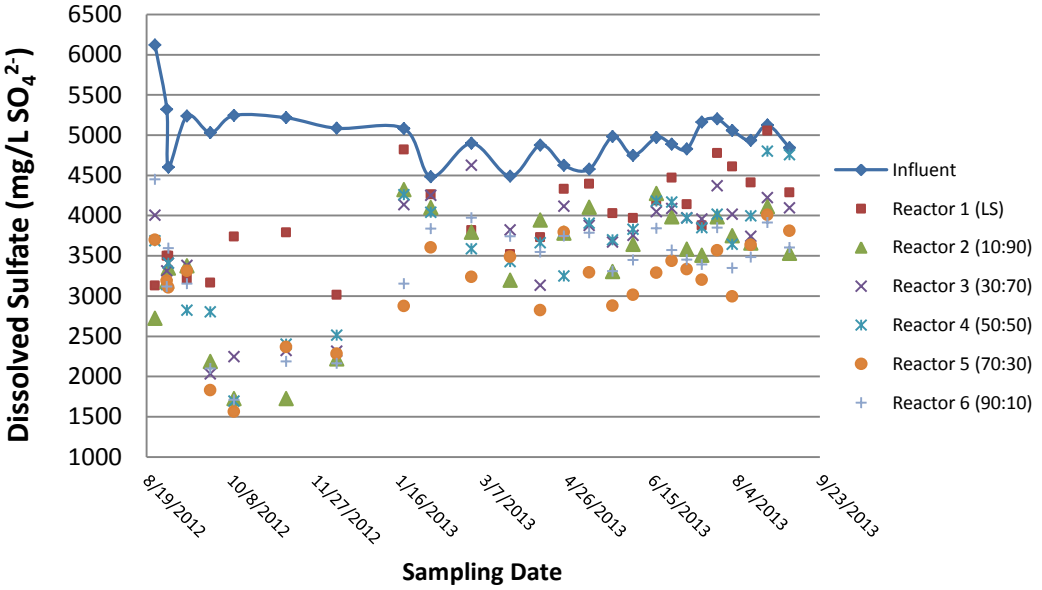

Figure 17: Dissolved sulfate concentrations (mg/L SO_4^{2-}) measured in the AMD influent and effluent of each reactor (R1-R6) at each sampling event.

3.2.2 Sulfur Isotope Composition ($\delta^{34}S$) of Dissolve Sulfate

The average sulfur isotope composition of the dissolved sulfate in the influent AMD showed minor variability and was determined as $\delta^{34}S$ = +5.93‰ (n=11, 1σ = ± 0.51‰) (Table 2). Reactor R1 effluent demonstrated minimal isotopic fractionation in $\delta^{34}S$ values from influent AMD sulfate values measuring +5.97‰ (n=11, 1σ = ± 0.38‰) overall. Within the bioreactors (R2-R6) relatively high $\delta^{34}S$ values were recorded in November and December, 2012; reaching up to +15.59‰ in reactor R3. During the low-temperature months (January-March, 2013), $\delta^{34}S$ values of dissolved sulfate decreased within the bioreactors' effluent (R2-R6) averaging +6.72‰ (n=15, 1σ = ± 0.61‰). Sulfur isotopic analyses of the dissolved sulfate in the bioreactors' effluent (R2-

R6) from April-July, 2013 determined a shift towards relatively higher $\delta^{34}S$ values with respect to those measured in dissolved sulfate in the influent AMD. Increased herbaceous content essentially correlated to higher $\delta^{34}S$ values as reactor R2, R3, R4, R5 and R6 averaged +8.19‰ (n=11, 1σ = ± 2.16‰), +8.66‰ (n=11, 1σ = ± 3.16‰), +8.55‰ (n=11, 1σ = ± 2.27‰), +8.66‰ (n=11, 1σ = ± 2.38‰) and +9.08‰ (n=11, 1σ = ± 2.97‰), respectively.

Table 2: Sulfur Isotope Composition ($\delta^{34}S$) of the Dissolve Sulfate

Collection Date	Influent ($\delta^{34}S$)	Reactor 1 ($\delta^{34}S$)	Reactor 2 ($\delta^{34}S$)	Reactor 3 ($\delta^{34}S$)	Reactor 4 ($\delta^{34}S$)	Reactor 5 ($\delta^{34}S$)	Reactor 6 ($\delta^{34}S$)
08/24/12	5.40	5.34	5.23	4.98	5.40	5.30	5.21
10/10/12	6.44	6.32	7.94	7.70	8.16	7.85	8.34
11/10/12	4.93	5.52	12.19	13.47	11.78	11.03	13.42
12/10/12	5.57	5.48	13.80	15.59	13.10	11.62	15.24
01/19/13	5.51	5.89	6.77	7.20	7.10	9.09	10.64
02/04/13	6.09	6.17	6.50	6.47	6.63	5.03	6.86
03/23/13	6.15	6.18	6.35	6.59	6.78	6.98	7.11
04/24/13	6.07	6.26	6.42	6.92	8.14	6.77	7.21
05/23/13	6.33	6.42	8.18	8.57	8.66	10.37	8.41
06/14/13	6.61	6.22	8.02	8.97	8.78	10.83	8.39
07/24/13	6.16	5.92	8.73	8.79	9.57	10.44	9.02
Average	**5.93**	**5.97**	**8.19**	**8.66**	**8.55**	**8.66**	**9.08**
Stdev (1σ)	**0.51**	**0.38**	**2.61**	**3.16**	**2.27**	**2.38**	**2.97**
Max	**6.61**	**6.42**	**13.80**	**15.59**	**13.10**	**11.62**	**15.24**
Min	**4.93**	**5.34**	**5.23**	**4.98**	**5.40**	**5.03**	**5.21**

*Sulfate was precipitated from AMD influent and the effluent of each reactor (R1-R6).

3.2.3 Sulfide

Dissolved sulfide (S^{2-}) concentrations measured in the influent AMD and reactor R1 (LS) effluent during each sampling were at or below detection limit, suggesting that very little or no dissolved sulfide was produced in these cases (Figure 18). Concentration sensitivity for this method is listed as 5 μg/L S^{2-} (i.e. 95% confidence level) and of the fifty-two total samples analyzed between the influent AMD and reactor R1 effluent, only 5 samples measured sulfide concentrations above the detection limit. Of these five samples, four were collected from the

reactor R1. Overall, sulfide values determined throughout the experiment for the influent and reactor R1(LS) were documented as 3 μg/L S^{2-} (n=26, 1σ = ± 3 μg/L) and 6 μg/L S^{2-} (n=26, 1σ = ± 10 μg/L), respectively. In the bioreactors (R2-R6), sulfide concentrations increased significantly from August-December, 2012; averaging 2.2 mg/L S^{2-} (n=40, 1σ = ± 4.20 mg/L) and reaching values as high as 19 mg/L S^{2-} in reactor R6. An abrupt decline in dissolved sulfide concentrations in all bioreactors (R2-R6) was measured during the low-temperature (T<10°C) months (January- March, 2013), with sulfide values of 15 μg/L S^{2-} (n=20, 1σ = ± 27 μg/L) measured in the R2-R6 effluent. The concentrations of sulfide in all bioreactors (R2-R6) increased to an average value of 4.57 mg/L S^{2-} (n=70, 1σ = ± 3.35 mg/L) from early April to September, 2013.

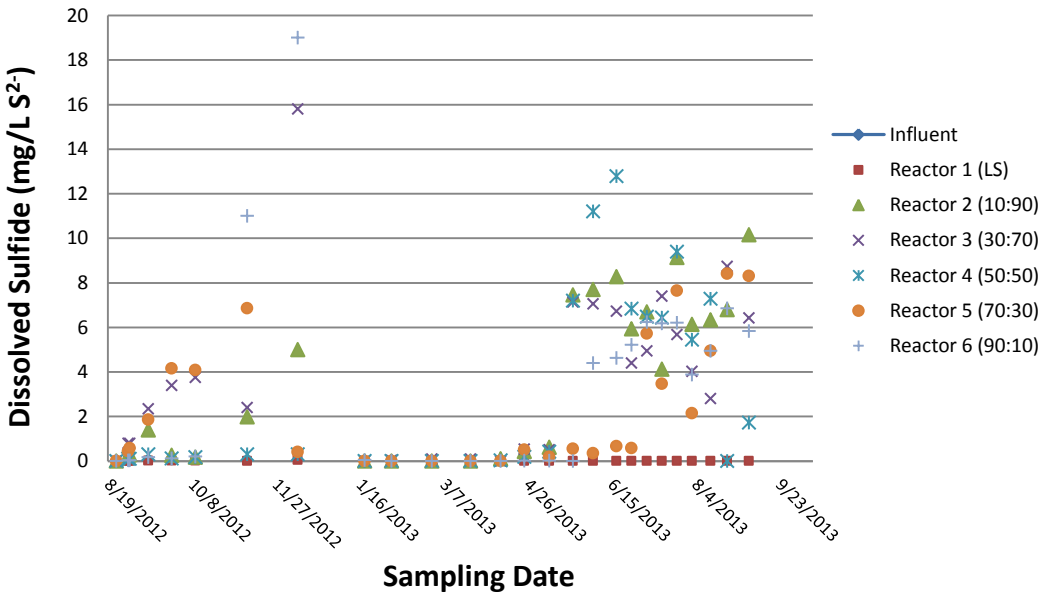

Figure 18: Dissolved Sulfide (mg/L S^{2-}) concentrations measured in AMD influent and reactor effluent samples throughout the course of the experiment.

3.2.4 Iron

The concentration of dissolved iron measured in the influent AMD varied throughout the experiment, with an average concentration of 908 mg/L Fe_T (n=26, 1σ = ± 123 mg/L). From August-December 2012, all reactors displayed large decreases in dissolved iron concentrations as R1 (LS), ligneous (R2, R3), 50/50 mixture (R4) and herbaceous (R5, R6) averaged 379 mg/L Fe_T (n=8, 1σ = ± 241 mg/L), 322 mg/L Fe_T (n=16, 1σ = ± 204 mg/L), 272 mg/L Fe_T (n=8, 1σ = ± 202 mg/L) and 217 mg/L Fe_T (n=16, 1σ = ± 218 mg/L), respectively (Figure 19). As cold temperatures persisted (January-March, 2013), iron concentrations increased in each reactor averaging 445 mg/L Fe_T (n=4, 1σ = ± 200 mg/L) in R1 (LS), 738 mg/L Fe_T (n=8, 1σ = ± 114 mg/L) in ligneous (R2, R3), 663 mg/L Fe_T (n=4, 1σ = ± 33 mg/L) in the 50/50 mixture (R4) and 498 mg/L Fe_T (n=8, 1σ = ± 296 mg/L) in the herbaceous (R5, R6). During the final months of this experiment (April-September, 2013), the herbaceous reactors (R5, R6) recorded the lowest iron concentrations averaging 409 mg/L Fe_T (n=28, 1σ = ± 165 mg/L). Effluent iron concentrations of R1 (LS), ligneous (R2, R3) and 50/50 mixture (R4) averaged 560 mg/L Fe_T (n=14, 1σ = ± 200 mg/L), 616 mg/L Fe_T (n=28, 1σ = ± 137 mg/L) and 498 mg/L Fe_T (n=14, 1σ = ± 116 mg/L) during this time (i.e. April-September, 2013).

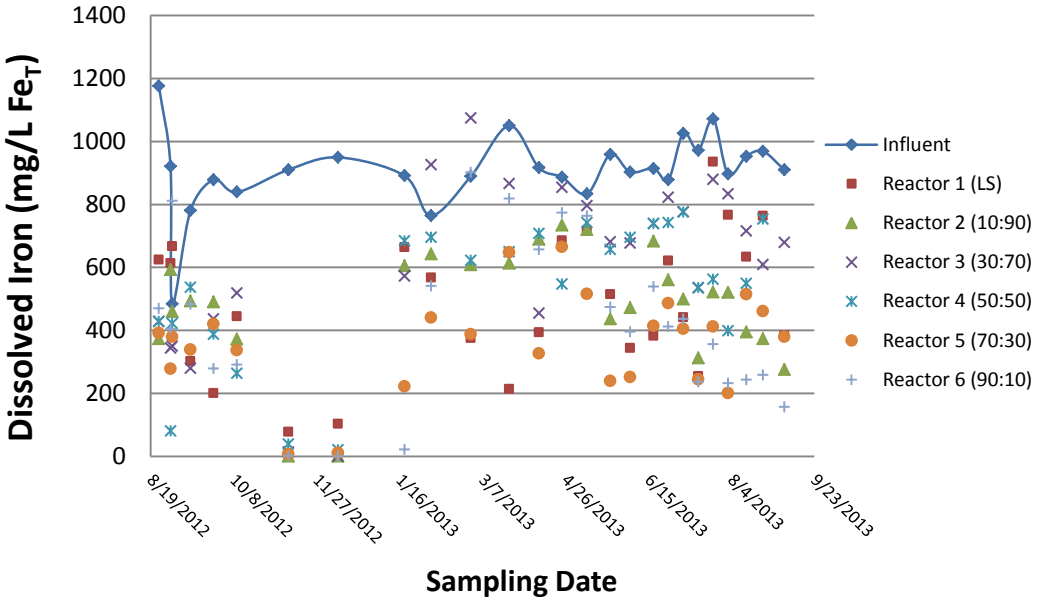

Figure 19: Dissolved iron concentrations (mg/L Fe_T) measured in the AMD influent and effluents of each reactor (R1-R6) throughout the experiment. Fe_T denotes the total concentration of both ferric and ferrous species.

3.2.5 Aluminum

Dissolved aluminum concentrations measured in the influent AMD averaged 198 mg/L Al^{3+} (n=24, 1σ = ± 26 mg/L) throughout the course of the entire experiment. As for the limestone reactor (R1) effluent, the aluminum concentrations averaged 122 mg/L Al^{3+} (n=24, 1σ = ± 39 mg/L). The concentration of dissolved aluminum in the effluent of Reactor R1 was lowest in December 10, 2013 with a value of 12.3 mg/L Al^{3+} (Figure 20). Much lower aluminum concentrations were recorded in the samples taken from the effluents of all bioreactors (R1-R6). Specifically, throughout the entire experiment, average aluminum concentrations of 31.7 mg/L Al^{3+} (n=46, 1σ = ± 35 mg/L), 32.0 mg/L Al^{3+} (n=24, 1σ = ± 35 mg/L) and 17.5 mg/L Al^{3+} (n=48, 1σ = ± 26 mg/L) were measured in the ligneous (R2, R3), 50/50 mix (R4) and herbaceous (R5, R6) reactors, respectively. Overall, the bioreactors (R2-R6) displayed an immediate drop in aluminum concentrations during the first week, a trend which for the most part continued for

roughly the next eight months. During late April 2013, effluent samples taken from the ligneous reactors (R2, R3) began to increase in aluminum concentrations once again but did not reach values higher than those measured in reactor R1 (LS). Increases in aluminum concentrations were subsequently exhibited during the following months in the 50/50 mixture (R4) and then reactor R6 (90:10). Finally, reactor R5 (70:30) displayed a significant increase during mid-august 2013 yet was not as pronounce as the other reactors.

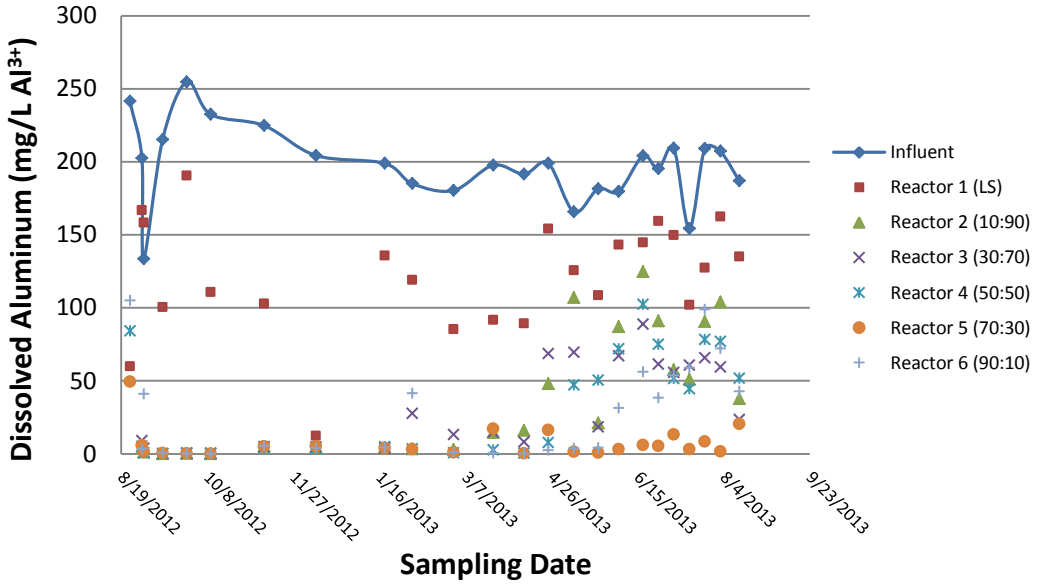

Figure 20: Temporal tends of dissolved aluminum concentrations (mg/L Al^{3+}) in samples taken from the AMD influent and reactor effluent ports (R1-R6) during the course of the experiment.

3.2.6. Manganese

Manganese concentrations measured for the duration of these experiments at the influent AMD port ranged from 35-52 mg/L Mn^{2+} with an average concentration and standard deviation of 43.5 mg/L Mn^{2+} (n=26, 1σ = ± 4 mg/L) (Figure 21). From August 2012 – October 2012, manganese concentration in the limestone reactor (R1) effluent were similar to the manganese concentrations in the AMD influent and measured 43.25 mg/L Mn^{2+} (n=6, 1σ = ± 5 mg/L). As for the bioreactors (R2-R6) average manganese concentrations were higher than influent AMD

for the first three weeks and measured 52.5 mg/L Mn^{2+} (n=20, 1σ = ± 7 mg/L). Average manganese concentrations dropped below influent AMD values in all reactors from late September-December 2012 recording 40.7 mg/L Mn^{2+} (n=4, 1σ = ± 3.4mg/L) in R1(LS), 32.3 mg/L Mn^{2+} (n=8, 1σ = ± 5.1 mg/L) in ligneous (R2, R3), 36.6 mg/L Mn^{2+} (n=4, 1σ = ± 3.2 mg/L) in the 50/50 mixture (R4) and 33.3 mg/L Mn^{2+} (n=8, 1σ = ± 4.2 mg/L). A net increase in effluent manganese concentrations was observed in all reactors from January-March 2013, averaging 44.4 mg/L Mn^{2+} (n=4, 1σ = ± 7 mg/L), 47 mg/L Mn^{2+} (n=8, 1σ = ± 7.7 mg/L), 45.4 mg/L Mn^{2+} (n=4, 1σ = ± 11.2 mg/L) and 43.7 mg/L Mn^{2+} (n=8, 1σ = ± 4.4 mg/L) in R1(LS), ligneous (R2, R3), 50/50 mixture (R4) and herbaceous (R5, R6) reactors, respectively. In the final experimental months (April-September, 2013), influent AMD manganese values averaged 43.9 mg/L Mn^{2+} (n=14, 1σ = ± 2.4 mg/L) while R1 (LS) had slightly lower concentrations of 42.9 mg/L Mn^{2+} (n=14, 1σ = ± 2.7 mg/L). The herbaceous reactors (R5, R6) displayed the lowest effluent manganese concentrations during this time (i.e. April-September, 2013) and recorded 40.9 mg/L Mn^{2+} (n=28, 1σ = ± 3.1 mg/L) whereas the ligneous (R2, R3) and 50/50 mixture (R4) were slightly higher, recording 43 mg/L Mn^{2+} (n=28, 1σ = ± 3.4 mg/L) and 43.3 mg/L Mn^{2+} (n=14, 1σ = ± 4.1 mg/L), respectively.

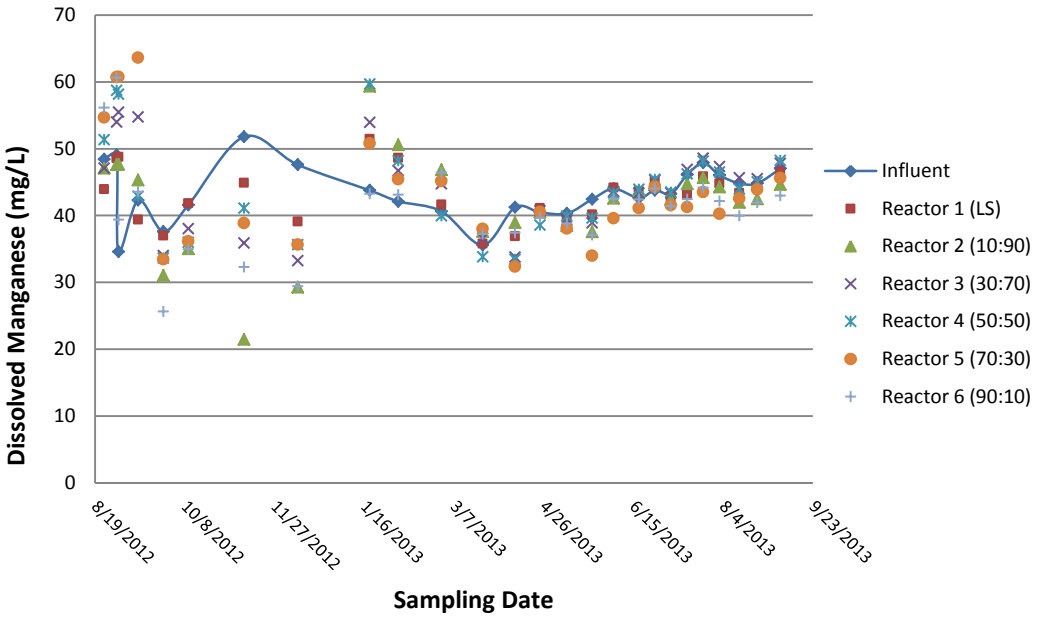

Figure 21: Plot of dissolved manganese (mg/L Mn^{2+}) measured within the AMD influent and reactor (R1-R6) effluents over the course of the experiment.

3.2.7. Calcium

Influent AMD drainage flowing into each reactor contained on average 144 mg/L Ca^{2+} (n=26, 1σ = ± 37 mg/L) that was observed throughout the duration of the experiment. Effluent drainage of the limestone reactor R1 averaged 275 mg/L Ca^{2+} (n=28, 1σ = ± 96 mg/L) with the maximum concentration of 531 mg/L Ca^{2+} which was measured during the first twenty-four hours after it actively received AMD. As for the bioreactors (R2-R6), temporal trends in calcium concentrations were similar to alkalinity, as initial calcium concentrations increased tremendously within the first two weeks reaching values up to 3153 mg/L Ca^{2+} (Figure 22). Such pronounced increases in calcium were short-lived as calcium concentrations in all bioreactors dropped below 800 mg/L Ca^{2+} after just one month (Figure 23). Relative to the limestone reactor (R1), the calcium concentrations measured in the biologic reactors (R2-R6) were substantially greater during this experiment. Still, a steady temporal decline in Ca^{2+} concentration was

observed in all bioreactors (R2-R6), with values decreasing below 400 mg/L Ca^{2+} during the last six months of the experiment .

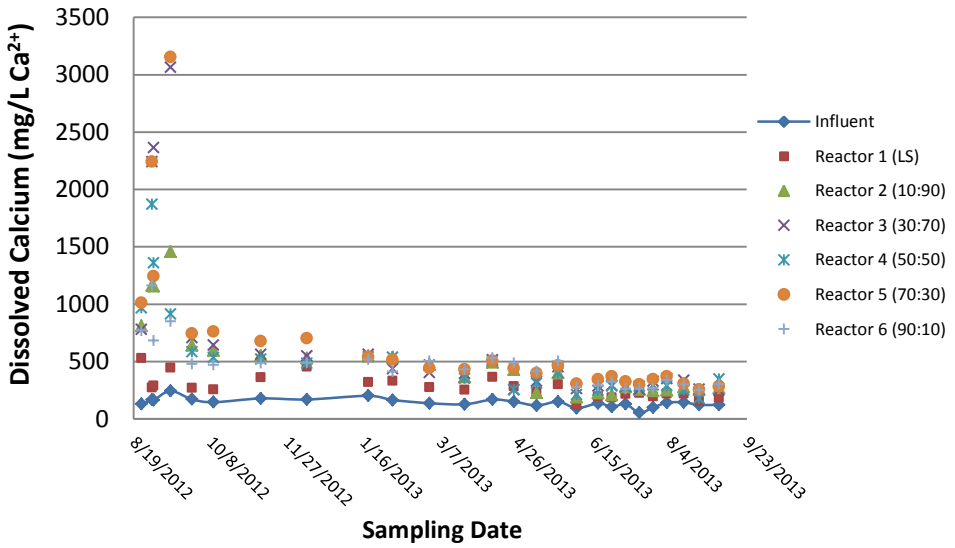

Figure 22: Calcium concentrations measured in samples taken from the AMD influent and effluent port of each reactor (R1-R6) as the experiment progressed.

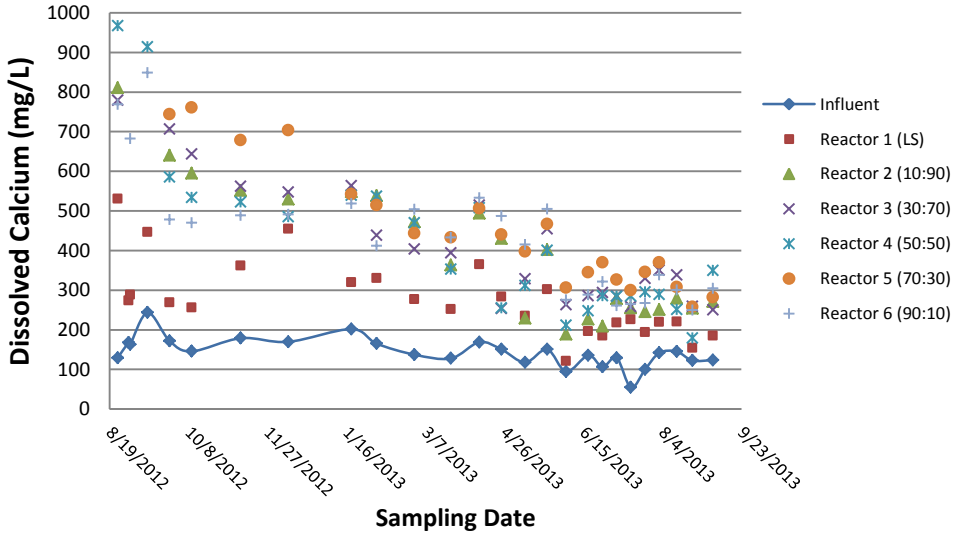

Figure 23: Rescaled view of calcium concentrations (mg/Ca^{2+}) measured in samples taken from the AMD influent and effluent port of each reactor (R1-R6) as the experiment progressed. Calcium concentrations higher than 1000 mg/L Ca^{2+} were not plotted.

3.2.8. Magnesium

Magnesium concentrations measured in the influent AMD were relatively consistent over the 377-day experiment with values averaging near 210 mg/L Mg^{2+} (n=26, 1σ = ± 16 mg/L). Reactor R1 (LS) magnesium concentrations measured higher than influent AMD, with average values of 238 mg/L Mg^{2+} (n=26, 1σ = ± 20 mg/L) (Figure 24). From December, 2012- Late February, 2013, the highest increases in magnesium concentrations were documented in the effluent of reactor 1 (LS) and averaged 252 mg/L Mg^{2+} (n=4, 1σ = ± 25 mg/L). Within the effluent of the biologic reactors (R2-R6), high magnesium concentrations were determined during the initial two weeks of operation reaching values up to 461 mg/L Mg^{2+}. In contrast to trends in calcium concentrations, after the initial two weeks, magnesium concentrations in the bioreactor effluents (R2-R6) were observed as being similar to those of the limestone effluent (R1). A large spike in magnesium concentrations was again observed during 1/19/13 in the all bioreactors as they averaged 310 mg/L Mg^{2+} (n=5, 1σ = ± 18 mg/L). Overall, the ligneous reactors (R2, R3) produced the highest magnesium concentrations 259 mg/L Mg^{2+} (n=52, 1σ = ± 66 mg/L) followed by the herbaceous (R5, R6) 254 mg/L Mg^{2+} (n=52, 1σ = ± 61 mg/L) and 50/50 mixture (R4) 251mg/L Mg^{2+} (n=4, 1σ = ± 65 mg/L) reactors.

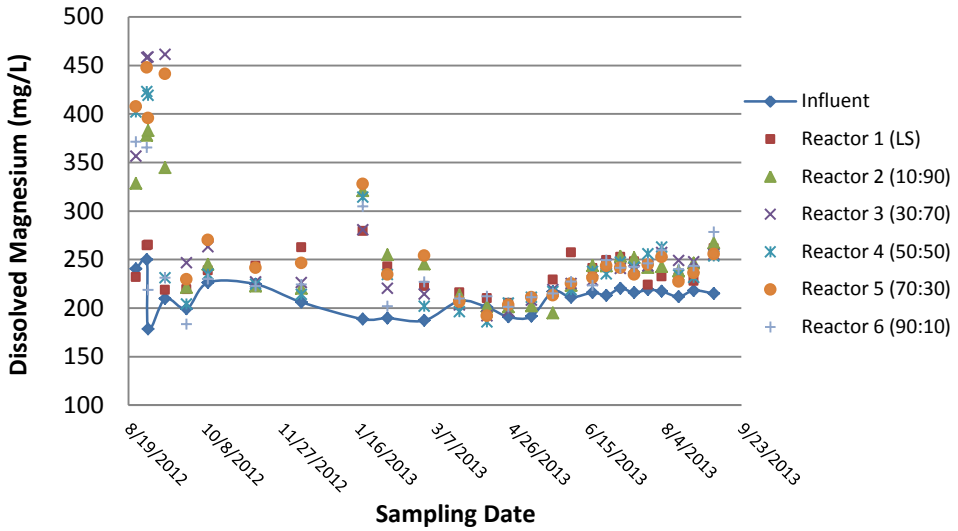

Figure 24: Magnesium concentrations (mg/L Mg^{2+}) measured in the AMD influent and effluent samples of each reactor (R1-R6) during each sampling event.

3.2.9. Chloride

Concentrations of chloride in the influent AMD had averaged 14 mg/L Cl^- (n=26, 1σ = ± 11.5 mg/L) during the course of the experiment. The high variability in AMD influent chloride values resulted from spikes of 22 mg/L Cl^- and 68 mg/L Cl^- during sampling dates 10/10/2012 and 1/19/2013, respectively. Omitting the spikes observed in AMD influent chloride concentrations, values had less variability and averaged 11.5 mg/L Cl^- (n=24, 1σ = ± 2.8 mg/L). The chloride concentrations in the limestone reactor (R1) exhibited similar values to those measured in the AMD influent, with some exceptions when spikes in chloride concentrations were detected. As a result of these spikes, a high overall relative deviation in chloride concentrations was calculated in the limestone reactor (R1), averaging 11.9 mg/L (n=26, 1σ = ± 6 mg/L) over the course of the experiment. Compared to the chloride concentration in the AMD influent, the chloride concentrations within the bioreactors (R2-R6) can be separated in three events: high concentration, medium concentrations and concentrations similar to influent AMD

(Figures 25 & 26). During the first two months of the experiments, in the bioreactors (R2-R6), the average chloride concentrations ranged from 730-1675 mg/L Cl^- with maximum values over 2500 mg/L Cl^-. Subsequent declines in chloride concentrations occurred during the following four months (November 2012- February 2012), when average concentrations ranged between 42-90 mg/L Cl^-. Lastly, during the final six months of the experiment chloride concentrations measured in the samples taken for the effluent of each bioreactor (R2-R6) fell below the average AMD influent values with average concentrations ranging from 9.4-11.5 mg/L Cl^- (Figure 26).

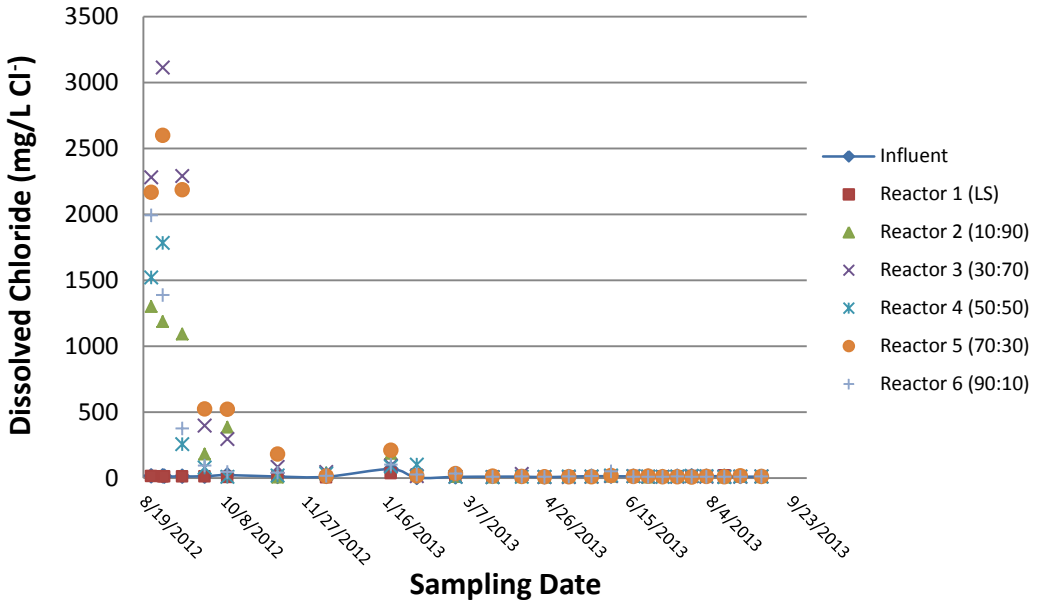

Figure 25: Measured chloride concentrations (mg/L Cl^-) of the AMD influent and the effluent of each reactor (R1-R6) for each sampling event.

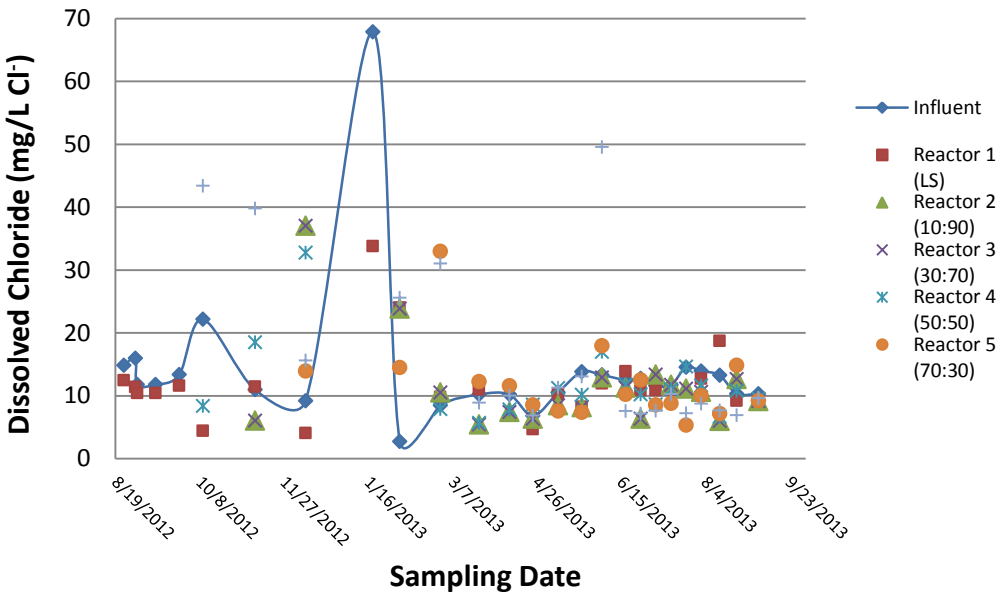

Figure 26 Rescaled view of the chloride concentrations (mg/L Cl^-) in the AMD influent and effluents of each reactor (R1-R6) for each sampling event. Chloride concentrations higher than 70 mg/L Cl^- were not plotted.

3.2.10. Fluoride

Influent fluoride concentrations over the course of this experiment were documented as having large relative fluctuations with an average values of 12.9 mg/L F^-(n=26, 1σ = ± 6.9 mg/L). As for the effluent samples taken from limestone reactor R1, significant removal was documented from the influent AMD in which values averaged 9 mg/L F^- (n=26, 1σ = ± 4.0 mg/L) throughout the entire experiment. In the case of the bioreactors (R2-R6) spikes in fluoride concentrations showed a transition from high, medium to low, which were correlate with the trends measured for chloride concentration values (Figure 27). Within the first two months of operation, the average fluoride concentrations recorded in the effluent samples taken from the bioreactors (R2-R6) ranged between 367-1175 mg/L F^-. During the next four months (November 2012 – February 2013) average fluoride values dropped substantially in each bioreactor (R2-R6) effluent, ranging from 12 to 187 mg/L F^-. Throughout the final six months

(March 2013- early September 2013), effluent fluoride concentrations of the bioreactors (R2-R6) had dropped below average AMD influent values ranging from 5-10 mg/L F^-(Figure 28).

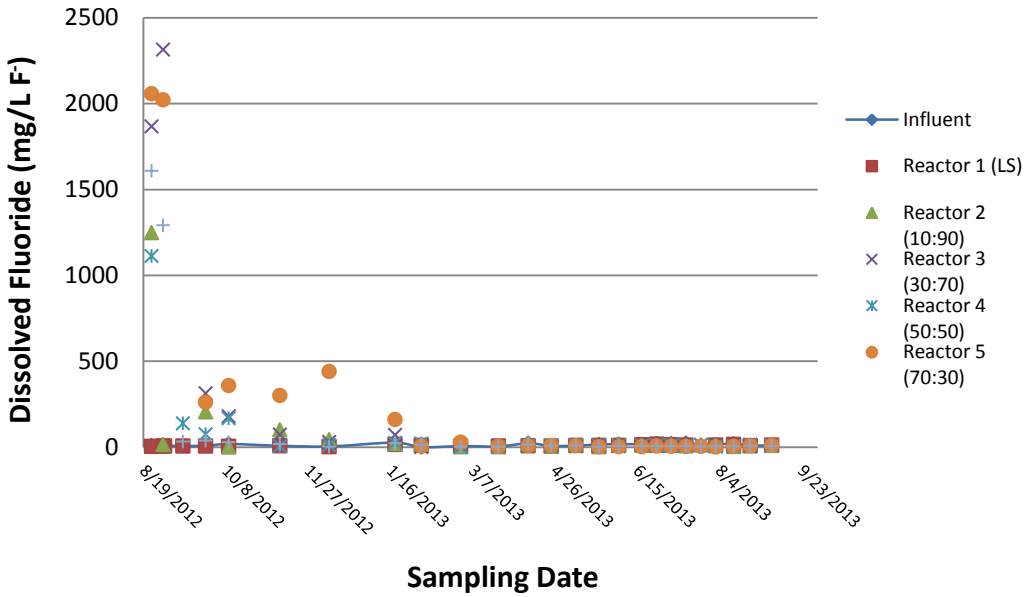

Figure 28: Fluoride concentrations measured in samples taken from influent AMD and effluent ports of all reactors (R1-R6) during the course of this experiment.

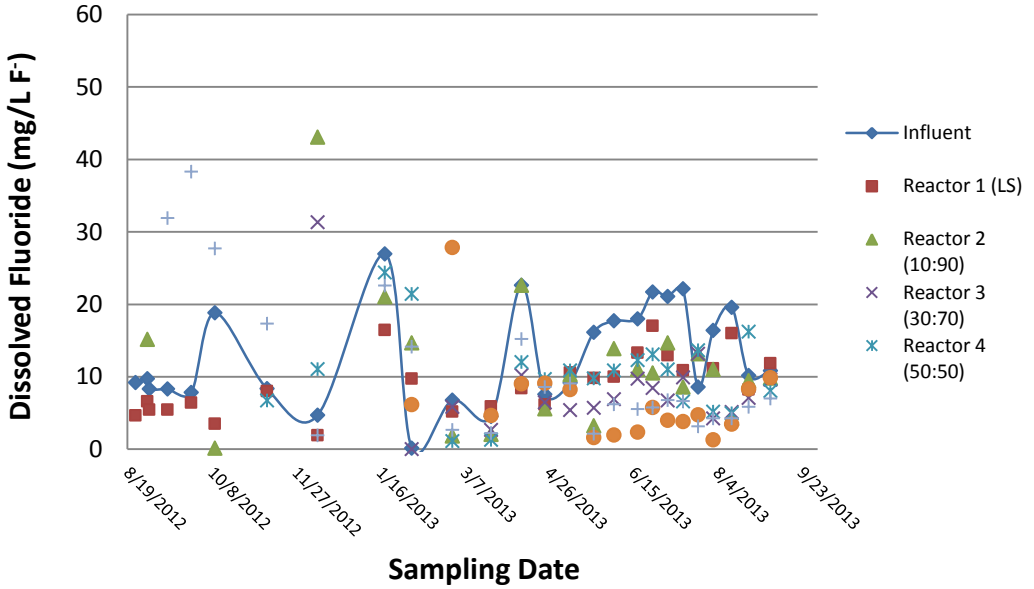

Figure 29: Rescaled view of fluoride concentrations measured in samples taken from influent AMD and effluent ports of all reactors (R1-R6) during the course of this experiment. Fluoride concentration values higher than 60 mg/L F^- were not plotted.

3.3. Trace Metals

3.3.1. Nickel

Throughout this experiment, the concentration of nickel in the AMD influent showed a high degree of relative variability, with an average concentration of 2.05 mg/L Ni^{2+} (n=26, 1σ = ± 0.57 mg/L). Removal of nickel in the limestone reactor (R1) was negligible and in multiple cases a rise in concentration was observed (Figure 30). Of the samples collected for reactor R1, an average nickel concentration of 2.16 mg/L Ni^{2+} (n=26, 1σ = ± 0.66 mg/L) was measured which corresponds to an overall 7.3 mol% increase from the influent drainage. In contrast, the biologic reactors (R2-R6) displayed successful removal of nickel throughout the experiment reaching values below detection (LOD = 10 ppb) in many instances. Initially nickel concentrations slowly declined reaching an average of 1.61 mg/L Ni^{2+} (n=5, 1σ = ± 0.11 mg/L) within the bioreactors (R2-R6) by the end of the third week. Next, large decreases of nickel concentration were observed within the bioreactors from 9/26/2012 to 12/10/2012 with concentrations averaging 0.07 mg/L Ni^{2+} (n=20, 1σ = ± 0.13 mg/L). In the final seven months, nickel concentrations began to slowly increase within the bioreactors averaging 0.39 mg/L Ni^{2+} (n=90, 1σ = ± 0.47 mg/L) during this period. Substrate composition of the bioreactors documented the lowest average nickel concentrations in the herbaceous (R5, R6) 0.506 mg/L Ni^{2+} (n=52, 1σ = ± 0.673 mg/L) over the 50/50 mixture (R4) 0.507 mg/L Ni^{2+} (n=26, 1σ = ± 0.733 mg/L) and ligneous reactors (R2, R3) 0.576 mg/L Ni^{2+} (n=52, 1σ = ± 0.572 mg/L).

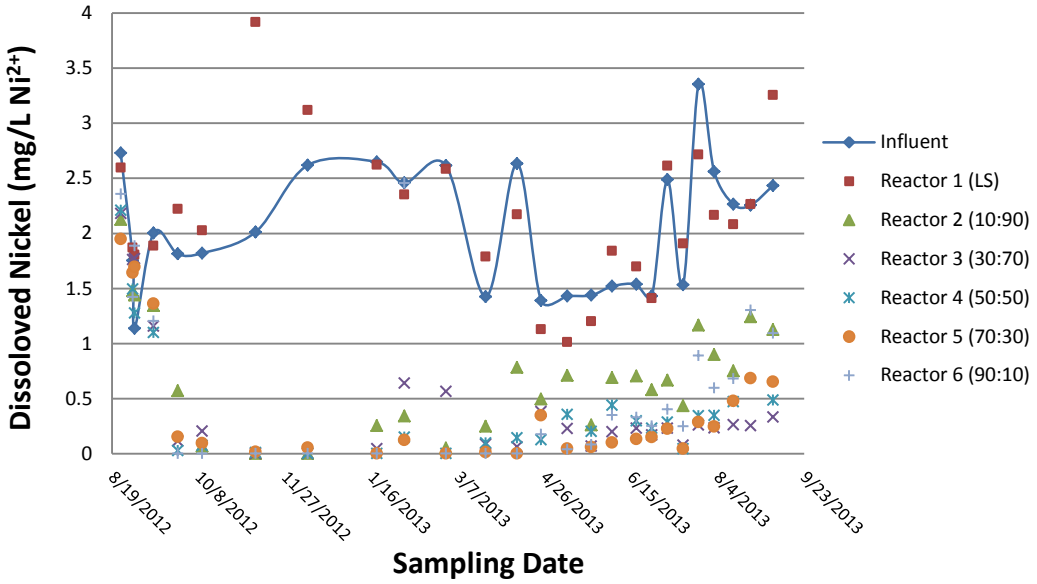

Figure 30: Dissolved nickel concentrations (mg/L Ni^{2+}) measured in the AMD influent and effluent of each reactor (R1-R6) for each sampling event.

3.3.2. Zinc

Influent AMD zinc values averaged 3.35 mg/L Zi^{2+} (n=26, 1σ = ± 0.34 mg/L) during the experiment and had relatively low variability when compared to nickel concentrations. A slight decrease in zinc was found in the majority of effluent samples analyzed from reactor R1as concentrations average 3.13 mg/L Zi^{2+} (n=26, 1σ = ± 0.44 mg/L) overall. In reactor R1, a dramatic removal of 1.68 mg/L zinc was documented in December 2012, followed by 1.09 mg/L and 0.345 mg/L increase in zinc concentrations on January and February 2013, respectively (Figure 31). Biologic reactors (R2-R6) were found to remove zinc exceptionally well. During the first two weeks, concentrations varied immensely between the bioreactors as output values ranged from 0.2-4.2 mg/L Zn^{2+}. After a month of actively receiving AMD, the bioreactors (R2-R6) had all reached effluent zinc concentrations well below 0.5 mg/L Zn^{2+} (Figure 31). Apart from two samples taken from R2 (11/10/12) and R6 (2/4/13), zinc concentrations within all

bioreactors remained near or below detection limit (LOD = 5 ppb) for the majority of the experiment.

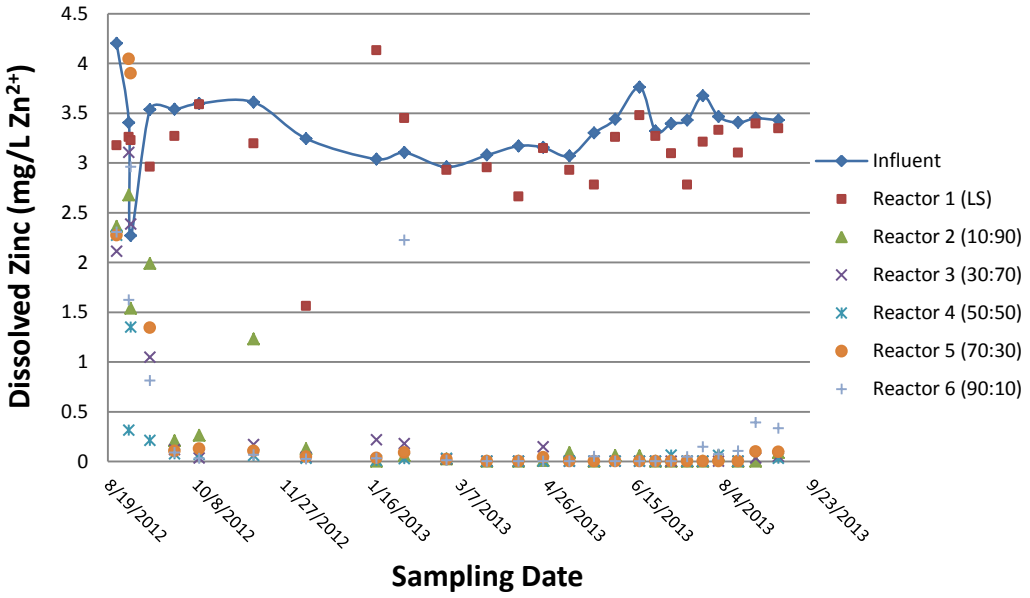

Figure 31: Measured zinc concentrations (mg/L Zn^{2+}) within the influent AMD and reactor effluents (R1-R6) over the course of the experiment.

3.3.3. Cadmium

Aside from a large spike on 9/26/12, cadmium concentrations in the influent AMD remained relatively constant for the duration of the project with an average concentration of 19.5 μg/L Cd^{2+} (n=26, 1σ = ± 6 μg/L) (Figure 32). In the reactor R1 (LS), Cd was removed with varying degrees of success and no appreciable net release of cadmium was observed, as seen in temporal trends of both nickel and zinc. Overall, an average of 14.3 μg/L Cd^{2+} (n=26, 1σ = ± 3 μg/L) was documented from the effluent of R1 (LS) corresponding to an average of 27 mol% cadmium removal. As for the bioreactors (R2-R6), cadmium levels had reach values below the detection limit (LOD = 3 μg/L) a month after the experiment began. Throughout the rest of the

experiment (late Sept. 2012- Sept. 2013), cadmium concentrations dropped below 5 µg/L within all the bioreactor (R2-R6) samples.

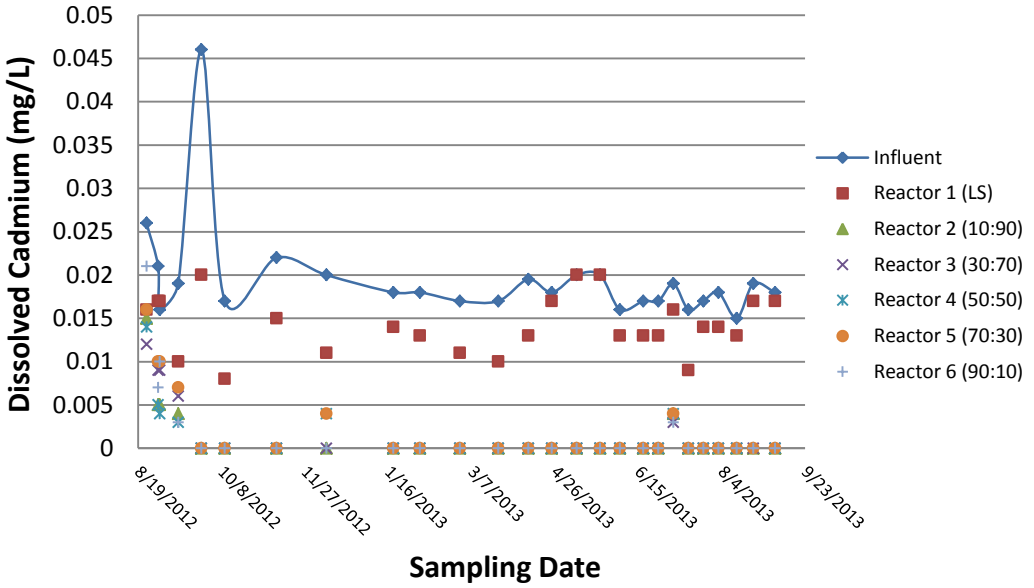

Figure 32: Influent AMD and reactor effluent (R1-R6) cadmium concentrations (mg/L Cd^{2+}) determined for each sampling event.

3.3.4. Copper

Dissolved copper concentrations in the AMD influent displayed large relative temporal fluctuations with an average concentration of 37 µg/L Cu^{2+} (n=26, 1σ = ± 15 µg/L). Significant removal of copper was exhibited in the limestone only reactor (R1), as an average of 17 µg/L Cu^{2+} (n=26, 1σ = ± 15 µg/L) was recorded in the effluent, which corresponded to 53.8 mol% removal. In the biologic reactors (R2-R6), copper concentrations dropped below detection (LOD = 3 µg/L) within the first month of operation. This trend continued for all biologic reactors (R2-R6) for the majority of the experiment (Figure 33). However, two large spikes in copper concentrations were recorded in January 2013, reaching concentration values of 95 and 30 µg/L Cu^{2+} within reactor R3 (30:70) and reactor R4 (50:50), respectively. Still, high copper removal

percentages were characteristic of the bioreactors (R2-R6) during this experiment, with average copper removal percentages ranging from 67-92 mol%.

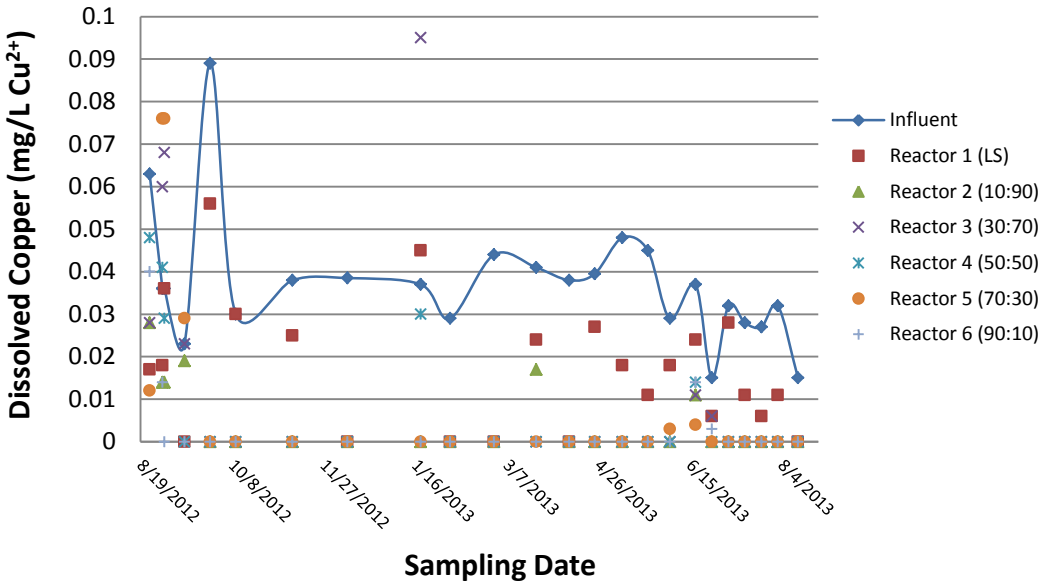

Figure 33: Measured copper values (mg/L Cu^{2+}) within the AMD influent and effluents of all reactors (R1-R6) over the course of the experiment.

3.3.5. Strontium

Dissolved strontium concentrations in the influent AMD were mostly below detection limit (LOD = 10 µg/L) yet on occasions reached levels near 0.1 mg/L Sr^{2+}. Strontium values increased by two orders of magnitude in early effluent samples taken from bioreactors R3 and R5 recording 13.5 and 11.1 mg/L Sr^{2+}, respectively (Figure 34). Strontium concentrations fell below 4 mg/L after a month of operation and continued to slowly decline throughout the experiment. Reactor 1 (LS) effluent displayed relatively low amounts of dissolved strontium when compared to the biologic reactors, yet was still significantly higher than influent strontium concentration levels (Figure 35). Throughout the entire experiment, average strontium concentration outputs were recorded as 0.464 mg/L Sr^{2+} (n=26, $1\sigma = \pm 0.674$ mg/L) in the limestone only reactor (R1), 1.489 mg/L Sr^{2+} (n=52, $1\sigma = \pm 2.359$ mg/L) for the ligneous

reactors (R2, R3), 1.243 mg/L Sr^{2+} (n=26, 1σ = ± 1.487 mg/L) in 50/50 reactor (R4) and 1.4 mg/L Sr^{2+} (n=52, 1σ = ± 1.840 mg/L) in the herbaceous reactors (R5, R6).

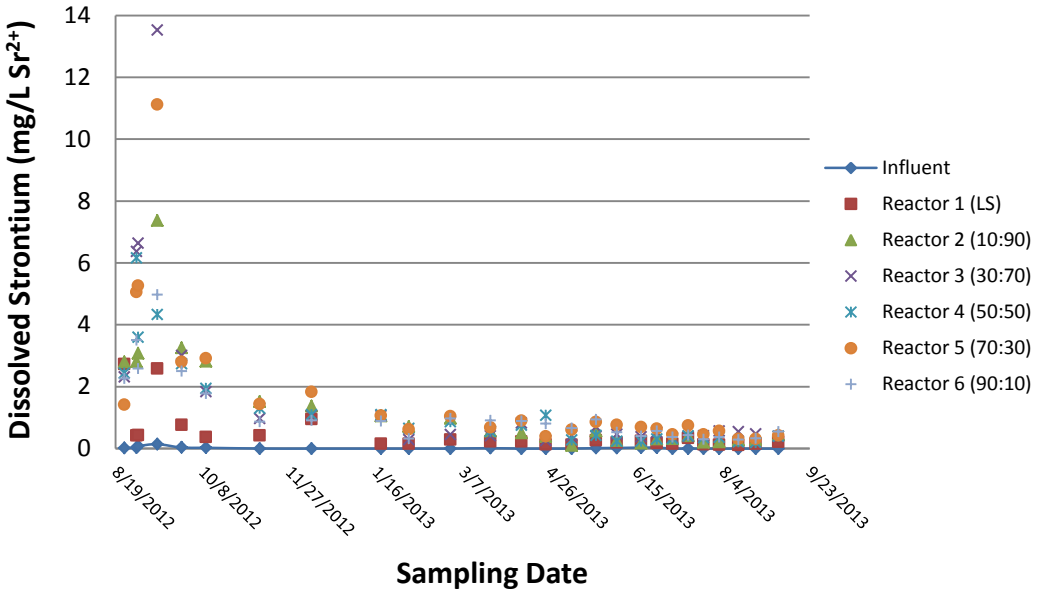

Figure 34: concentrations (mg/L Sr^{2+}) detected in AMD influent and reactor effluents (R1-R6) at each sampling event.

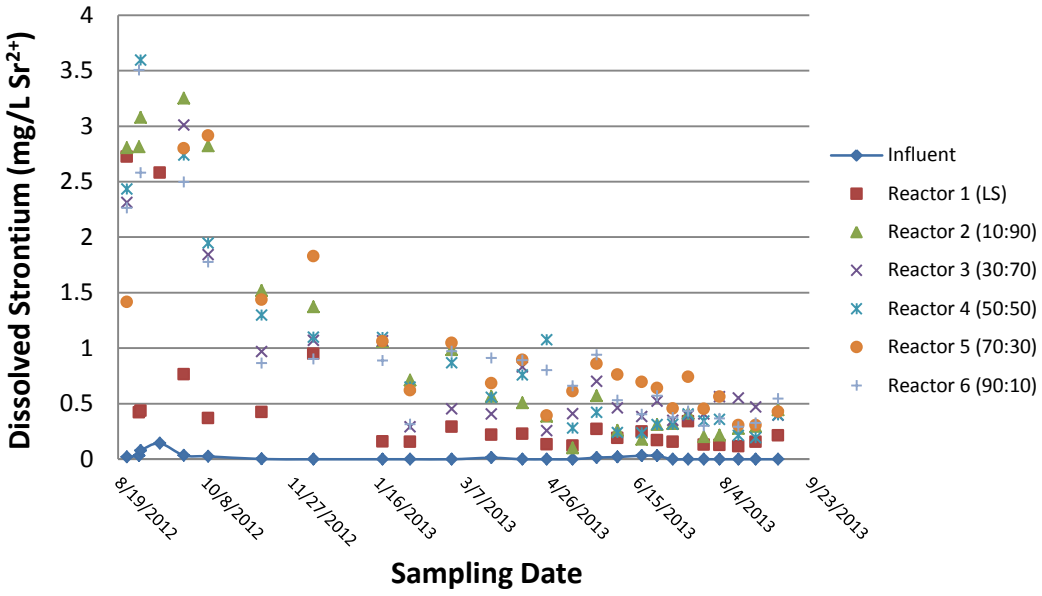

Figure 34: Rescaled view of strontium concentrations (mg/L Sr^{2+}) detected in AMD influent and reactor effluents (R1-R6) at each sampling event. Strontium concentrations higher than 4 mg/L were not plotted.

3.3.6. Potassium

In the influent AMD, the potassium concentrations remained relatively constant throughout the course of the experiment and averaged 7.4 mg/L K^+ (n=26, $1\sigma = \pm 1.6$ mg/L). A minor removal of potassium was documented in the effluent of the limestone only (R1) reactor, which showed average potassium concentrations of 7.2 mg/L K^+ (n=26, $1\sigma = \pm 1.5$ mg/L). The bioreactors (R2-R6) displayed distinct temporal trends in potassium concentrations compared to those measured in the AMD influent, in which concentration went from high, to medium, to low during the experiment. Potassium content was high throughout the initial two months as the average values recorded from all bioreactor effluents (R1-R6) ranged from 81-442 mg/L K^+ (Figure 35). Over the following four months (November 2012- February 2013), potassium concentrations declined in all five bioreactor (R2-R6) effluent drainages as average potassium concentrations ranged between 8.5-12.3 mg/L K^+ (Figure 36). Still, during the final month's bioreactor (R2-R6) potassium concentrations remained above the recorded influent AMD values indicating a net release of potassium continued throughout the experiment.

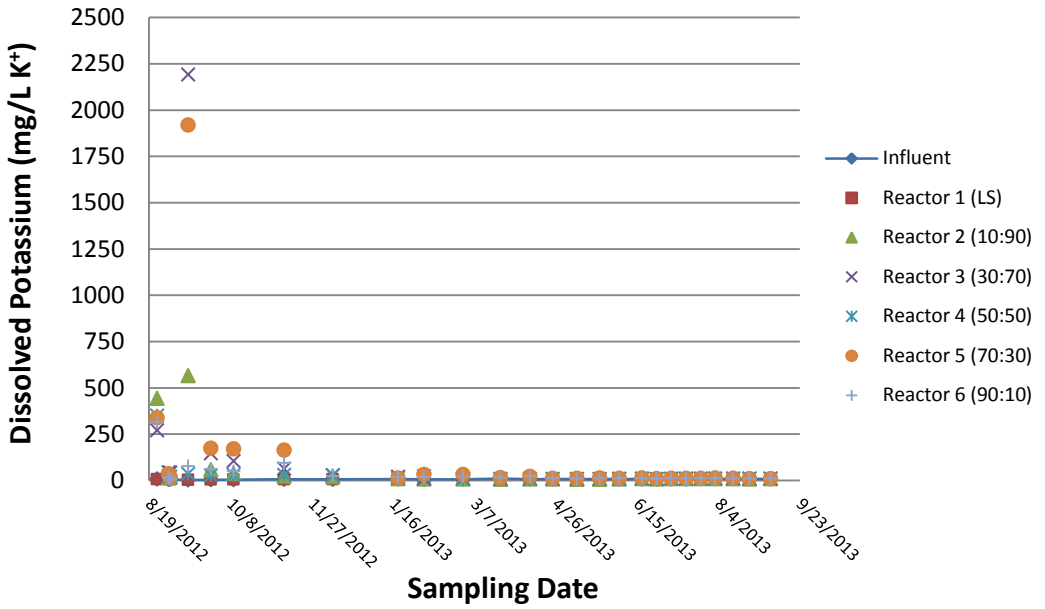

Figure 35: Dissolved potassium concentrations through time showing measured potassium of influent AMD and each reactor effluent (R1-R6) throughout the entire experiment.

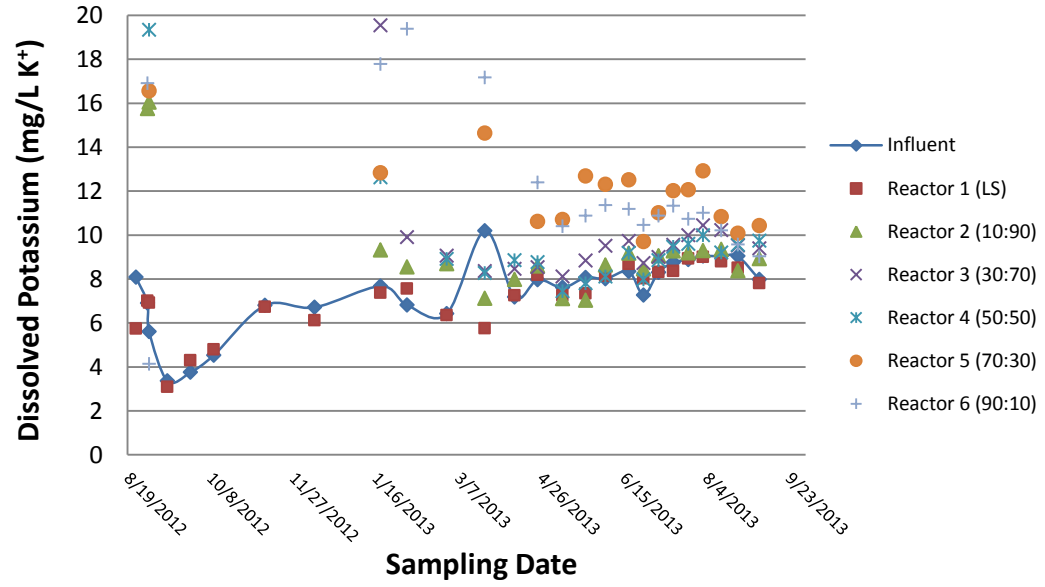

Figure 36: Rescaled view of measured potassium of influent AMD and each reactor effluent (R1-R6) throughout the entire experiment. Potassium concentrations higher than 20 mg/L were not plotted.

3.3.7. Sodium

Dissolved sodium concentrations measured in the influent drainage displayed a large spike during 9/26/2012 of 162 mg/L Na^+. Aside from this large spike, the average sodium concentrations measured in the influent AMD were relatively constant and averaged 30.2 mg/L Na^+ (n=25, $1\sigma = \pm 5.4$ mg/L). Effluent measurements for reactor R1 (LS) also exhibited a spike in sodium on 9/26/2012 reaching 72 mg/L Na^+ but overall reactor R1 exhibited a subtle decline in sodium concentrations during active treatment as the calculated average was 30.2 mg/L Na^+ (n=25, $1\sigma = \pm 3.64$ mg/L) for this test cell. Again, the bioreactors (R2-R6) displayed an evolution from high to medium and low sodium concentrations as time progressed. Initially, from August to October 2012, within the bioreactors (R2-R6), sodium concentrations ranged from 41-137 mg/L Na^+ (Figure 37). Then, during the next four months (November 2012-February 2013), average concentrations decreased within the bioreactor effluents, with concentrations ranging from 32-55 mg/L Na^+. All bioreactor sodium concentrations then dropped near the AMD influent concentrations, with an average of 32 mg/L Na^+ in the final six months (Figure 38).

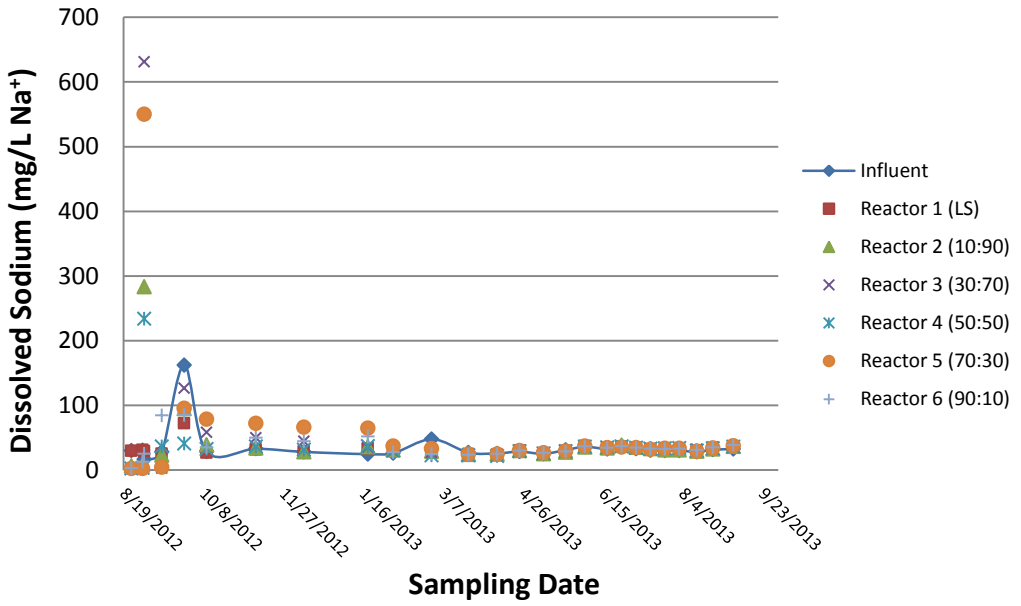

Figure 37: Measured sodium concentrations (mg/L Na^+) in the AMD influent and effluent samples of each reactor (R1-R6) during the course of the experiment.

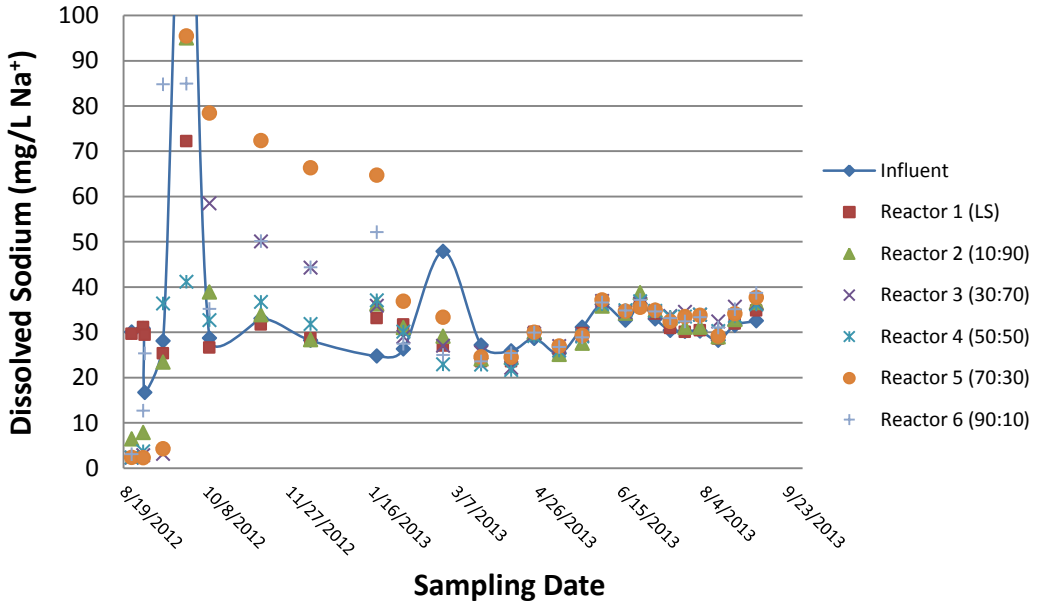

Figure 37: Rescaled view of Measured sodium concentrations (mg/L Na+) in the AMD influent and effluent samples of each reactor (R1-R6) during the course of the experiment. Sodium concentration values higher than 100 mg/L were not plotted.

CHAPTER 4

DISCUSSION

4.1. Solution Parameters

4.1.1 Experimental Conditions Summary

The experimental reactors (R1-R6) have actively received AMD for the duration of the research at an average rate of ~5mL/min directly from the main seep at the Tab-Simco AML site. Throughout the experiment, the influent AMD was consistently composed of acidic waters (pH=2.80) with high concentrations (ppm) of dissolved constituents: 900 Fe_{Total}, 200 Al, 40 Mn and 5000 SO_4^{2-}, along with significant amounts of trace elements (Figures 30-33). Although, daily precipitation events as much as 6.73cm (2.65'') in the area caused diel physicochemical fluctuations in the AMD influent (i.e. contaminant plumes, AMD dilution), these changes were short-lived and of minor significance when compared to the long-term trends. During these experiments, the local air temperature displayed a wide range of values, from -13 to 35^0C (8 to 96^0F); thus, playing a substantial role in controlling the rate of both chemical and biological processes and controlling the efficacy of the bio-induced remediation within bioreactor test cells.

4.1.2 Temperature Effects on ASBR Technology

Reactor outflow temperatures recorded in the field closely resembled that of the average local air temperatures (Figure 9) and dramatically disrupted biologic activity during the winter season. The concentration of gaseous O_2 in the aqueous phase was documented as displaying a cyclical trend within the acid impoundment of all reactors (R1-R6) (Figure 15). Specifically, from the influent AMD to the acid impoundment (AI) of each reactor (R1-R3), initial warm

temperature months (T>10°C) resulted in a depletion of dissolved oxygen (DO) while the cold temperature months (T<10°C) documented increases in DO. Then as temperatures began to rise in the final months, DO concentrations decreased within the AI's of each reactor (R1-R6) once again. Evaluation of the DO concentrations in the acid impoundment against the measured temperatures shows a negative correlation between the two parameters (Figure 38). Temperature is known to play a large role in the solvation of gases such as $O_2(g)$ in aqueous solution, therefore, increase in DO concentrations as temperatures decrease is expected (Manahan, 2010). The data also demonstrates minor differences between DO concentrations in the AI of the limestone reactor (R1) and biologic reactors (R2-R6) as a function of temperature (Figure 38). However, during the warmer biologically-active months, measurable decreases in DO values were recorded from the influent AMD to the AI's of all reactors (R1-R6). These results suggest that the acidophilic iron oxidizing *proteobacteria* such as *At. Ferrooxidans*, which comprised the majority of microbial communities found at the uppermost portion of each reactor, may play an important role in reducing $O_{2(aq)}$ and subsequently oxidizing ferrous iron (Pugh, 2013; Wang et al., 2013). Furthermore, superoxide and peroxyl radical generation by the photolysis of $O_{2(aq)}$ is induced by solar radiation entering the uppermost portion of each reactor may also enhance oxygen decomposition during warm temperature months (Garg et al., 2013).

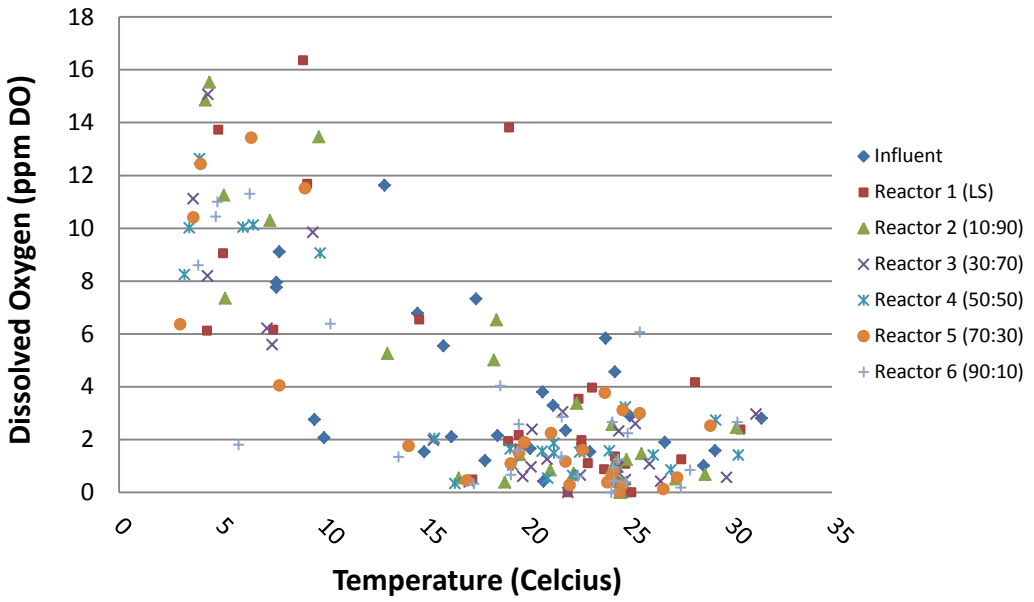

Figure 38 Plot displaying dissolved oxygen concentrations (ppm DO) versus the recorded field temperatures of the influent AMD and the acid impoundments of each reactor (R1-R6).

The establishment of an anoxic environment is commonly associated with cultivating active sulfate reducing bacteria and, therefore, is a key ingredient in the performance of bioreactor technology (Johnson & Hallberg, 2005). Although during the initial week of the experiment, the DO concentrations in the effluent of all bioreactors (R2-R6) were near 0ppm, these anoxic conditions were not maintained throughout the rest of the experiment. DO concentrations from the AI to the effluent ports of each reactor decreased as the air temperatures decreased (Figure 16) which contradicts the temperature dependency in the solvation of gaseous $O_{2(g)}$ into water. This also corresponded to an increase in dissolve iron, manganese, copper, nickel and zinc during the cold temperature months.

Net consumption of oxygen from the acid impoundment to the effluent port of each reactor (R1-R6) implies that oxidative processes had shifted deeper into all reactors during cold temperature months. As a result, processes such as oxidative-dissolution and decreases in precipitation kinetics would produce disturbances in these reactors influencing destabilization of

both mineral phases and adsorbed species (Edwards et al., 2000). Oxidative-dissolution would have affected the bioreactors (R2-R6) to a greater extent over the limestone only reactor (R1) since it had never developed conditions suitable for sulfide formation (i.e. reducing). During the early months of operation, high concentrations of sulfide and low ORP values suggested that reducing conditions were present in the bioreactors. These conditions are necessary for the precipitation and accumulation of metal sulfide phases. Therefore, as the conditions in the bioreactors changed (e.g., during cold months), such phases could have been subject to oxidative dissolution as outlined in equation 1.

This process could explain the net consumption of $O_{2(aq)}$ at depth during colder months along with the notable increases in dissolved metals, especially iron and manganese in the effluent of the bioreactors. Dissolved sulfide can incorporate a wide variety of divalent metal cations into a crystalline phase, yet not all mineral phases possess equivalent stabilities in an aqueous medium (i.e. MnS (pK_{sp}=10.5-13.5), FeS (pK_{sp}=18.1), NiS (pK_{sp}=19.4-26.6), ZnS (pK_{sp}=24.7), CuS(pK_{sp}=36.1-48.5)) (Harris, 2010). Consequently, since MnS and FeS are the most soluble of these phases, they would be subject to oxidative dissolution over NiS, ZnS and CuS. However, during the low-temperature months effluent of the limestone only reactor (R1) also exhibited decreasing $O_{2(aq)}$ and increasing $Fe_{(aq)}$ concentrations; thus, another mechanism must be considered to fully explain the data-set.

Since reactor R1 did not exhibit conditions suitable to promote biologic sulfate reduction processes, declines in the DO concentrations are not associated with the oxidation of sulfide phase at depth as the temperatures dropped. One possible explanation could be that the same mechanism for ferrous iron oxidation occurring in warm temperatures occurred in all the reactors during the cold months; however, at a decreased rate due to slower reaction kinetics at low

temperatures. The oxidation of ferrous iron into ferric iron results in a net consumption of $O_{2(aq)}$ according to equation 2. Excessive release of protons through the hydrolysis of ferric iron (equation 3) and the subsequent slow precipitation of additional oxide phases would cause a displacement of adsorbed cations (magnesium, zinc) on the oxo-bridges of previously formed iron oxyhydroxides through proton exchange (Kim et al., 2008; G. Lee, Bigham, & Faure, 2002).

In addition, slow precipitation of iron oxides would deter intercalation of trace metals within the crystalline structure and such species would remain in solution. Equations 2 & 3 would also explain the consumption of dissolved oxygen along with the release of trace metals observed during the colder months. Still, in the biologic reactors (R2-R6), oxidative-dissolution would remain the dominant cause for the decreases in metal attenuation as protons produced during ferrous oxidation would be less available for cation exchange on oxide surfaces due to the circum-neutral pH observed in these reactors during the colder months (Figure 11).

4.1.3 Effect of Redox Transitions on Bioreactor Efficiency

Dynamic redox environments in the bioreactors (R2-R6) were measured during the course of this experiment in contrast to the relatively continuous redox environments in the limestone reactor R1. In reactor R1 (LS), effluent ORP measurements followed similar trends to that of the AMD influent. Aside from the low-temperature months all bioreactor effluents (R2-R6) exhibited a large decrease in ORP values throughout the duration of the experiment. To further describe the transitions in oxidation-reduction potential, changes in ORP values were calculated from influent to acid impoundments (eq.10) and acid impoundments to effluent ports (eq.11) as a function of time (Figures 39 &40).

$$ORP_{AI}\,(mV) - ORP_{In}\,(mV) = \Delta ORP_{In \rightarrow AI}\,(mV) \quad (10)$$

$$ORP_{Eff}\ (mV) - ORP_{AI}\ (mV) = \Delta ORP_{AI \rightarrow Eff}\ (mV) \quad (11)$$

Where the ORP (mV) values of the influent AMD, AI of and effluent each reactor are represented by ORP_{In}, ORP_{AI} and ORP_{Eff}, respectively. Thus, positive ΔORP (mV) represents an increase in ORP while a negative ΔORP (mV) represents a decrease in ORP from the influent AMD to the reactor AI ($\Delta ORP_{AI \rightarrow Eff}$) or the reactor AI to the reactor effluent ($\Delta ORP_{AI \rightarrow Eff}$) .

The acid impoundment of the limestone reactor (R1) exhibited increases in ORP values from AMD influent with ΔORP > 0 throughout the duration of the experiment (Figure 39). Since the formation of iron oxyhydroxides (FeOOH) is the prevalent process occurring within reactor 1 (R1), this is potentially the process that influenced ORP values to increase within the acid impoundment. Similar redox trends were shown to occur in experiments using mixed cultures of *A. ferrooxidans* in which a direct correlation was observed between the ORP values and the oxidation of ferrous iron (Wang et al., 2013).

In the bioreactors (R2-R6), temporal changes in ORP values from influent AMD to each acid impoundment represent a transition from decreasing to increasing ORP measurements (Figure 39). This trend inversely mimics the changes in pH within the acid impoundments of the bioreactors (Figure 10), as they went from initial increases to decreases in pH values when compared to AMD influent. During the first week of operation, DNA sequencing of the AI's and effluents of the bioreactors (R2-R6) identified the presence of *Clostridia* and *Bacilli* which contain several OTU's capable of fermentation and cellulosic degradation. Active fermentation processes occurring at the uppermost portions within the bioreactors would explain the decline in $\Delta OPR_{IN \rightarrow AI}$ measured during the initial months. Substantial decreases in pH and increases in ORP values from the influent AMD to the AI of each bioreactor were recorded from January-Sept. 2013. This implies that oxidation of ferrous iron and hydrolysis of ferric iron controlled the

AI chemistry during the late stage of the experiment, which may have been facilitated by acidophilic iron oxidizing bacteria. Supporting evidence from microbial analyses showed a strong increase in chemolithotrophs in the upper portions of the bioreactors from August 2012 to May 2013 (Pugh, 2013).

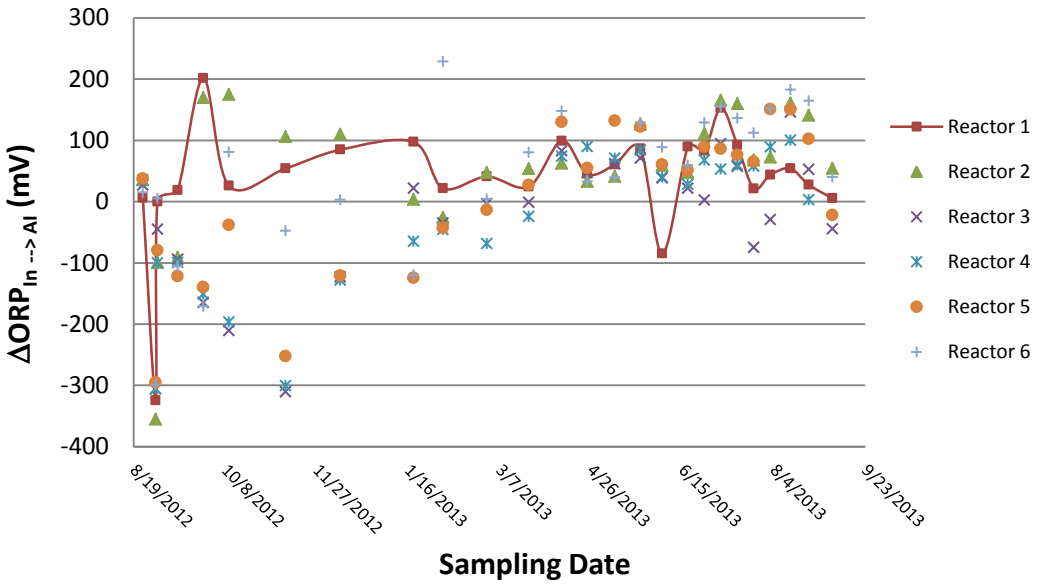

Figure 39 Calculated changes in ORP values ($\Delta ORP_{In \rightarrow AI}$) from the influent drainage to the acid impoundments of each reactor (R1-R6) during each sampling event.

Although the effluent of the limestone reactor R1 maintained a positive ORP value averaging 211mV, when compared to its acid impoundment, the R1 effluent ORP values decreased consistently throughout the experiment (Figure 40). As ferric iron undergoes hydrolysis at the uppermost portion of the reactor, relative ratios of ferric to ferrous iron would decrease causing a corresponding decrease in ORP (Hiroyoshi et al., 2001). At the beginning of the experiments, bioreactors displayed a decreasing trend in ORP values suggesting that the acid impoundments had more oxidizing conditions. During the cold months differences between AI and effluent ORP values ($\Delta ORP_{AI \rightarrow Eff}$) decreased in all bioreactors (R1-R6). Reducing environments were not maintained throughout the low temperature months (late December 2012

to April 2013) implying oxidative conditions were likely present at depth in each bioreactor as seasonal changes ensued. This trend corresponds with the decrease in DO concentrations that occurred at depth during this time, indicating that oxidative dissolution of sulfide phases would cause an increase in bioreactor (R2-R6) effluent ORP values.

From late February to August 2013, significant decreases in ORP values were measured within the bioreactors (R2-R6) between their acid impoundments and effluents, with ΔORP's reaching up to 800 mV on 6/4/2013. Such large redox differences are commonly associated with the biological degradation of organic material introduced by highly active microbial communities. The reducing conditions created are favorable for microbial sulfate reducing processes (Christensen et al., 1996; Muyzer & Stams, 2008; Neculita et al., 2008). Isolated bacteria from sulfate-reducing enrichments showed that members closely related to the *Desulfovibrio* genus were present in the bioreactors (R2-R6), suggesting that these communities were responsible for the sulfate reduction processes that occurred within each bioreactor (Pugh, 2013).

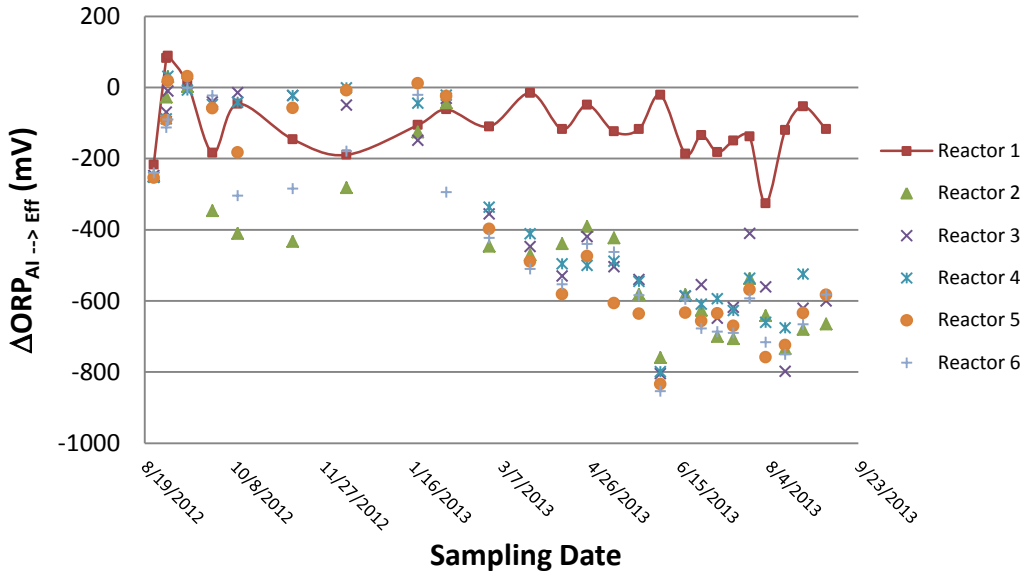

Figure 40 Calculated changes in ORP values (ΔORP) from the AI→Effluent of each reactor (R1-R6) during the experiment.

4.2. Treatment Efficacy

4.2.1. Biologic and Abiologic Effects on pH Values

Measured pH values in the limestone reactor (R1) effluent displayed an average increase of 0.54 units (n=26, 1σ = ± 0.35 units) from the influent AMD, yet never recorded values high enough to produce alkalinity (e.g., pH > 4.5). Still, an overall average increase of 131 mg/L Ca^{2+} (n=26, 1σ = 79 mg/L) dissolved calcium from the AMD influent was produced within the limestone reactor suggesting precipitate formation in R1 had not completely disrupted $CaCO_{3(s)}$ dissolution. In contrast to the limestone reactor (R1), all bioreactors displayed a considerably higher amount of calcium released throughout the course of the experiment. Since all reactors (R1-R6) contained the same volumes of limestone, the additional organic substrate included in biologic reactors had an important contribution to maintaining higher calcite dissolution rates, probable due to less armoring of the calcite in these bioreactors. The armoring of limestone by

precipitates occurred rapidly within the limestone only reactor (R1), while the presence of increased surface area offered by organic matter in the bioreactors had slowed the armoring process and promoted relatively higher rates of calcite dissolution, and thus higher alkalinity in the bioreactors (R2-R6).

Substantial increase in pH within the biologic reactors (R2-R6) has been suggested to be induced by microbial-mediated reduction of strong sulfuric acid (pKa ~ -3.0) into a relatively weak hydrogen sulfide (pKa ~ 7) via the following equation (Johnson & Hallberg, 2005):

$$SO_4^{2-}{}_{(aq)} + 2CH_2O + 2H^+{}_{(aq)} \rightarrow H_2S_{(aq)} + 2H_2CO_{3(aq)} \quad (12)$$

To constrain whether hydrogen sulfide production within the bioreactors played a significant role in increasing effluent pH values, the net increase in dissolved calcium, strontium and magnesium were used as a proxy for total limestone dissolution at any given sampling event (Figure 41). Also, bioreactor (R2-R6) total limestone dissolution (TLD) values during later sampling events (i.e. 4/24/13 – 9/5/13) were compared to all TLD values of reactor R1 since 1) concentration of calcium, strontium and magnesium fell within a comparable range and 2) bioreactor samples all contained high dissolved sulfide concentrations during this time. The biologic reactors (R2-R6) exhibit higher pH values during months when the effluent had high sulfide concentrations and the total limestone dissolution values were comparable with reactor R1. This would be expected as hydrogen sulfide is a weaker acid relative to sulfuric, causing the free proton concentration to decrease as sulfate is reduced to sulfide.

Overall, results from this experiment suggest that calcite dissolution plays an important role in promoting alkalinity and raising pH, yet sulfide formation can also have a positive impact on increasing the pH of acidic solutions. However, in bioreactor technology, the primary goal is not to utilize hydrogen sulfide as a source of alkalinity but as a species that reacts with divalent

metals and forms sulfide minerals. To achieve metal removal hydrogen sulfide must be fully deprotonated. Consequently, it is important that the bioreactor maintains optimal pH values not only for the microbial sulfate reduction processes, which convert sulfate to hydrogen sulfide, but also for the sequestration of hydrogen sulfide in sulfide minerals.

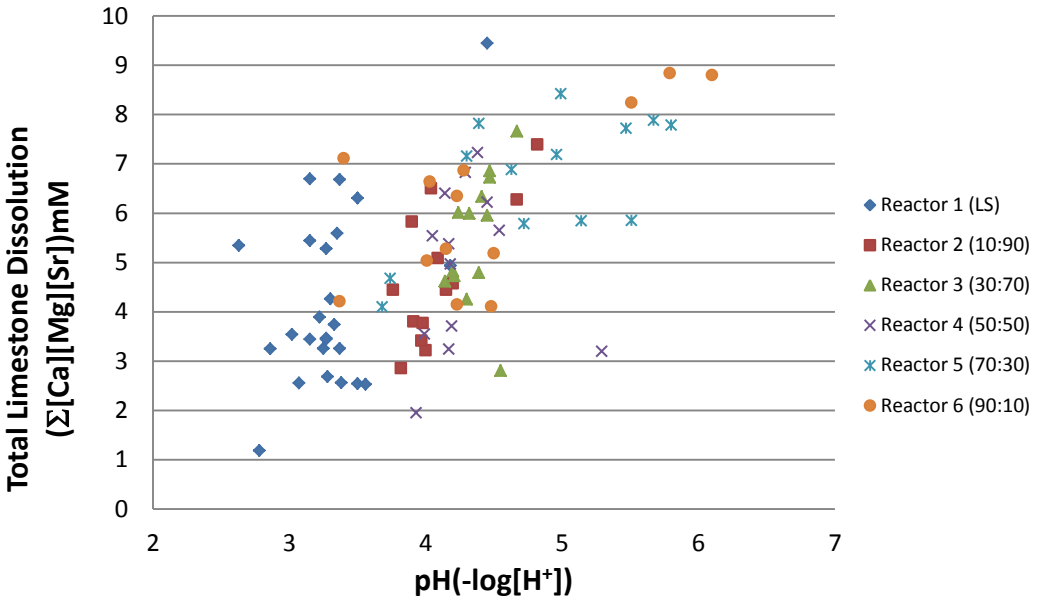

Figure 41 Plot of the summation of net increases in calcium, magnesium and strontium concentrations (i.e.Total Limestone Dissolution (TLD)) from influent AMD within each reactor compared to the measured pH. All bioreactor samples (R2-R6) contained high levels of dissolved sulfide while the limestone only reactor (R1) had no detectable sulfide.

4.2.2 pH Dependent Aluminum Removal

Aluminum can be described as a redox insensitive element that exhibits mobility in solutions of extreme pH (Bigham & Nordstrom, 2000). Figure 42 plots dissolved aluminum concentrations versus pH from AMD influent and reactors R1-R6. Minor increases in pH resulted in significant decreases of aluminum concentrations, as a pH increase to 4.0 corresponded to over 50 mol% Al removal from influent AMD. Further neutralization caused nearly 100 mol% aluminum removal in the majority of samples as pH rose above 5.0 units. The

mobility of aluminum is not particularly persuaded by changes in redox conditions and is demonstrated by the strong correlation with pH exhibited throughout the samples.

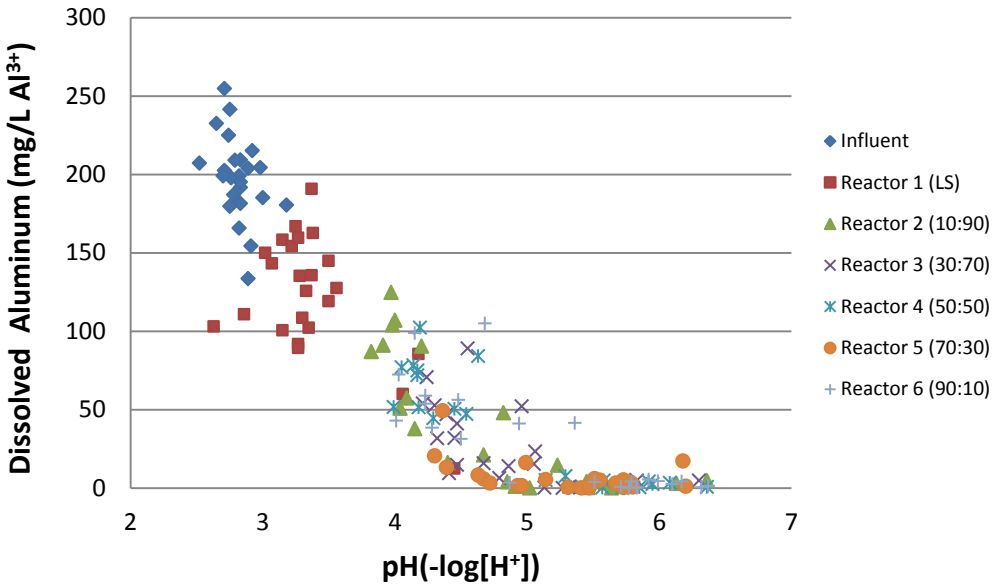

Figure 42 Plot of the dissolved aluminum concentration (mg/L Al^{3+}) against the corresponding pH measured during each sampling event.

4.2.3. Iron Oxyhydroxide Adsorption/Co-precipitation and Sulfide Formation

Sulfate removal can be achieved via surface absorption, mineral co-precipitation and microbial mediated reduction followed by hydrogen sulfide production and subsequent sulfide precipitation (Bigham & Nordstrom, 2000a; Guo & Blowes, 2009; Rose & Ghazi, 1997). To understand sulfate cycling within the reactors it is practical to first determine the major sulfate species that existed throughout the course of the experiment. Sulfuric acid is a relatively strong diprotic acid and remains in solution as bisulfate (HSO_4^-) at pH less than 2.0 units. An increase in pH above 2.0 units causes the majority of sulfate species to become fully deprotonated to divalent anionic SO_4^{2-} species. Figure 43 displays speciation of sulfuric acid along with the

minimum and maximum effluent pH values recorded within the limestone only reactor R1 (i.e. blue rectangle) and biologic reactors (pink rectangle). Throughout the entire experiment, all reactors contained the fully deprotonated SO_4^{2-} as the dominant species and thus can be used as a proxy to described sulfur cycling.

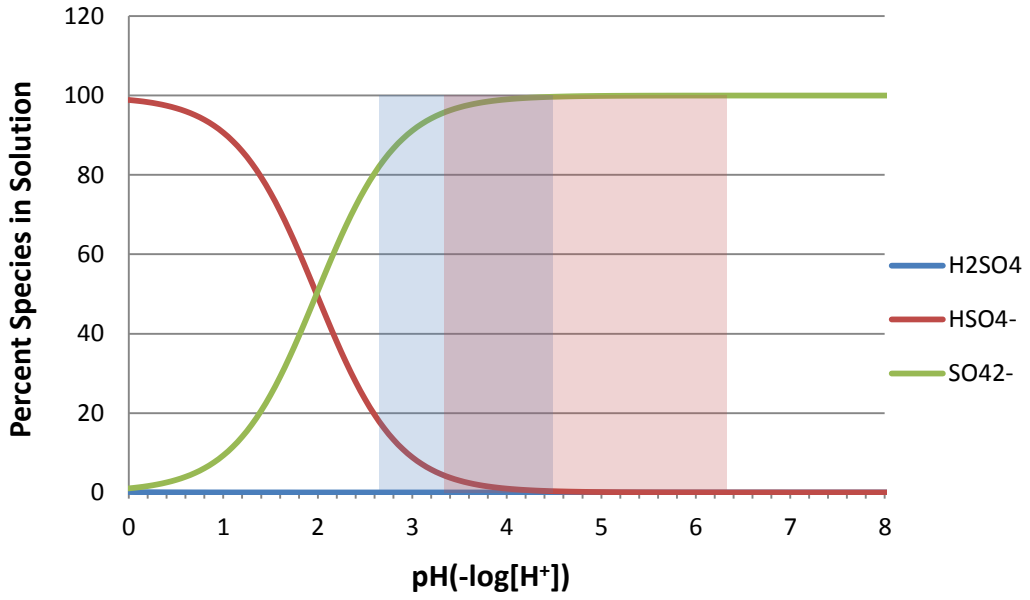

Figure 43: Speciation diagram for sulfuric acid displaying the percent of sulfate species (i.e. H_2SO_4, HSO_4^- and SO_4^{2-}) as a function of pH. Free proton concentrations measured in the limestone only reactor (R1) and biologic reactors (R2-R6) are represented by the blue and pink rectangle, respectively.

It is expected that significant changes in dissolved iron would also influence sulfate concentrations as both ions exist as abundant constituents within the influent AMD. The percent iron removal and sulfate removal in these experiments are positively correlated (Figure 44). By comparing removal percentages between the biologic reactors (R2-R6) and the limestone only reactor (R1), it can be stated that on average the bioreactors displayed higher sulfate removal as a function of iron removal, suggesting that additional sulfate-sequestration processes operated in the bioreactors.

Geochemical modeling of effluent datasets of reactor R1 (LS) describes the solution as being saturated (SI > 0) with respect to K-jarosite ($KFe^{3+}_3(OH)_6(SO_4)_2$), nano-crystalline $Fe(OH)_3$, Cu/Zn-Ferrite ($Zn_{1-x}Cu_xFe_2O_4$) and Goethite (FeO(OH)). On average a 0.22mg/L K^+ removal was documented in reactor R1 through the course of this experiment although it was sporadic and displayed many fluctuations including net potassium releases when compared to influent AMD. This suggests that K-jarosite may very well be a sulfate mineral phase that is being formed within reactor R1, yet the stability of this phase may be compromised as it ages causing a structural rearrangement to a more stable iron oxide phases, such as goethite (FeO(OH)) (Jolivet et al., 2004).

Nano crystalline ferrihydrite $Fe(OH)_3$ was supersaturated in the effluent of reactor R1 and its formation involves the hydrolysis of ferric iron (Zhu et al., 2012). Ferrihydrite precipitation would explain the low pH recorded at the upper most portion of the reactor considering that ferric iron hydrolysis involves the net release of protons (Bigham & Nordstrom, 2000). Hydroxyl groups (-OH) of nano-crystalline ferrihydrite particles would provide tremendous surface area for hydrogen bonding to occur with negatively charged SO_4^{2-} species giving rise to sulfate removal via adsorption on nano-crystalline ferrihydrite. However, ferrihydrite nano-particles may also exhibit meta-stability, as growth of nucleation sites induce phase transformations to more stable phases such as goethite. Thus, ferrihydrite may not account for the majority sulfate removal documented in the limestone only reactor (R1) (Zhu et al., 2012).

The effluent of reactor R1 was also supersaturated with respect to zinc and copper ferrite, and these phases may have formed and contributed to the removal of sulfate to varying degrees throughout the experiment. Multiple oxo (Fe-O-Fe) bridges would be available on the surfaces of

Zn/Cu-ferrite phases in which the four unbounded valence electrons of oxygen would attract protons in such low pH solutions giving the surface and overall net positive charge. In this case, sulfate ions would also exhibit adsorption to these surfaces by electrostatic interactions. Lastly, the effluent of reactor R1 was modeled as being saturated with respect to goethite (FeO(OH)) which, under these conditions, is a thermodynamically stable iron oxide phase that contains high surface area (Rietra et al., 1999). Having such high stability makes it likely that the metastable phases would have transformed via structural rearrangements or dissolution-recrystallization mechanisms resulting in the formation of goethite (Jolivet et al., 2004). The oxo (Fe-O-Fe) and hydroxyl (-OH) groups of this phase would offer sites for sulfate adsorption at the low pH measured in reactor R1, contributing to the sulfate sequestration as adsorbed species on goethite (Rietra et al., 1999; Zhang & Sparks, 1990).

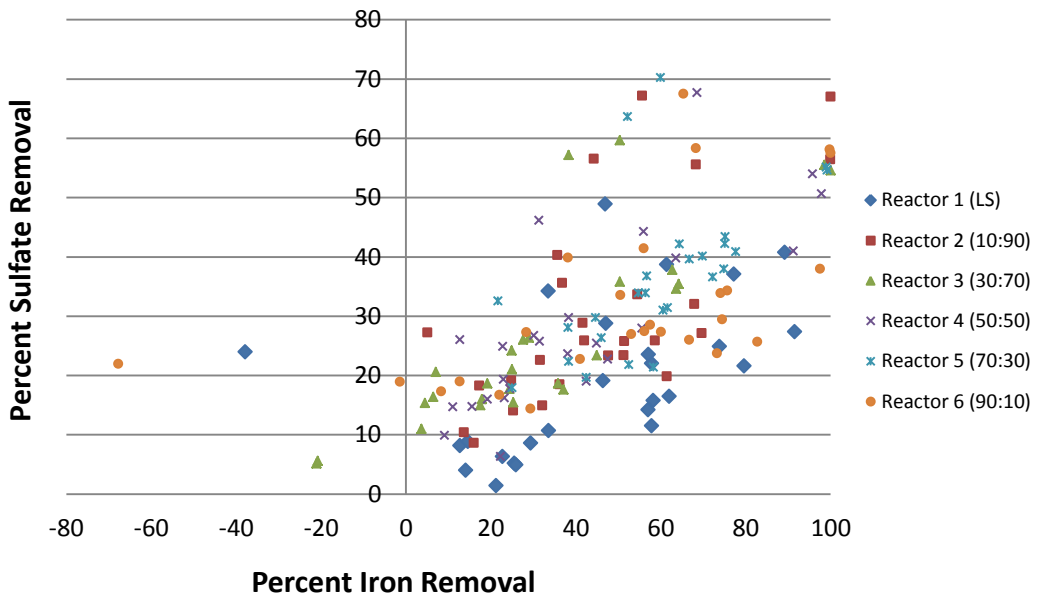

Figure 44: Percent sulfate removal versus percent iron removal with sulfate (y-axis) and iron (x-axis) removal percentages from influent AMD within each reactor (R1-R6).

Sulfide formation within bioreactors (R2-R6) is often discernible by the appearance of black precipitates in the effluent, which can be readily separated from solution through vacuum filtration (Benner et al., 1999). Effluent samples collected from bioreactors showed the presence of black to grey precipitates, while the influent and limestone only reactor (R1) always contained clear to yellow-orange solutions (Figure 45). Dissolved sulfide concentrations measured during the experiment were associated with negative ORP values as depicted in Figure 46. In order to distinguish sulfide minerals that were liable to form throughout these experiments, raw ORP values were converted to Eh units and Pourbaix diagrams were created for multiple aqueous systems.

Nordstrom et al. 2005 recognized that the standard half-cell potential of the Ag:AgCl electrode (i.e. HI769828-1) in 3.5M KCl reference solution, as used in this experiment, must be corrected for temperature induced fluctuations in reference potential. Therefore, to obtain Eh from ORP values measured in the field a linear equation was derived from variations in reference potential (E_{ref}) as a function of temperature (Figure 47). Next, the temperature dependent reference potential was corrected for each sample using measured field temperatures generating a reference potential (E_{ref}) for each data point. Electromotive force (*emf*) values determined in the field (i.e. ORP) were then added to their corresponding reference potential (E_{ref}) to determine the sample redox potential in Eh (Volts) units as outlined in the following equation (Nordstrom & Wilde, 2005):

$$Eh = emf + E_{ref} \quad (13)$$

Using calculated Eh and measured pH values, sulfide mineral formation could be further investigated by representing system parameters with Pourbaix (i.e. Eh-pH) diagrams.

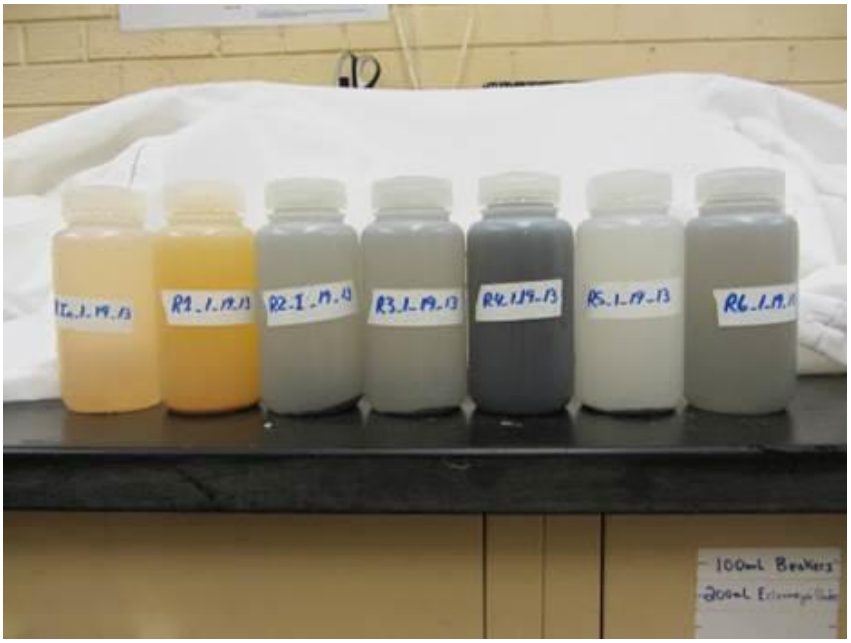

Figure 45: Photograph of samples within 1 hour of collection from left to right samples contain influent AMD, limestone only (R1) and bioreactor effluent (R2-R6).

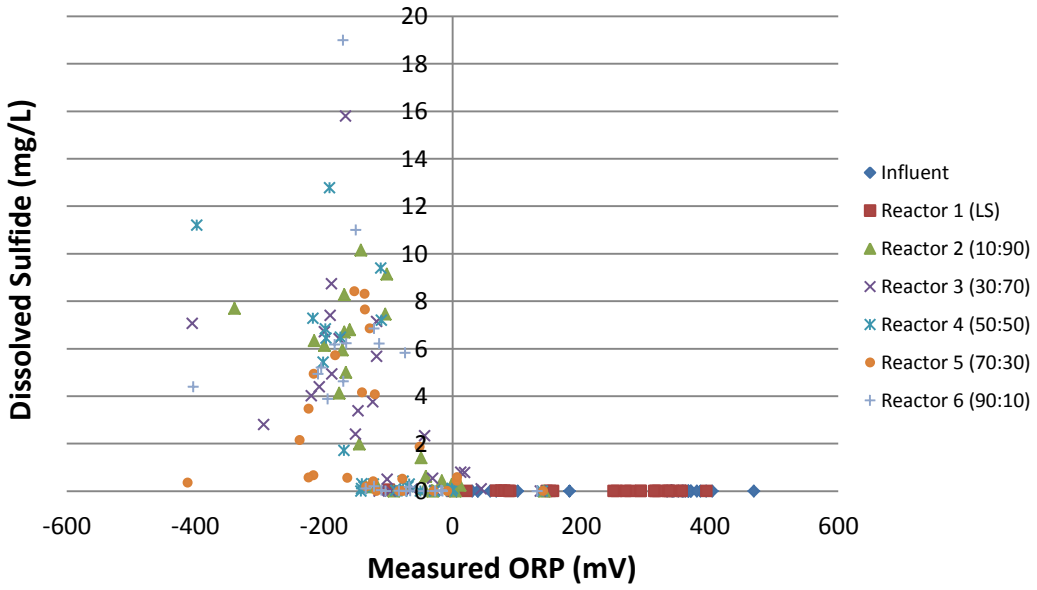

Figure 46 Measured sulfide concentrations (mg/L S^{2-}) versus the corresponding ORP (mV) values recorded in the field.

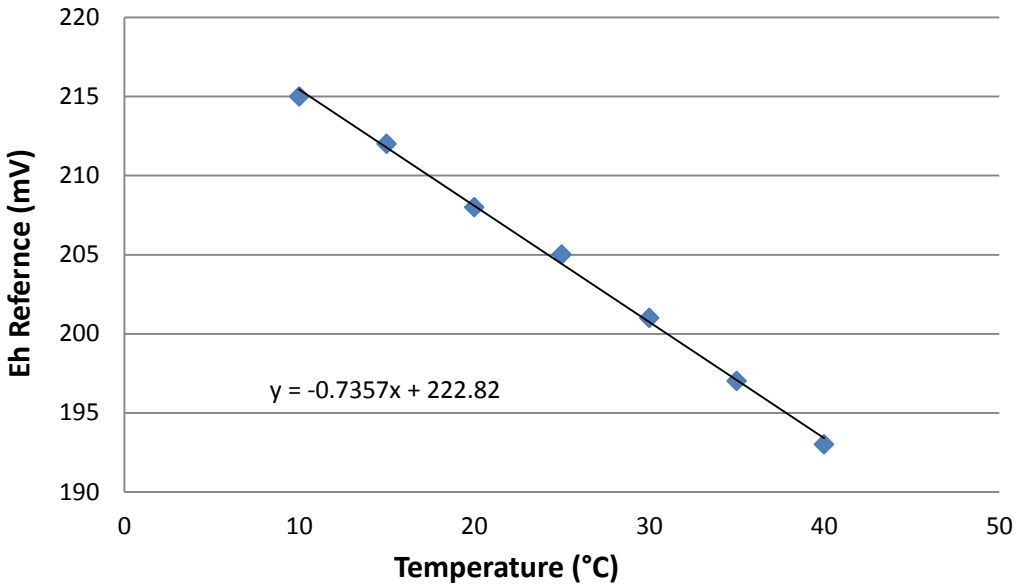

Figure 47: Standard half-cell potential of Ag:AgCl reference electrode in 3.5M KCl reference solution as a function of temperature producing a linear regression of the temperature dependent Ag:AgCl reference values determined by Nordstrom and Wilde, 2005. The linear equation was used to correct measured ORP values to field temperatures.

To define boundaries in each Pourbaix diagram, average species activities in AMD influent were used due to the relatively high ionic strength ($I_{average}$ = 0.0944) of these solutions. Two plots were formulated for each system discussed in which one represents values taken from the acid impoundment (AI) while the other characterizes effluent solutions collected from each reactor.

4.2.3.1. Fe-SO_4-H_2O system

For the Fe-SO_4-H_2O system, reactor acid impoundments displayed a few values nearing pyrite formation but the bulk of the measurements suggested solvated ferrous and ferric iron as the dominant species (Figure 48). These results coincide with previous discussions on redox and pH transitions within the acid impoundments of the bioreactors (R2-R6), as they became more oxidizing and acidic with time. Additionally, overtime the AI's of each reactor became

dominated by members of the genera *Acidimicrobiaceae*, *Alicyclobacillaceae* and *Acerobacteraceae* which all contain iron oxidizing members that may have facilitated the oxidation of ferrous iron as documented by the increase in Eh (Emerson et al., 2010; Pugh, 2013).

In contrast, Eh-pH measurements of effluent fluids suggested pyrite formation in multiple cases within the bioreactors (R2-R6), whereas the limestone reactor (R1) remained dominated by ferrous iron with a shift toward ferrihydrite formation (Figure 49). Still, pH increases within effluents of bioreactors also suggest iron oxyhydroxide formation as an additional phase. These results imply that strong variations in pH and redox conditions found in the bioreactors (R2-R6) may have caused additional sulfate removal through both sulfide formation and iron oxide adsorption/co-precipitation when compared to reactor R1.

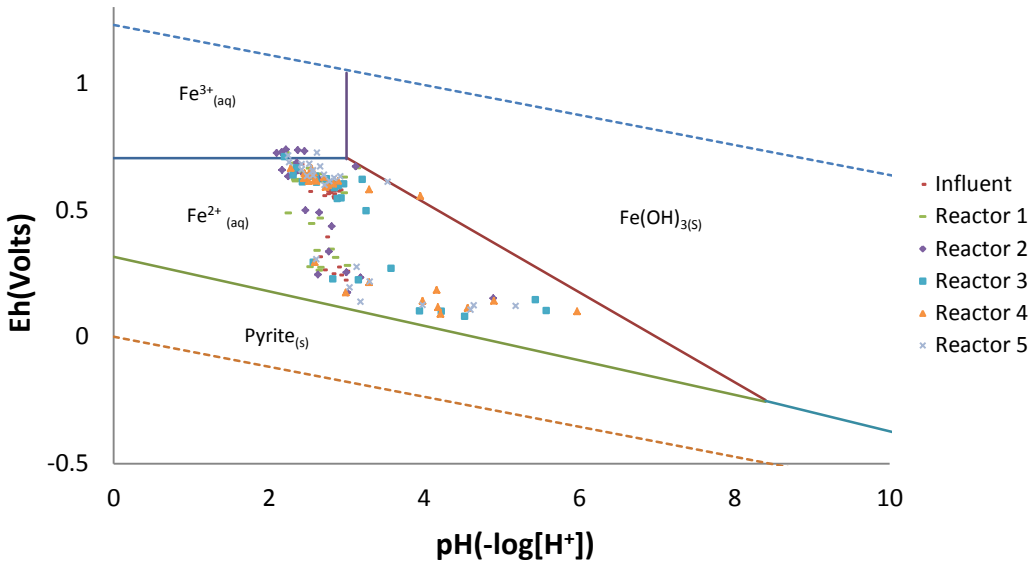

Figure 48: Pourbaix diagram of the Fe-SO_4-H_2O system and plotted Eh (y-axis) and pH (x-axis) measurements made in the AMD influent and acid impoundments of each reactor (R1-R6) during the course of the experiment. Boundary conditions: T = 25°C, P = 1.0133 bars, a[SO_4^{2-}] = $10^{-2.086}$, a[Fe^{3+}] = $10^{-4.04}$.

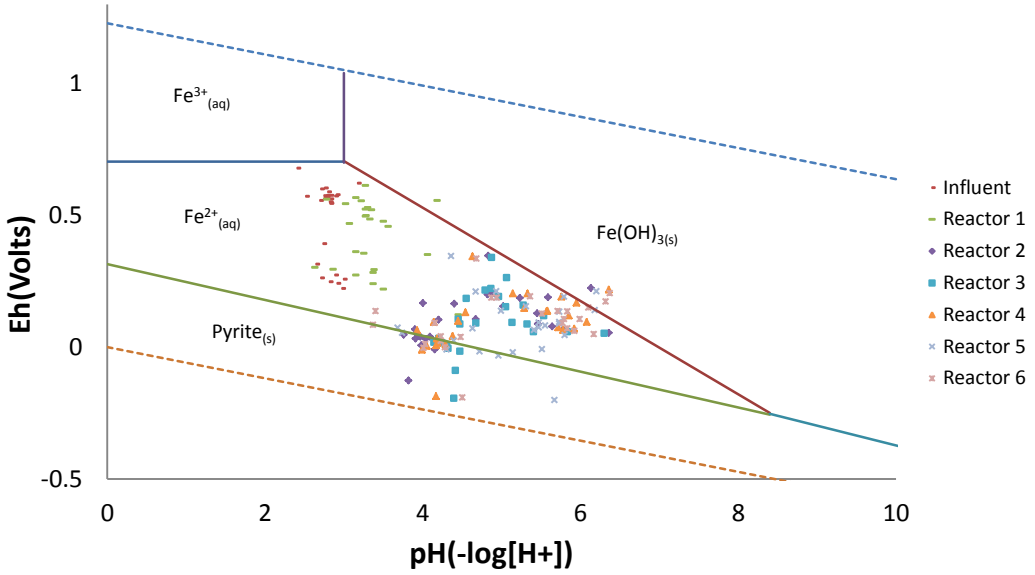

Figure 49: Pourbaix diagram of the Fe-SO_4-H_2O system and plotted Eh (y-axis) and pH (x-axis) measurements made in the AMD influent and effluents of each reactor (R1-R6) during the course of the experiment. Boundary conditions: T = 25°C, P = 1.0133 bars, a[SO_4^{2-}] = $10^{-2.086}$, a[Fe^{3+}] = $10^{-4.04}$.

4.2.3.2. Mn-SO_4-Fe-H_2O system

Dissolved manganese (Mn^{2+}) is a relatively stable species over a wide range of redox and pH values proving it a difficult element in terms of remediation (Luan et al., 2012). Manganese solubility was well represented in the data-set as an average of only 0.14% and 0.58% was removed in the limestone (R1) and bioreactors (R2-R6), respectively. Eh-pH measurements of the acid impoundments did not suggest any manganese mineralization to dominate the Mn sequestration (Figure 50). As for effluent bioreactor measurements, manganese precipitation as mono-sulfide alabandite (MnS) was expected in a few samples, which may account for the large manganese removal seen briefly during initial months (Figure 51). Recent samples (last 6 months) collected from bioreactors (R2-R6) show a decrease in the effluent pH but the conditions within the bioreactors remained reducing, causing the data to plot near Mn^{2+}-Alabandite boundary. This late shift may account for the ~6 mol% manganese removal

documented in the herbaceous bioreactors (R5, R6) during these months. Overall, the formation of manganese sulfides does not seem to play a large role in the increased sulfate removal expressed by the biologic reactors (R2-R6).

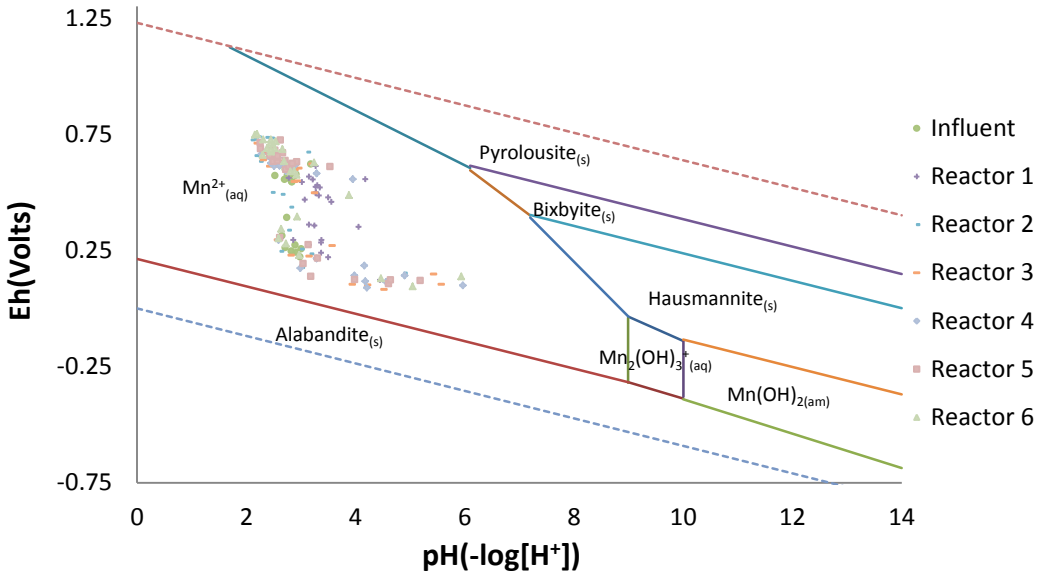

Figure 49: Pourbaix diagram of Mn-SO_4-Fe-H_2O system and plotted Eh (y-axis) versus pH (x-axis) for the AMD influent and acid impoundments of each reactor (R1-R6) collected during each sampling event. Boundary conditions: T = 25°C, P = 1.0133 bars, a[Mn^{2+}] = $10^{-3.69}$, a[SO_4^{2-}] = $10^{-2.086}$, a[Fe^{3+}] = $10^{-4.04}$.

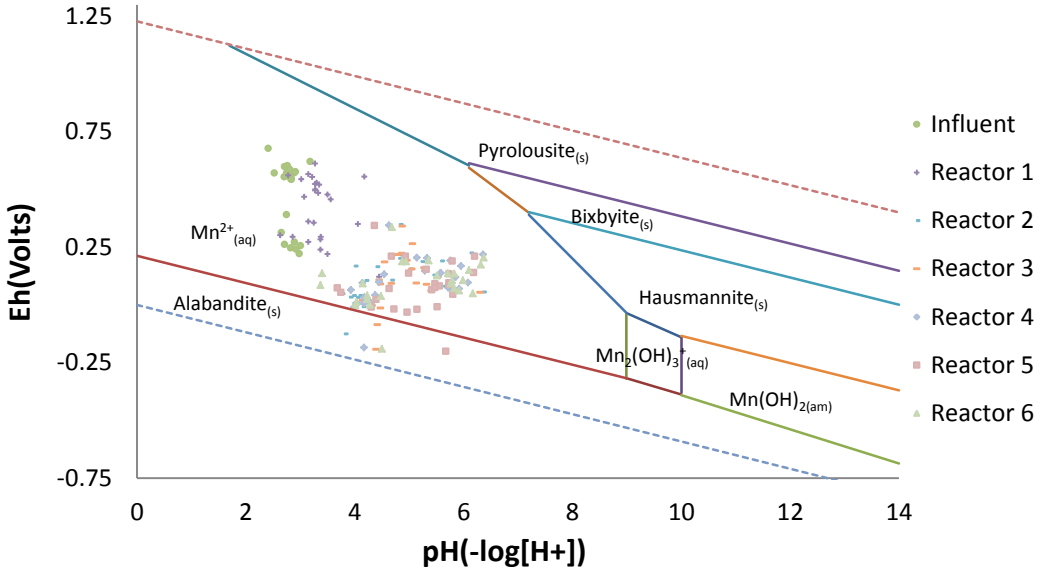

Figure 50: Pourbaix diagram of Mn-SO_4-Fe-H_2O system and plotted of Eh (y-axis) versus pH (x-axis) for the AMD influent and reactor effluents (R1-R6) collected during each sampling event. Boundary conditions: T = 25°C, P = 1.0133 bars, a[Mn^{2+}] = $10^{-3.69}$, a[SO_4^{2-}] = $10^{-2.086}$, a[Fe^{3+}] = $10^{-4.04}$.

4.2.3.3. Zn-SO_4-Fe-H_2O system

Zinc mobility in aqueous systems dominated by iron and sulfate can be extremely reduced at readily attainable pH and redox conditions (Figure 51 & 52). Formation of iron oxide precipitates in the acid impoundments of each reactor was the dominate process, as the acid impoundment water evolved to low-pH, highly oxidizing conditions. This process however, does not increase the sequestration of Zn in precipitates through the formation of Zn-intercalated ferrite as these phases are more likely to develop in solutions with pH > 3.12. In addition, aside from the early AI measurements in which the pH was high within the bioreactors (R2-R6), zinc was not expected to become incorporated into iron oxide phases in the upper portions of the bi0reactors (Figure 51). In contrast, increases in pH along with decreased redox conditions exhibited in the bioreactor (R2-R6) effluents favored formation of both Zn-Ferrite and Sphalerite (ZnS) (Figure 52). The zinc concentration measurements in the bioreactor effluents (R2-R6) indicated an average of 86.7 mol% Zn removal, suggesting that the proposed mechanisms were indeed active throughout the entire experiment. Also, microbial communities sequenced indicated the presence of SRB-species closely related to the family *Desulfobacteraceae* (Pugh, 2013) which have been demonstrated to form sphalerite in communities cultured from biofilms near Pb-Zn deposits (Labrenz, 2000). As for the limestone only reactor (R1), a minimal shift from dissolved zinc to Zn-Ferrite is observed and can explain the low Zn^{2+} removal of 5.4 mol% during the course of this experiment. The formation of zinc sulfides could also contribute to the overall decrease in sulfate in the bioreactors when compared to the limestone reactor. However, formation of Zn-Ferrite within the biologic reactors was probable and cannot be discounted as an important mechanism for zinc sequestration within ASRB technology.

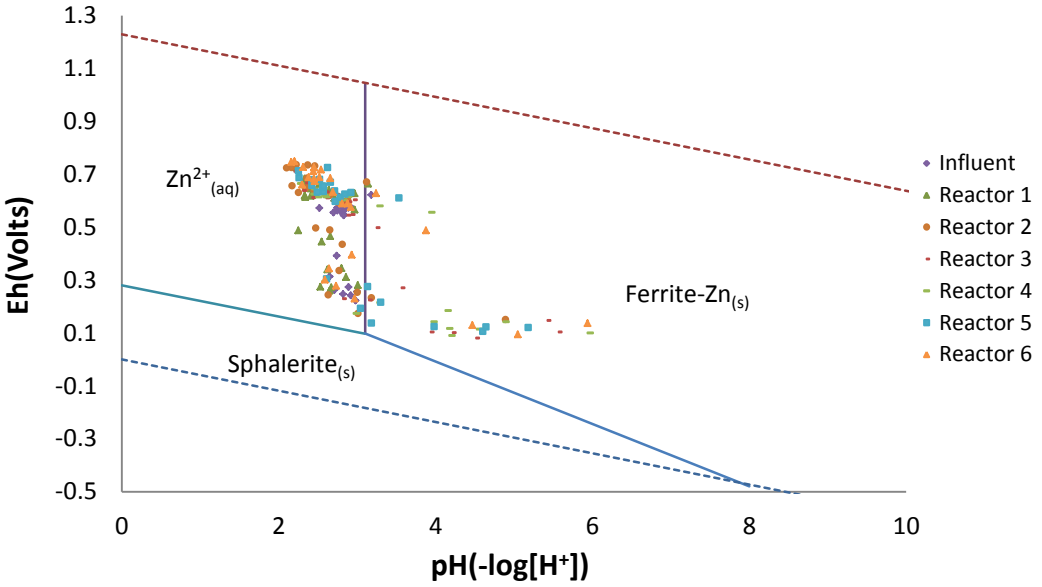

Figure 51: Pourbaix diagram for the Zn-SO_4-Fe-H_2O system and plotted Eh (y-axis) and pH (x-axis) values measured in the AMD influent and acid impoundments of each reactor (R1-R6) throughout the course of this experiment. Boundary conditions: T = 25°C, P = 1.0133 bars, a[Zn^{2+}] = $10^{-4.886}$, a[SO_4^{2-}] = $10^{-2.086}$, a[Fe^{3+}] = $10^{-4.04}$.

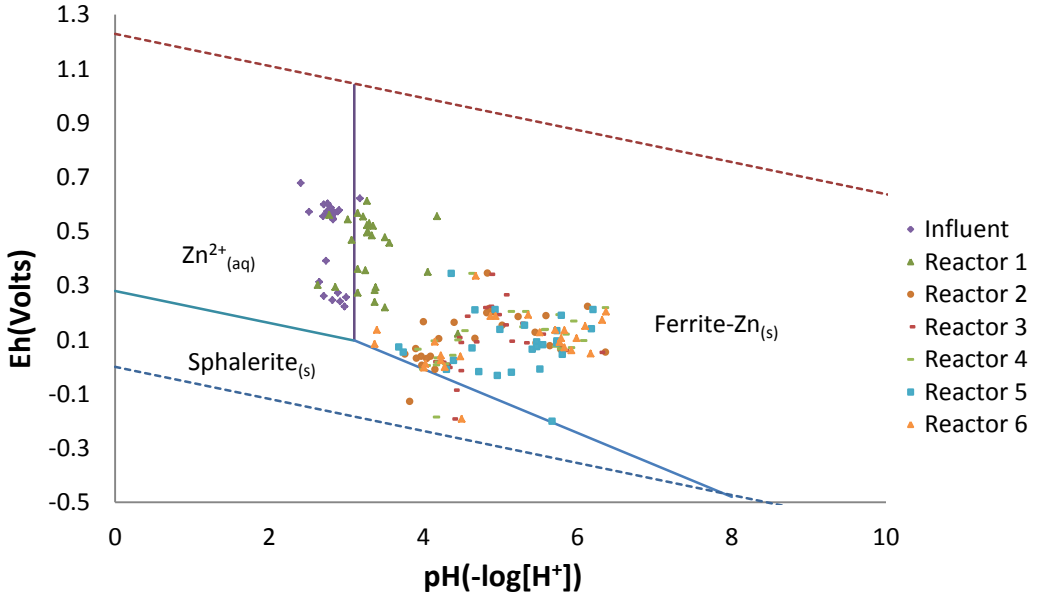

Figure 52: Pourbaix diagram for the Zn-SO_4-Fe-H_2O system and plotted Eh (y-axis) and pH (x-axis) values measured in the AMD influent and effluents of each reactor (R1-R6) throughout the course of this experiment. Boundary conditions: T = 25°C, P = 1.0133 bars, a[Zn^{2+}] = $10^{-4.886}$, a[SO_4^{2-}] = $10^{-2.086}$, a[Fe^{3+}] = $10^{-4.04}$.

4.2.3.4. Cu-Fe-SO_4-H_2O system

Within the Cu-Fe-SO_4-H_2O system, copper can be removed via intercalation into the structure of iron oxides along with formation of various sulfide phases such as chalcopyrite ($CuFeS_2$). Under the Eh-pH conditions of multiple acid impoundment samples, copper could have been mainly precipitated as $CuFeO_2$ but also Cu-Ferrite and even Chalcopyrite (Figure 53). Recent AI measurements suggest that solvated copper is more favored over mineral phase sequestration, due to increases in Eh potentials along with free proton concentrations. At depth, within the bioreactors, reducing environments and increased pH values promote the precipitation of all three phases which supports the finding of high average 81.4 mol% copper removals documented within the bioreactors (R2-R6) (Figure 54). As for reactor R1 (LS), increase in pH caused the data-set to shift away from solvated Cu^{2+} towards a solution environment that favors $CuFeO_2$ formation. On average reactor R1 removed 53.8 mol% copper from the AMD influent. The environmental conditions present in reactor R1 indicate that the main mechanism of copper sequestration was intercalation of copper within the iron oxide structure. With respect to the bioreactors (R2-R6), chalcopyrite formation could have definitely accounted for increase in sulfate removal observed over the course of this experiment.

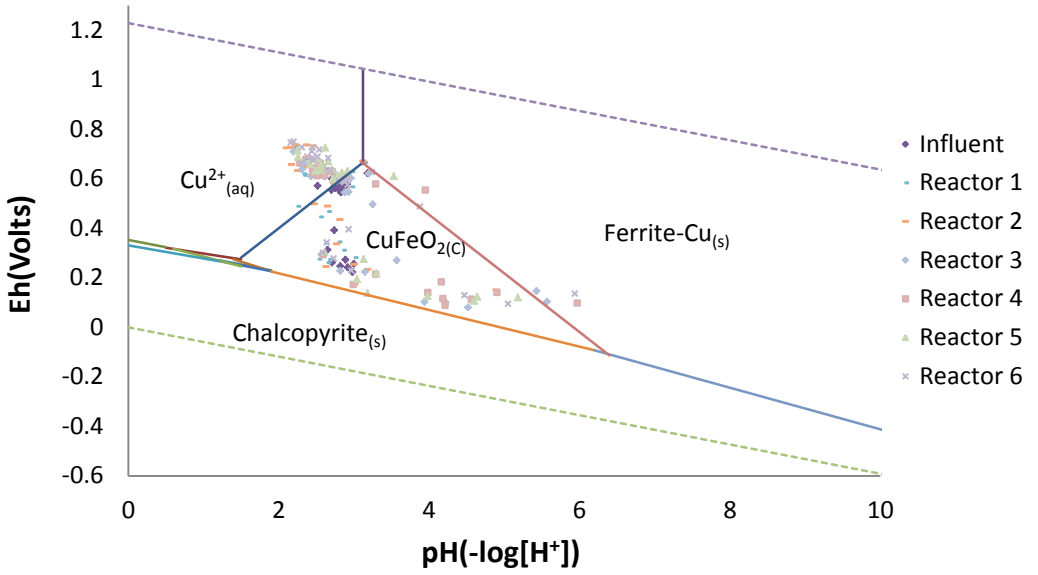

Figure 53: Pourbaix diagram of the Cu-Fe-SO_4-H_2O system and plotted Eh-pH measurements made in the AMD influent and acid impoundments of each reactor (R1-R6) during the course of the experiment. Boundary conditions: T = 25°C, P = 1.0133 bars, a[Cu^{2+}] = $10^{-6.642}$, a[SO_4^{2-}] = $10^{-2.086}$, a[Fe^{3+}] = $10^{-4.04}$.

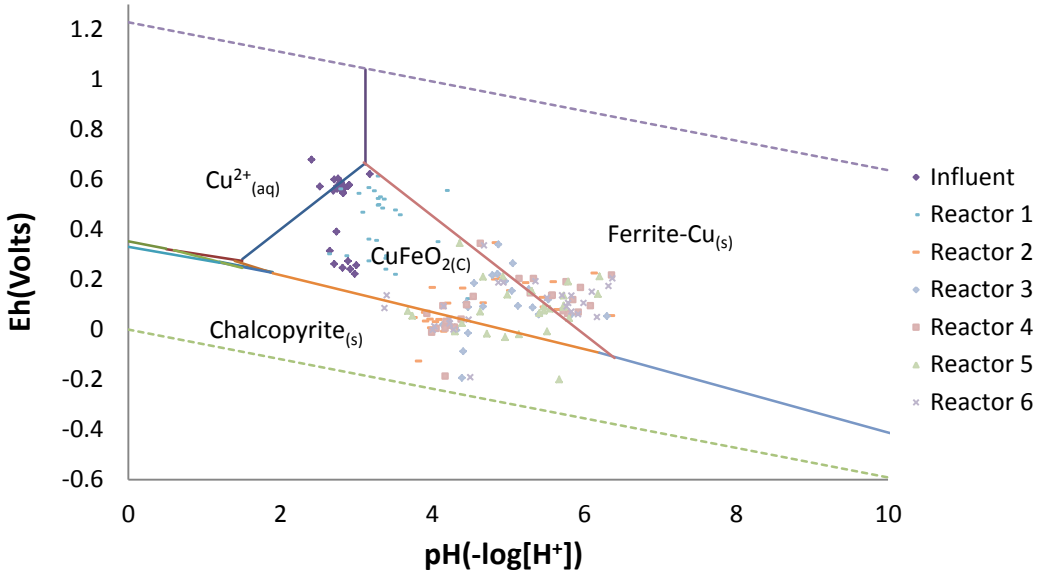

Figure 53: Pourbaix diagram of the Cu-Fe-SO_4-H_2O system and plotted Eh-pH measurements made in the AMD influent and acid impoundments of each reactor (R1-R6) during the course of the experiment. Boundary conditions: T = 25°C, P = 1.0133 bars, a[Cu^{2+}] = $10^{-6.642}$, a[SO_4^{2-}] = $10^{-2.086}$, a[Fe^{3+}] = $10^{-4.04}$.

4.2.3.5. Ni-Fe-SO_4-H_2O system

At pH values above 2.71 units, nickel tends to become rather insoluble within the Ni-Fe-SO_4-H_2O system and can precipitate under all redox conditions, within the stability limits of water. The acidity of the acid impoundments of all reactors (R1-R6) had increased with time and in many cases pH values dropped below that of influent AMD (Figure 54). In consequence, the solubility of nickel within the acid impoundments would have also increased with time, suggesting that most nickel removal occurs deeper within the reactors. Eh-pH measurements of the limestone only reactor (R1) effluent fluids shift slightly into $NiFeO_4$ stability, indicating that any nickel removal occurring in this reactor is liable to correspond to iron oxide formation (Figure 55). However, results show only minimal nickel removal from reactor R1, along with many sampling events measuring net increase in nickel concentrations. Average AMD nickel concentrations exhibit high relative deviations which is expected considering average influent pH is 2.80 units which is extremely close to the Ni^{2+}-$NiFeO_4$ boundary. Therefore, the overall nickel removal in reactor R1 may be slightly underestimated due to the high degree of variability in influent nickel concentrations. Although results have indicated possible formation of nickel sulfide phases, effluent measurements of the bioreactors (R2-R6) suggest the environment is conducive to $NiFeO_4$ precipitation. Still, multiple bioreactor samples fall near the border of the two phases, NiS_2 & $NiFeO_4$. Thus, nickel sulfides cannot be ruled out as mineral phases that contribute to the additional sulfate removal seen within the bioreactors (R2-R6).

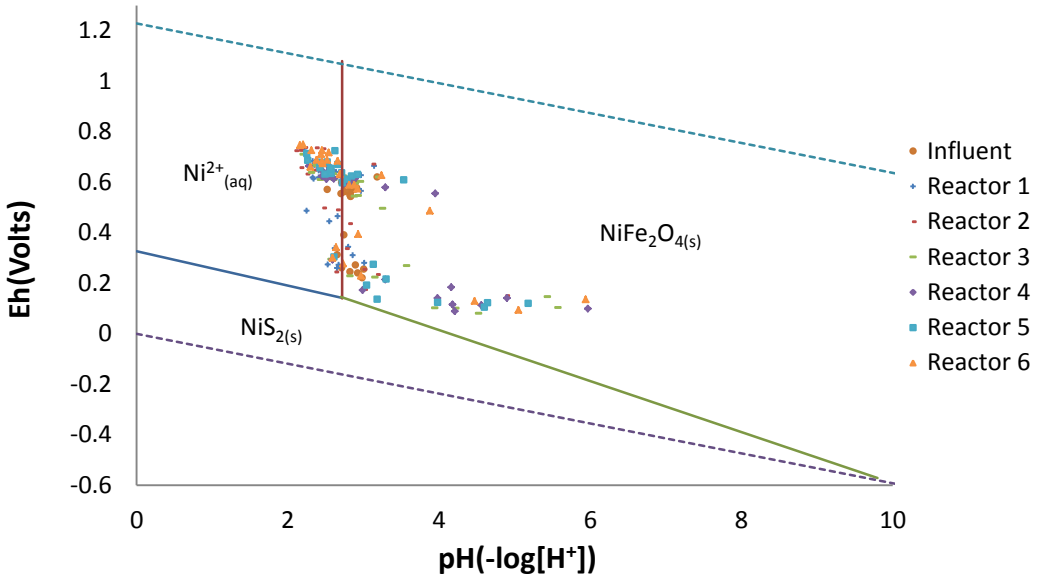

Figure 54: Pourbaix diagram for the Ni-SO_4-Fe-H_2O system with measured Eh (y-axis) and pH (x-axis) values in the AMD influent and acid impoundments of each reactor (R1-R6) throughout the course of this experiment. Boundary conditions: T = 25°C, P = 1.0133 bars, a[Ni^{2+}] = $10^{-5.018}$, a[SO_4^{2-}] = $10^{-2.086}$, a[Fe^{3+}] = $10^{-4.04}$.

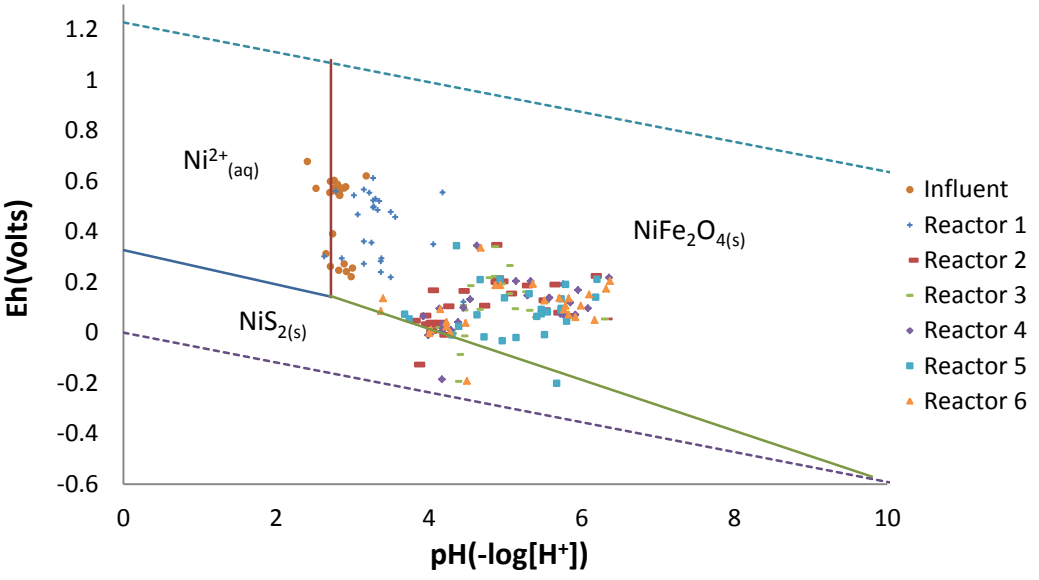

Figure 55: Pourbaix diagram for the Ni-SO_4-Fe-H_2O system with measured Eh (y-axis) and pH (x-axis) values in the AMD influent and effluents of each reactor (R1-R6) throughout the course of this experiment. Boundary conditions: T = 25°C, P = 1.0133 bars, a[Ni^{2+}] = $10^{-5.018}$, a[SO_4^{2-}] = $10^{-2.086}$, a[Fe^{3+}] = $10^{-4.04}$.

4.2.3.6. Trace Metal Removal

To further discern whether trace metals are sequestered through iron oxide adsorption/co-precipitation or sulfide formation within the bioreactors (R2-R6), it is practical to compare the trace metal removal and sulfide concentrations in effluent samples. Figures 56 and 57 depict the measured sulfide concentrations against the nickel and zinc removal percentages, respectively. High nickel and zinc removal was observed in bioreactor samples containing dissolved sulfide values that ranged from 0-10 mg/L S^{2-}. This result suggests that trace metals were removed by both iron oxide intercalation and sulfide phase formation within the bioreactors. Since both mechanisms (i.e. FeO-intercalation & sulfide formation) for trace metal removal were possible, the high removal percentages of these species relative to reactor R1 are expected. Also, the limestone reactor (R1) did not produce sulfide levels of any significance and displayed low nickel and zinc removal, indicating that maintaining pH levels greater than average effluent values of R1 (i.e. pH > 3.34) is important in removing zinc and nickel via iron oxyhydroxide adsorption/co-precipitation.

Additionally, high zinc removal was expressed throughout a wide range of nickel removal percentages (i.e. 50-100 mol%) although the Pourbaix diagram for the Ni-Fe-SO_4-H_2O system describes nickel precipitation over a slightly broader range of pH-Eh conditions (Figure 58). Hallberg et al. (2011) have shown that nickel laterites are extremely susceptible to reductive dissolution by subjecting them to reducing environments produced by cultures of *Acidithiobacillus ferrooxidans*. Consequently, nickel phases may be more susceptible to reductive-oxidative dissolution processes when subjected to the high variation in redox gradients observed within the bioreactors.

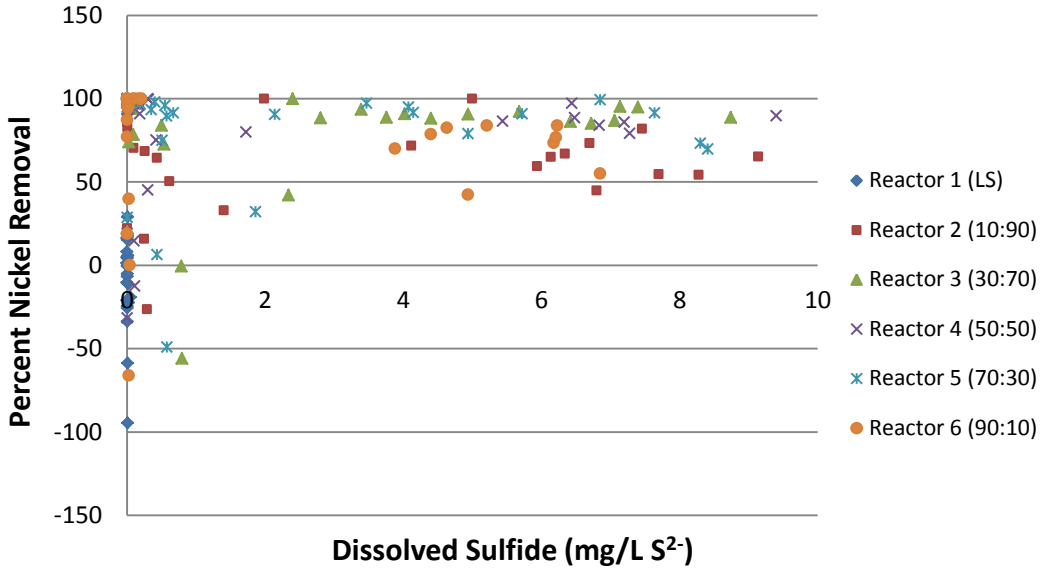

Figure 56: Percent nickel removal vs. dissolved sulfide. Plot displaying the percent nickel removal from influent AMD within all reactors (R1-R6) against dissolved sulfide concentrations measured (mg/L S^{2-}).

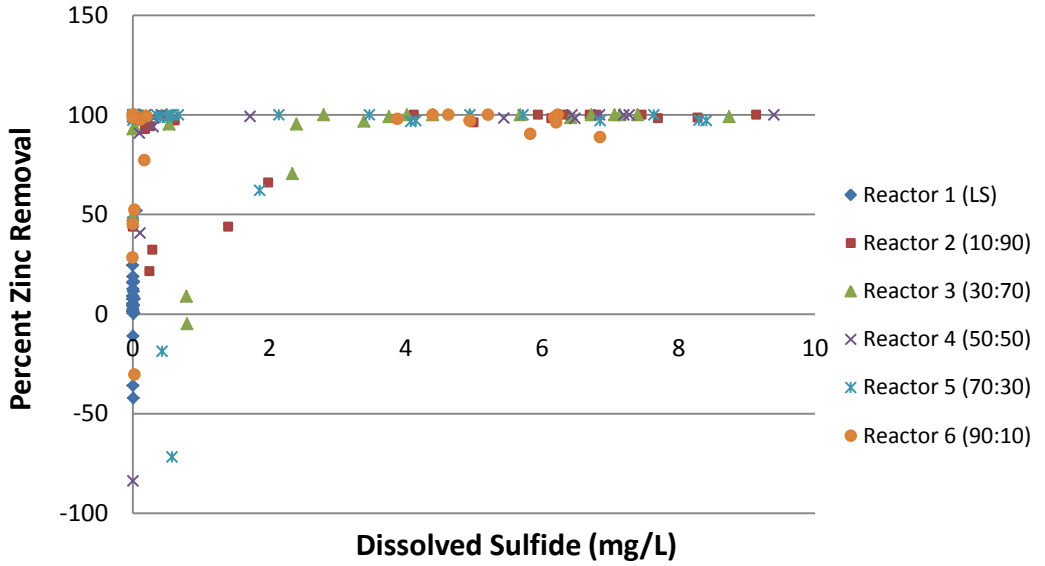

Figure 57: Percent zinc removal vs. dissolved sulfide. Plot displaying the percent zinc removal from influent AMD within all reactors (R1-R6) against dissolved sulfide concentrations (mg/L S^{2-}).

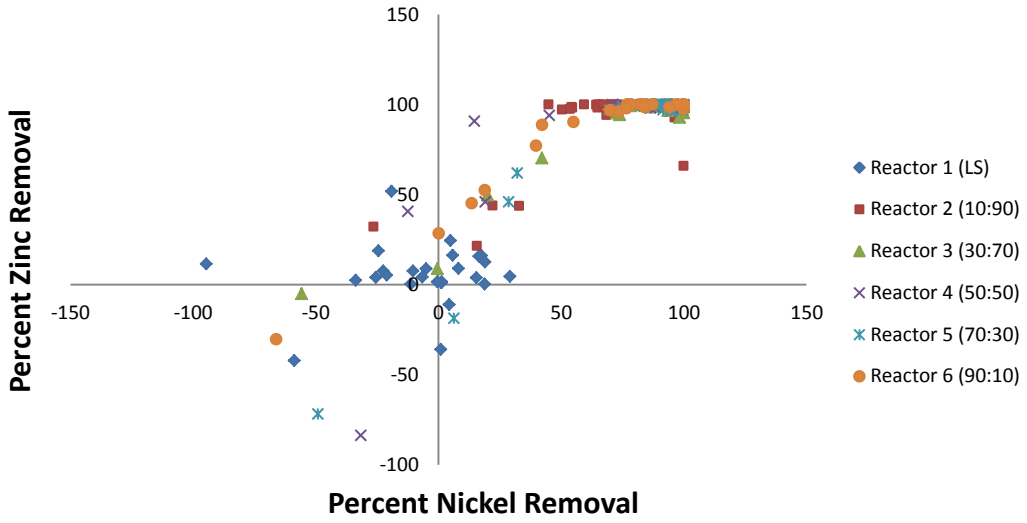

Figure 58: Plot displaying the percent zinc (y-axis) and nickel (x-axis) removal from the influent AMD to the effluent of each reactor (R1-R6) during the course of this experiment.

4.2.4. Hydrogen Sulfide ($H_2S_{(g)}$) Volatilization

Reduction of sulfate and subsequent formation of sulfide phases within all bioreactors (R2-R6) has been identified as a mechanism to achieve increased sulfate removal when compared to the limestone only reactor (R1). Still, it is apparent that trace metal removal in the bioreactors (R2-R6) could have been increased by the formation of intercalated iron oxide phases. Consequently, the high sulfate removal may not be completely accounted for by sulfide precipitation alone.

As a final mechanism, sulfide removal via partitioning of aqueous hydrogen sulfide $H_2S_{(aq)}$ into the gaseous phase $H_2S_{(g)}$ may offer an additional pathway for enhance sulfate removal within the bioreactors (R2-R6). Hydrogen sulfide is a weak acid (pK_{a1} = 7.02) and, therefore, in an open system under acidic conditions (pH < 7) it has great potential to escape solvation in its di-protonated gaseous phase. An anaerobic bioreactor column experiment ran by Bernandez et al. (2012) displayed no evidence of $H_2S_{(g)}$ volatilization yet detected high concentrations of dissolved. However, the pH measured during their experiment was consistently

reported above the pKa_1 of $H_2S_{(aq)}$ (i.e. pH ~ 7.5), which favors this constituent in the monoprotic form (i.e. HS^-). Therefore, throughout this experiment, the low effluent pH values documented in the bioreactors (pH < 6.3) would promote $H_2S_{(aq)}$ formation. As a result, conversion of $H_2S_{(aq)}$ into $H_2S_{(g)}$ within in the bioreactors and subsequent exsolvation may account for the additional sulfate removal.

4.2.5. Sulfur Isotopes as Indication of Bacterial Mediated Sulfate Reduction

Sulfur isotopes have been successfully used to detect and monitor biologically-mediated sulfate reducing processes in natural environments. Since microbial growth preferentially removes isotopically light elements from the system, it is expected that heavier sulfur isotope values measured in dissolved sulfate from bioreactor effluent correlate with bacterial sulfate reducing processes (Burns et al., 2012; Guo & Blowes, 2009; Walters et al., 2013). This is due to the light sulfur isotopes being incorporated in biologically produced hydrogen sulfide and the corresponding sulfide mineral phases. To evaluate the extent of biological sulfate reducing processes, the difference in sulfur isotope composition between the bioreactor effluents (R2-R6) and the influent AMD was considered.

Sulfur isotope measurements of dissolved sulfate were performed on samples collected from the influent AMD and effluent fluids of each bioreactor (R1-R6). Enrichment ($\varepsilon^{34}S_{In\rightarrow Eff}$) factors were determined by subtracting the AMD influent isotope composition ($\delta^{34}S_{IN}$) from each reactor's (R1-R6) effluent isotope composition ($\delta^{34}S_{EFF}$) via the following equation:

$$\varepsilon^{34}\delta S_{In\rightarrow Eff} = \delta^{34}S_{EFF} - \delta^{34}S_{IN} \quad (14)$$

Therefore, a negative enrichment factor corresponds to effluent dissolved sulfate that is ^{34}S-depleted with respect to influent AMD while positive enrichment factors are associated with

effluent dissolved sulfate that is ^{34}S-enriched with respect to influent AMD. Figure 59 displays calculated enrichment factors throughout the course of the experiment. During the experiments, increasing bacterial-mediated sulfate reduction processes are associated with enrichment of 10-15‰ (Table 2). In contrast, only minimal enrichments in sulfur isotopes of <1‰ were observed within the limestone only reactor (R1) during the course of the experiment. This dismisses any abiotic contribution (e.g. adsorption/co-precipitation) as a major component influencing such large positive enrichments in the sulfur isotope composition within bioreactor (R2-R6) effluent sulfate. Furthermore, the variation in magnitude of sulfur isotope enrichment mirrors the variation in dissolved sulfide concentrations (Figure 18) measured within the biologic reactors (R2-R6). Similar to results reported in previous studies, the present study documents analogous responses in the isotopic composition trends of the effluent sulfate within bioreactor samples (R2-R6) during dates in which high sulfide concentrations were measured. However, during low-temperature months (T < 10° C), decreases in positive enrichment factors were documented (Figure 59). In early February 2013, a negative enrichment factor value of -1‰ was observed in reactor R6 (90:10), that can be associated with the oxidative dissolution of previously formed ^{34}S-depleted sulfide mineral phases. As average temperatures began to rise above 10°C, positive enrichment factor values was recorded in all bioreactors (R2-R6), yet never reached enrichment values as high as those that were documented during the initial biologically active months (October-December, 2012).

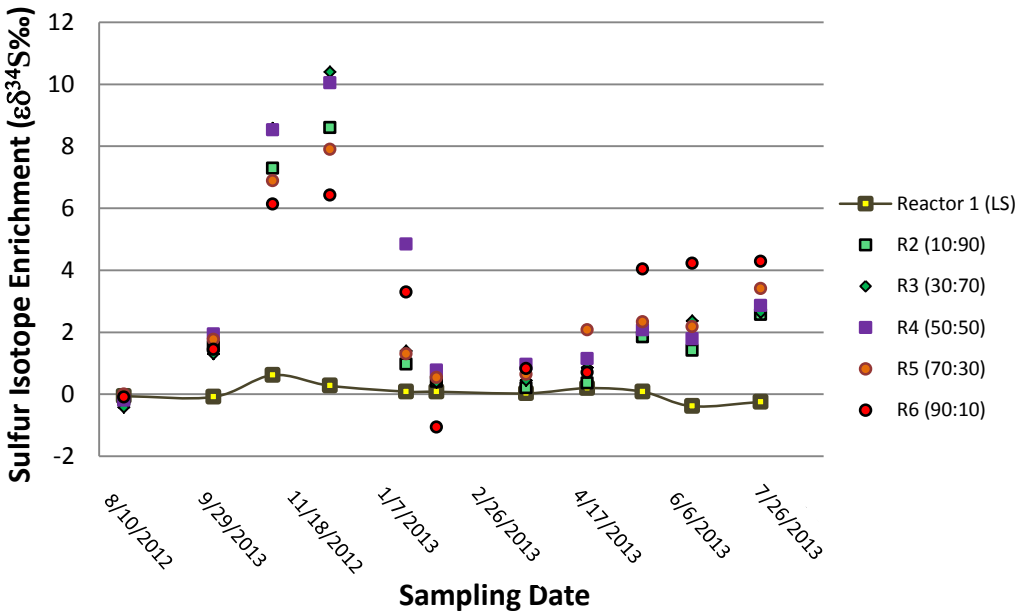

Figure 59: Calculated $\delta^{34}S$ enrichment/depletion ($\varepsilon^{34}S_{In \rightarrow Eff}$ (‰)) by comparing the sulfur isotope composition of the dissolved sulfate precipitated from the influent AMD and the effluent solutions collected during each sampling event.

Transitions in microbial mediated sulfate reduction and their relation to the overall percent sulfate removal are outlined in figure 60. Within the initial months (Aug-Oct, 2012) of operation, $\varepsilon^{34}S$ exhibited low values (0 - 4‰) while sulfate removal ranged from 27-70% removal. These results indicate that SRB communities were not yet fully established making abiotic mechanisms (i.e. adsorption/co-precipitation), the dominant pathway for sulfate removal. During the following months (Oct-Dec, 2012) of operation, $\varepsilon^{34}S$ increased (6 - 12‰) and sulfate removal within the biologic reactors (R2-R6) fell between 50-67 mol%. This implies that SRB communities had become well established and biologically-mediated sulfate removal was the dominant mechanisms for sulfate sequestration. Subsequent months (Jan-March, 2013) of operation corresponded to lower values $\varepsilon^{34}S$ (-1 - +2‰) and sulfate removal within the biologic reactors (R2-R6) fell between 5-40 mol% suggesting that biological reduction decreased and

abiotic processes governed sulfate removal. In the final months of which the sulfur isotope composition of the effluent sulfate was measured (March-July, 2013), an increase in $\varepsilon^{34}S$ factor documented values up to +4.5‰. This corresponded to increase in both sulfide concentrations (Figures 17 & 18) and sulfate removal within the biologic reactors (R2-R6). Overall changes in the sulfur isotope enrichment factor in all reactors (R1-R6) have shown time-dependent transitions in the biologically mediated sulfate reduction.

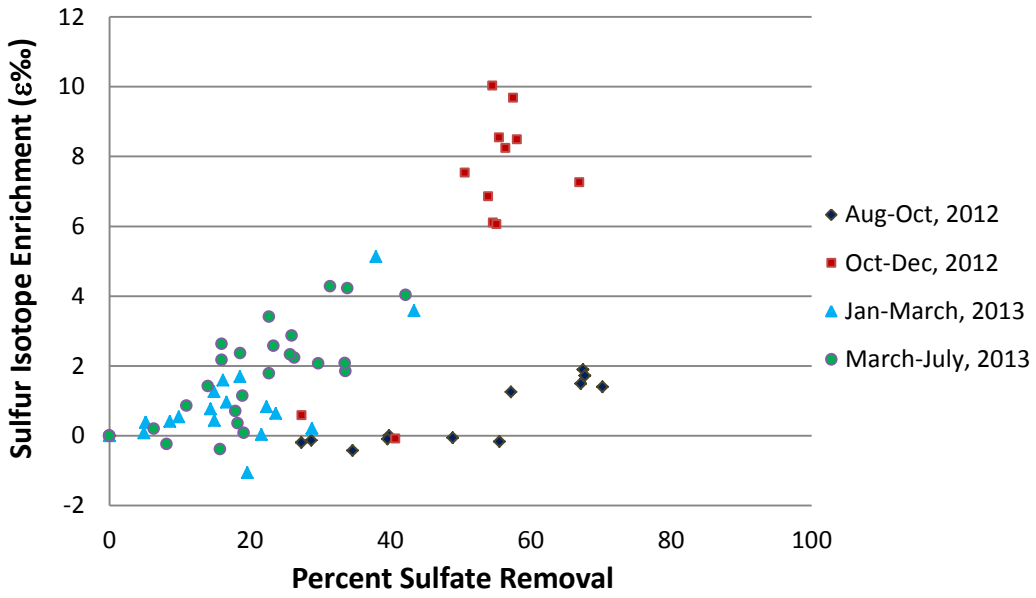

Figure 60: Measured sulfate removal percentages (x-axis) and the corresponding sulfur isotope enrichment factor (y-axis) of the dissolved sulfate precipitated from each sample through the course of this experiment. Data points are group by as Aug-Oct, 2012(Black Diamond); Oct-Dec, 2012(Red Square); Jan-March, 2013(Blue Triangle) and March-July, 2013(Green Circle) to show time dependent transitions.

4.3. Reactor Performance based on Substrate Composition

To constrain whether substrate variations induced measureable differences in remediation efficacy, experimental results from all reactors (R1-R6) were group in the following four categories:

1) Limestone Only Reactor (R1)
2) Dominantly Ligneous Reactors (R2, R3)
3) 50/50: Ligneous/Herbaceous Mixture (R4)
4) Dominantly Herbaceous Reactors (R5, R6)

Each chemical species present in the AMD influent was compared to the effluent concentrations in each reactor to determine removal percentages based on reactor type via the flowing equation:

$$(([X]_{AMD} - [X]_{Reactor})/[X]_{AMD})*100 = \% [X] \text{ Removal} \quad (15)$$

Where $[X]_{AMD}$ and $[X]_{Reactor}$ represents the concentration of any particular species (i.e. SO_4, Fe, Al, Mn) in the influent AMD and the effluent of each reactor, respectively. During each sampling event, the percent removal of sulfate, iron, aluminum and manganese was calculated for each reactor (R1-R6). Values obtained were then averaged by reactor type and compared to discern whether reactor composition has an effect on remediation efficacy (Figure 61-64).

Increased sulfate removal was achieved within in the bioreactors (i.e. 28-31 mol%) when compared to the limestone only (i.e. 19 mol%) reactor (R1). This could be attributed to sulfate reduction and formation of sulfides within the bioreactors (R2-R6) which was not documented in the limestone only reactor (R1). Comparison of sulfate removal efficiency among the bioreactors demonstrates increased removal as herbaceous content of the reactor increases (Figure 61). Therefore, during the time-span of this experiment herbaceous substrate is identified as the optimal substrate to enhance sulfate removal in ASRB technology.

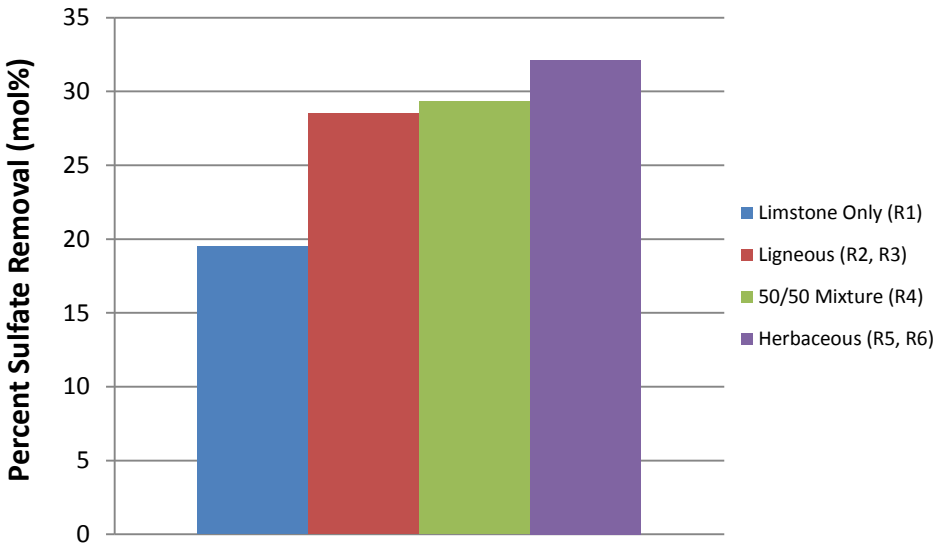

Figure 61: Overall percent sulfate removal from the influent AMD in the limestone only reactor (R1; Blue Bar), ligneous reactors (R2, R3; Red Bar), 50/50 mixture (R4; Green Bar) and herbaceous reactors (R5, R6; Purple Bar) during the course of this experiment.

Removal of iron from influent AMD was not particularly optimized within the bioreactors as the limestone only reactor (R1) displayed a higher overall removal percentage (i.e. 44.5 mol%) when compared to the ligneous (R2, R3) and 50/50 mixture (R4) bioreactors (i.e. 38.9 mol% & 42.9 mol%) (Figure 62). The redox sensitivity of the iron (oxy)hydroxide and iron sulfide phases may decrease the proficiency in iron removal within ASRB technology as these reactors displayed temporal fluctuations in redox gradients. However, between all reactors (R1-R6), there is a direct correlation between the herbaceous content and the iron removal efficiency of each reactors, with the dominantly herbaceous reactors (R5, R6) achieving the highest iron removal percentage of 55 mol%. As a result, in terms of ASRB technology, this study identifies that increased iron removal can be accomplished by increasing the herbaceous substrate within the bioreactor.

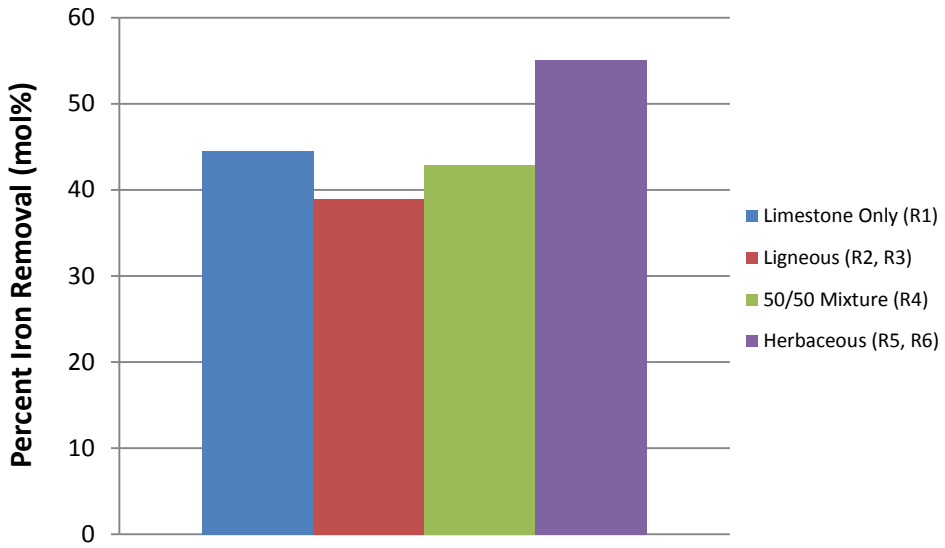

Figure 62: Overall percent iron removal from the influent AMD in the limestone only reactor (R1; Blue Bar), ligneous reactors (R2, R3; Red Bar), 50/50 mixture (R4; Green Bar) and herbaceous reactors (R5, R6; Purple Bar) during the course of this experiment.

All bioreactors (R2-R6) had documented enhanced aluminum removal (i.e. 82-91 mol%) when compared to the reactor R1 (i.e. 36.9 mol%). Since the formation of aluminum precipitates is predominantly redox insensitive, their stability was maintained as redox gradients evolved within the bioreactors. Substantial increases in pH values from the influent AMD drainage to the effluent of the bioreactors (R2-R6) optimized aluminum removal in theses reactors over reactor R1 (LS). Temporal trends in the effluent pH values of bioreactors (R2-R6) determined that the herbaceous reactors were able of maintaining higher pH values as the experiment progressed. This corresponded to higher overall aluminum removal percentages over time and indicates that increased herbaceous content in ASRB's can also aid in optimizing aluminum removal.

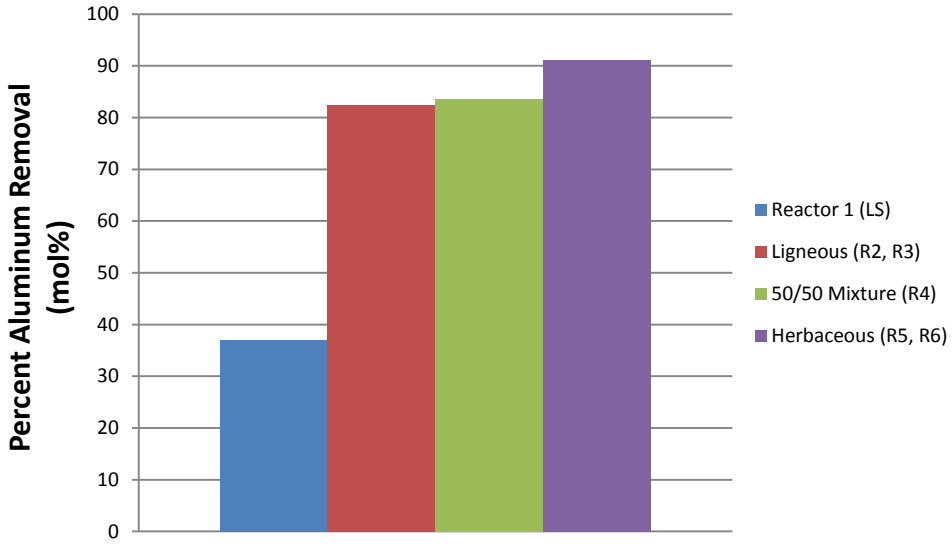

Figure 63: Overall percent aluminum removal from the influent AMD in the limestone only reactor (R1; Blue Bar), ligneous reactors (R2, R3; Red Bar), 50/50 mixture (R4; Green Bar) and herbaceous reactors (R5, R6; Purple Bar) during the course of this experiment.

Manganese removal percentages in the limestone reactor (R1) were negligible and showed similar concentrations to the influent manganese from August 2012 – October 2012 (Figure 64). In the bioreactors (R2-R6), during the initial week of the experiments, a net increase in manganese concentration was measured relative to the influent AMD drainage. Then, the concentration of manganese in the bioreactors quickly decreased and manganese removal ranging from 9-32 mol% was observed in late September 2012- early October 2012. During the following two months (November 2012 – December 2012), manganese removal became significant in the limestone reactor reaching 16 mol% average manganese removal between the two months. This removal coincides with the high iron removal (i.e. 90 mol%) also observed in the limestone reactor during these months. Still, manganese removal was even greater in the bioreactors during these months (November 2012 – December 2012) with up 59 mol% removal and an average removal of 33 mol%. As the reactors began to experience prolonged periods of

cold temperatures another release of manganese was documented through January 2013 – February 2013. During these months an average increase of 12 mol%, 19 mol%, 16 mol% and 8 mol% from influent AMD manganese was documented in the limestone reactor (R1), ligneous reactors (R2, R3), 50/50 reactor (R4) and herbaceous reactors (R5, R6), respectively. As manganese measurements continued from March 2013 to September 2013 minimal removal percentages were recorded in all reactors. However, the herbaceous reactors (R5, R6) showed the greatest Mn^{2+} retention, together averaging 6 mol% removal through the final six months.

These fluctuations show that although manganese removal can be achieved within ASRB technology it can be greatly disturbed by temporal changes in redox gradients. Overall, manganese removal was minimal documenting less than 4 mol% removal in all reactor types. Although the herbaceous reactors (R5, R6) averaged the highest manganese removal a direct correlation between increasing herbaceous content and removal was not exhibited as the ligneous reactors (R2, R3) displayed higher manganese removal than the 50/50 mixture (R4). This study suggests that increased herbaceous substrate can help enhance manganese removal using ASRB technology, yet overall removal will still be minimal.

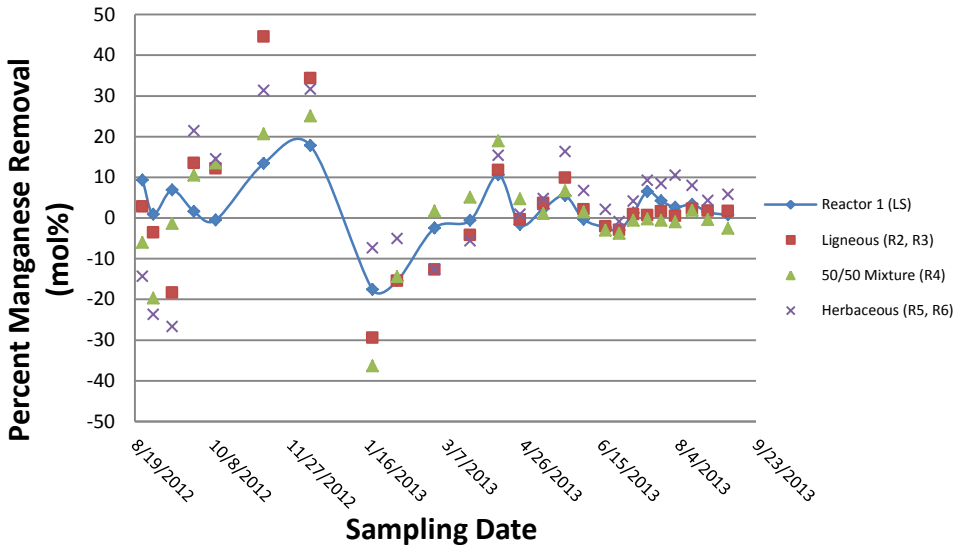

Figure 64: Percent manganese removal from the influent AMD in the limestone only reactor (R1), ligneous reactors (R2, R3), 50/50 mixture (R4) and herbaceous reactors (R5, R6) during the course of this experiment.

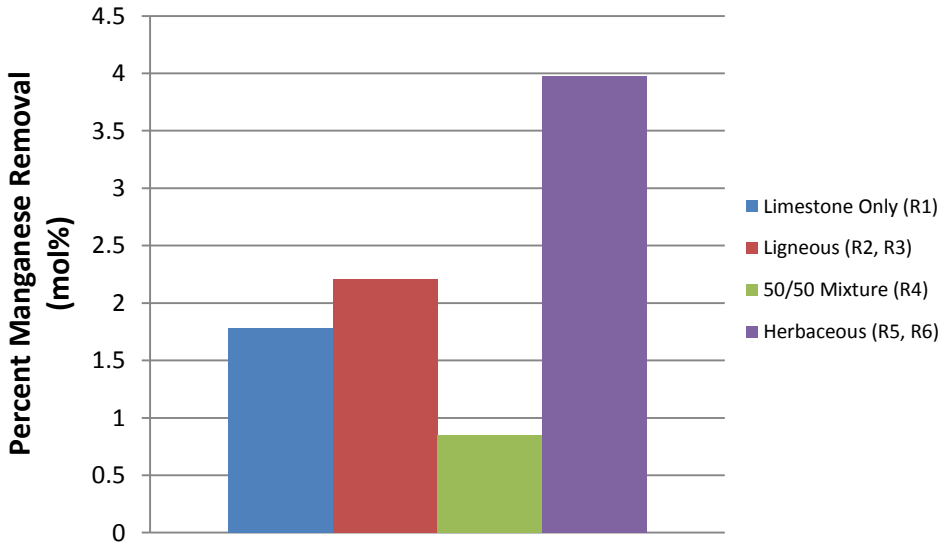

Figure 65: Overall percent manganese removal from the influent AMD in the limestone only reactor (R1; Blue Bar), ligneous reactors (R2, R3; Red Bar), 50/50 mixture (R4; Green Bar) and herbaceous reactors (R5, R6; Purple Bar) during the course of this experiment.

In summation Table 3 lists the calculated averages in pH values, percent removal of iron, sulfate, aluminum, manganese, nickel, zinc, copper and cadmium along with the alkalinity produced for each bioreactor category. Parameters were then ranked as first, second and third by comparing each bioreactor performance in improving AMD parameters against one another. Of the ten parameters, the dominantly herbaceous reactors (R5, R6) ranked 1st in eight cases, and thus is determined as the top overall compost type in terms of AMD remediation efficacy. As for the dominantly ligneous (R2, R3) and 50/50 mixture (R4) reactors, subtle variations in many parameters (i.e. sulfate, aluminum and zinc removal) made it difficult to distinguish a clear rank between these compost types. Yet, comparison of these two reactor types depicts the 50/50 mixture ranking (R4) higher than the ligneous (R2, R3) in 6 out of 10 parameters. Therefore, in total the 50/50 mixture (R4) rank 2nd while an overall 3rd rank was appropriated to the dominantly ligneous reactors (R2, R3).

Table 3: Bioreactor Performance Based on Substrate Composition

Parameter	Ligneous (R2, R3)	50/50 Mix (R4)	Herbaceous (R5, R6)
pH	4.77	4.98	5.11
Iron Removal*	38.92	40.60	55.08
Sulfate Removal*	28.49	29.34	34.40
Aluminum Removal*	83.24	83.65	91.08
Manganese Removal*	2.2	0.85	4.0
Nickel Removal*	69.55	73.81	73.81
Zinc Removal*	87.87	87.48	85.13
Copper Removal*	77.87	81.80	84.78
Cadmium Removal*	93.32	82.73	91.20
Alkalinity (meq as $CaCO_3$)	369.14	317.48	436.70
Overall Rank	3rd	2nd	1st

*Removal is calculated from the average removal % (mol%) from the influent AMD for each reactor type during the course of the experiment.

4.4. Extrapolation of Experimental Results to the Tab-Simco Remediation System

To examine the impact of increasing the herbaceous content in compost used for full-scale ASRB systems, the overall removal percentages documented for each reactor type was applied to the contaminant loads exhibited at the Tab-Simco site. Previous studies have documented an average influent AMD flow-rates experienced at the Tab-Simco site of 1.35 liters per second (L/s) (Behum et al., 2011). Considering the duration of the present study was 377 days (i.e. August 23, 2012- September 5, 2013), the volume of AMD passing through the full-scale bioreactor can be calculated as followed (eq.16):

$$(1.35L/s)*(60s/min.)*(60min./hr.)*(24hr./day)*(377day/exp.) = 4.3973 \times 10^7 \text{ L AMD} \quad (16)$$

The average concentration of each chemical species measured in the AMD influent (Table 4) during this experiment can then be multiplied by the calculated volume of AMD entering the full-scale bioreactor at Tab-Simco (i.e. 4.3973×10^7 L AMD). As a result the amount of contaminants expelled at the Tab-Simco site over 377-days can be expressed in kilograms (Table 5).

By applying the overall removal percentage document in each bioreactor type (Table 3), differences in the amount of contaminant removal can then be compared. Table 5 identifies that in a full-scale ASRB, by using dominantly herbaceous substrate over ligneous substrate as the organic material would correspond to an additional removal of ~13,000 kg SO_4^{2-}, ~6,000 kg Fe and ~700 kg Al after 377 days of active remediation. Therefore, results in this experiment have determined that over the same period of time, increasing herbaceous content in a bioreactor could dramatically increase the overall treatment capacity when compared to a bioreactor that is dominated by ligneous material.

Table 4: Average Contaminant Concentrations in AMD Influent at Tab-Simco AML Site

Contaminant	Sulfate*	Iron	Aluminum	Zinc	Cadmium	Nickel	Copper	Manganese
Concentration (mg/L)	5000	900	200	3.30	0.02	2.00	0.04	44

*Concentrations averaged from AMD influent values sampled over the course of this experiment.

Table 5: Contaminants Expelled at Tab-Simco vs. Full-Scale Removal based on Substrate Composition

Contaminant	Tab-Simco (kg)*	Ligneous Removal(kg)**	50/50 Mixture Removal (kg)**	Herbaceous Removal (kg)**
Sulfate	**219866.40**	**62639.94**	**64508.80**	**75634.04**
Iron	**39575.95**	**15402.96**	**16067.84**	**21798.43**
Aluminum	**8794.66**	**7320.67**	**7356.73**	**8010.17**
Zinc	**145.11**	**127.51**	**126.94**	**123.53**
Cadmium	**0.88**	**0.82**	**0.73**	**0.80**
Nickel	**87.95**	**61.17**	**64.91**	**64.91**
Copper	**1.76**	**1.37**	**1.44**	**1.49**
Manganese	**1934.82**	**42.57**	**16.45**	**77.39**

*Contaminants expelled (kg) at Tab-Simco were calculated using flow rates from Behum, 2011 and applied to the average concentration measured over the course of the 377-day experiment.

**Full-scale ASRB removal of contaminants were based on the average removal percentages documented in each reactor type (i.e. ligneous (R2, R3); 50/50 mixture (R4); herbaceous (R5, R6)) over the course of the 377-day experiment.

CHAPTER 5

CONCLUSIONS & IMPLICATIONS

Field experiments testing the efficacy of anaerobic sulfate reducing bioreactors (ASRB) have exposed variability in geochemical parameters related to seasonal transitions in the mid-western United States. Natural conditions cannot be properly mimicked in a laboratory setting which causes significant discrepancies between results obtained in laboratory tests and field scenarios. Most notably, as these experiments have shown the formation of redox gradients, from the upper to lower portions of the bioreactors (R2-R6) display distinct biochemical processes in the oxidizing and reducing parts of the experimental system. These are conditions that have not been reproduced in previous laboratory experiments. Most experiments involved anoxic environments, closed-systems, static conditions, constant temperatures and minimal exposure to UV-light (Bernardez et al., 2012; Clyde, Champagne, & Jamieson, 2010; Coggon et al., 2012; Robinson-Lora & Brennan, 2010). Although previous lab-scale experiments have provided insight into important mechanisms for the remediation of AMD, the results of this field study indicates that the aqueous environments of passive-flow ASRB's do not progress towards steady-state conditions. Since these systems evolve temporally and changes in biochemical conditions occur, it is unrealistic to infer, as previous 3-6 months laboratory studies have shown, that a permanent sink for pH and redox sensitive mineral phases (i.e. iron oxyhydroxides and iron sulfides) will develop.

Reactors used in these experiments had total heights of 89 cm. (35 in.) and developed redox gradients of up to 800 mV. This experimental design may not have provided enough redox "buffering transition zone", which resulted in frequent downward movement of the oxidizing

front during the low-temperature months, causing the meta-stable redox sensitive phases to dissolve and release metals and sulfate into the environment. To abate this issue, it may be helpful to increase bioreactor depth which would decrease its' susceptibility to destabilization of redox zones induced by changes in physicochemical conditions along with decreasing microbial activity during low-temperature months.

The acid impoundments within each bioreactor generated positive increases in ORP (mV) from influent ORP (mV) values which suggest chemolithotrophic iron oxidizers are utilizing energy obtained during the oxidation of ferrous iron for growth. Although this processes is useful to form iron oxide phases by catalyzing the hydrolysis of ferric iron, ASRB technology thrives on the production of reducing environments and sequestration of sulfur and metals in sulfide phases. Therefore, developing an acid impoundment above the compost within a bioreactor negatively impacts system stability and should be avoided. To prevent the formation of acid impoundments altogether existing bioreactors such as Tab-Simco could simply lower the bioreactor pond levels near the compost interface.

Within the limestone only reactor (R1), increases in pH produced from the dissolution of limestone was ineffective for neutralization of AMD in short-term remediation. Limestone cobbles and pebbles may not provide a large surface area for reactivity and thus the accumulation of precipitate coatings within this reactor may greatly inhibit abiotic alkalinity production. In contrast, biologic reactors have shown substantial increases in pH through time which could be attributed to (1) additional compost surface area postponing immediate armoring of limestone surfaces, (2) degradation of organic material and subsequent formation of organic compounds containing functional groups of relatively weak acidity (i.e. R-COOH) and (3) depletion of free proton concentration by production of hydrogen sulfide. Nonetheless, it is

apparent that addition of compost to limestone increases neutralization capacity of the treatment system, proving it beneficial to add compost mixtures to limestone channel-ways that are used at Tab-Simco for AMD pre-treatment before entering bioreactor systems.

Reactor R1 (LS) on average had removed 44.5 mol% iron during the course of the experiment while the ligneous (R2, R3), 50/50 mix (R4) and herbaceous (R5, R6) had removed 38.9 mol%, 40.6 mol% and 55.1 mol% iron, respectively. Reactor R1 (LS) demonstrates that significant iron removal can be accomplished without a substantial increase in pH. When compared to reactor R1 (LS) the bioreactors (R2-R6) had maintained much higher pH values yet in many cases did not exhibit an increase in the overall iron removal. As a result, the mobility of iron must also correspond to the stability of the mineral phases which incorporate this element. Since reactor R1 maintained a relatively homogeneous pH and redox environment, iron phases would have not been exposed to reductive/oxidative transformations. Overall, pretreatment of iron in coal-derived AMD before entering ASRB's may be vital for improving this technology. Thus, channeling AMD into an acidic settling pond prior to bioreactor treatment would prevent large amounts of iron and aluminum oxide precipitates from entering the bioreactor without the addition of expensive chemicals.

In this experiment, biologic sulfate reduction was shown to be effected by temperature (T), with SO_4^{2-} removal and sulfide concentrations exhibiting dramatic decreases at $T < 10^0C$. At low T, abiotic processes may become the dominant mechanism of sulfate sequestration. However, decrease in precipitate-induced sulfate absorption kinetics or precipitate phase transformation may result in the release of sequestered sulfate, iron and other trace metals back into the solution. This would offer the best explanation for the decline in treatment efficiency observed in multiple samples during the low temperature months. Over the course of this

experiment, reactor R1 (LS) displayed lower overall sulfate removal when compared to the bioreactors, proving microbial mediated sulfate reduction a necessary mechanism for enhancing coal-derived AMD remediation.

Removal of trace metals such as zinc, nickel, copper and cadmium within the bioreactors (R2-R6) was greatly increased when compared to reactor R1 (LS). Geochemical modeling identifies both iron oxide intercalation and sulfide precipitation as possible sinks for these contaminants within the bioreactors. Developing both a reducing environment along with increasing pH values has shown to be important parameters for increasing the sequestration of these metals from solution. However, as the bioreactors (R2-R6) matured, removal of nickel had declined possibly due to the increase in free proton concentrations during the final months of operation. As neutralization of the AMD influent continues to diminish within the bioreactors (R2-R6) declines in the removal of the other trace metals (i.e. copper, zinc, cadmium) may ensue. Furthermore, the trace metals that have been concentrated in mineral phases within the bioreactors (R2-R6) are subject to dissociation as the acidity increases over time. This may result in plumes concentrated in trace contaminants which could be extremely detrimental to the adjacent ecosystem. To prevent this, it is important to acknowledge when the remediation efficacy of these bioreactor systems has been compromised and initiate action to rehabilitate a failing system.

Reactors dominated by herbaceous compost (R5, R6) indicated enhanced remediation efficacy during ~ 1 year of exposure to coal-derived AMD. However, abandoned mine lands (AML's) have been documented to produce acidic metal-laden waters for many century's proving 1 year of remediation to be insignificant on a relative time-scale. Therefore this study acknowledges that substrate composition has minor effect on the long-term stability of passive-

flow anaerobic sulfate reducing bioreactors. Achieving long-term remediation of coal-derived AMD using ASRB technology will require improvement of the overall design of these systems by incorporating the physicochemical responses in the aqueous environments that are outlined in this experiment.

Since many AML sites represent a unique set of chemical and physical characteristics treatment strategies must identify the contaminants of concern, mechanism for sequestration (i.e. type of precipitates formed) and the future stability of the mineral phases associated with the type of remediation. In AML sites with high iron loads multiple strategies have found success in utilizing active chemical treatment strategies (i.e. NaOH) to neutralize influent drainage inducing the formation of iron oxyhydroxides (Johnson & Hallberg, 2005). However, sulfate removal is less effective in these strategies and therefore AML sites with high sulfate loads (i.e. Tab-Simco) must incorporate microbial-induced sulfate reduction found in ASRB technology as an additional mechanism for the removal of this contaminant. Therefore to continue the advancement in passive remediation of coal-derived AMD using ASRB's, future experiments must improve system designs to account for the temporal dynamics of the biogeochemical processes that are exhibited in the AML field settings.

REFERENCES

Hach Method10244, H. M. (2011). Phenolphthalein and Total Alkalinity 10 to 4000 mg/L as CaCO 3, 1–8.

Affolter, B. R. H., & Hatch, J. R. (2002). Characterization of the Quality of Coals from the Illinois Basin, Chapter E. *Resource Assessment of the Springfield , Herrin , Danville , and Baker Coals in the Illinois Basin*, (Hatch, J.R., Affolter, R.H., Eds., USGS Professional Paper 1625-D,E1-E222.).

Amann, R., & Fuchs, B. M. (2008). Single-cell identification in microbial communities by improved fluorescence in situ hybridization techniques. *Nature reviews. Microbiology*, *6*(5), 339–48. doi:10.1038/nrmicro1888

APHA. (2005). *Standard Methods for the Examination of Water and Wastewater. Chapter 4, Inorganic Nonmetallic Constituents* (pp. 151–152).

Archer, P. (1996). Illionis Basin Report.

Behum, P. T., Kiser, R., & Lewis, L. (2010). INVESTIGATION OF THE ACID MINE DRAINAGE AT THE TAB- SIMCO MINE , ILLINOIS : OBSERVATIONS AND IMPLICATIONS FOR, 5–9.

Behum, P. T., Lefticariu, L., Bender, K. S., Segid, Y. T., Burns, A. S., & Pugh, C. W. (2011). Remediation of coal-mine drainage by a sulfate-reducing bioreactor: A case study from the Illinois coal basin, USA. *Applied Geochemistry*, *26*, S162–S166. doi:10.1016/j.apgeochem.2011.03.093

Benner, S. G., Blowes, D. W., Gould, W. D., Herbert,, R. B., & Ptacek, C. J. (1999). Geochemistry of a Permeable Reactive Barrier for Metals and Acid Mine Drainage. *Environmental Science & Technology*, *33*(16), 2793–2799. doi:10.1021/es981040u

Bernardez, L. a., de Andrade Lima, L. R. P., Ramos, C. L. S., & Almeida, P. F. (2012). A Kinetic Analysis of Microbial Sulfate Reduction in an Upflow Packed-Bed Anaerobic Bioreactor. *Mine Water and the Environment*, *31*(1), 62–68. doi:10.1007/s10230-012-0170-z

Bigham, J. M., & Nordstrom, D. K. (2000a). Iron and Aluminum Hydroxysulfates from Acid Sulfate Waters. *Reviews in Mineralogy and Geochemistry*, *40*(1), 351–403. doi:10.2138/rmg.2000.40.7

Bigham, J. M., & Nordstrom, D. K. (2000b). Iron and Aluminum Hydroxysulfates from Acid Sulfate Waters. *Reviews in Mineralogy and Geochemistry*, *40*(1), 351–403. doi:10.2138/rmg.2000.40.7

Biomedicals, M. (2013). FastDNA ® SPIN Kit for Soil, 1–16.

Blowes, D. W., Spink, L. E., Wilkin, R. T., Jewett, D. G., & Weisener, C. J. (2009). Treatment of Arsenic , Heavy Metals , and Acidity Using a Mixed, *43*(6), 1970–1976.

Burns, A. S., Pugh, C. W., Segid, Y. T., Behum, P. T., Lefticariu, L., & Bender, K. S. (2012). Performance and microbial community dynamics of a sulfate-reducing bioreactor treating coal generated acid mine drainage. *Biodegradation*, *23*(3), 415–29. doi:10.1007/s10532-011-9520-y

Christensen, B., Laake, M., & Lien, T. (1996). Treatment of Acid Mine Water by Sulfate-Reducing Bacteria; Results from a Bench Scale Experiment. *Elsevier Science*, *1354*(96), 1617–1624.

Clyde, E. J., Champagne, P., & Jamieson, H. E. (2010). The use of passive treatment alternatives for the mitigation of acidic drainage at the Williams Brother mine, California: Bench-scale study. *Applied Geochemistry*, *25*(7), 958–971. doi:10.1016/j.apgeochem.2010.04.004

Cocos, I. a, Zagury, G. J., Clément, B., & Samson, R. (2002). Multiple factor design for reactive mixture selection for use in reactive walls in mine drainage treatment. *Water research*, *36*(1), 167–77. Retrieved from http://www.ncbi.nlm.nih.gov/pubmed/11766792

Coggon, M., Becerra, C. A., Nüsslein, K., Miller, K., Yuretich, R., & Ergas, S. J. (2012). Bioavailability of jarosite for stimulating acid mine drainage attenuation. *Geochimica et Cosmochimica Acta*, *78*, 65–76. doi:10.1016/j.gca.2011.11.030

Corperation, H. H. T. (2004). *Instruction Manual for Model Z-2000 Series Polarized Zeeman Atomic Absorption Spectrophotometer*.

Daoud, J., & Karamanev, D. (2006). Formation of jarosite during Fe2+ oxidation by Acidithiobacillus ferrooxidans. *Minerals Engineering*, *19*(9), 960–967. doi:10.1016/j.mineng.2005.10.024

DeNicol, D. M., & Stapleton, M. G. (2002). Impact of acid mine drainage on benthic communities in streams: the relative roles of substratum vs. aqueous effects. *Environmental pollution (Barking, Essex : 1987)*, *119*(3), 303–15. Retrieved from http://www.ncbi.nlm.nih.gov/pubmed/12166664

Doulati Ardejani, F., Jodeiri Shokri, B., Bagheri, M., & Soleimani, E. (2010). Investigation of pyrite oxidation and acid mine drainage characterization associated with Razi active coal mine and coal washing waste dumps in the Azad shahr–Ramian region, northeast Iran. *Environmental Earth Sciences*, *61*(8), 1547–1560. doi:10.1007/s12665-010-0469-7

Edwards, K. J., Bond, P. L., Druschel, G. K., McGuire, M. M., Hamers, R. J., & Banfield, J. F. (2000). Geochemical and biological aspects of sulfide mineral dissolution: lessons from Iron Mountain, California. *Chemical Geology*, *169*(3-4), 383–397. doi:10.1016/S0009-2541(00)00216-3

Emerson, D., Fleming, E. J., & McBeth, J. M. (2010). Iron-oxidizing bacteria: an environmental and genomic perspective. *Annual review of microbiology*, *64*, 561–83. doi:10.1146/annurev.micro.112408.134208

EPA (Methods 375.3). (1978). Sulfate (Gravimetric): Method# 375.3.

Freitas, A. P. P., Schneider, I. A. H., & Schwartzbold, A. (2011). Biosorption of heavy metals by algal communities in water streams affected by the acid mine drainage in the coal-mining region of Santa Catarina state, Brazil. *Minerals Engineering*, *24*(11), 1215–1218. doi:10.1016/j.mineng.2011.04.013

FWPCA. (2002). *Federal water pollution control act* (pp. 1–234).

Gammons, C. H., Duaime, T. E., Parker, S. R., Poulson, S. R., & Kennelly, P. (2010). Geochemistry and stable isotope investigation of acid mine drainage associated with abandoned coal mines in central Montana, USA. *Chemical Geology*, *269*(1-2), 100–112. doi:10.1016/j.chemgeo.2009.05.026

Garg, S., Jiang, C., Miller, C. J., Rose, A. L., & Waite, T. D. (2013). Iron redox transformations in continuously photolyzed acidic solutions containing natural organic matter: kinetic and mechanistic insights. *Environmental science & technology*, *47*(16), 9190–7. doi:10.1021/es401087q

Gibson, G. R. (1990). Physiology and ecology of the sulphate-reducing bacteria. *The Journal of applied bacteriology*, *69*(6), 769–97. Retrieved from http://www.ncbi.nlm.nih.gov/pubmed/2286579

Gray, N. F. (1997). Environmental impact and remediation of acid mine drainage : a management problem, *30*(January 1996).

Groat, C. G. (2004). National Field Manual for the Collection of Water-Quality Data. Chapter A3, Cleaning of Equipment for Water Sampling.

Guo, Q., & Blowes, D. W. (2009). Biogeochemistry of two types of permeable reactive barriers, organic carbon and iron-bearing organic carbon for mine drainage treatment: column experiments. *Journal of contaminant hydrology*, *107*(3-4), 128–39. doi:10.1016/j.jconhyd.2009.04.008

Hanajima, D., Fukumoto, Y., Yasuda, T., Suzuki, K., Maeda, K., & Morioka, R. (2011). Bacterial community dynamics in aerated cow manure slurry at different aeration intensities. *Journal of applied microbiology*, *111*(6), 1416–25. doi:10.1111/j.1365-2672.2011.05151.x

Hanna. (2012). Instruction Manual HI 9828 (Multiparameter). Retrieved from www.hannainst.com

Harris, D. C. (2010). *Quantitative Chemical Analysis* (8th ed., p. AP10).

Hiroyoshi, N., Miki, H., Hirajimma, T., & Tsunekaw, M. (2001). Enhancement of Chalcopyrite leaching by ferrous ions in acidic ferric sulfate solutions. *Hydrometallurgy*, *60*(3), 185–187.

Hubbard, C. G., Black, S., & Coleman, M. L. (2009). Aqueous geochemistry and oxygen isotope compositions of acid mine drainage from the Río Tinto, SW Spain, highlight inconsistencies in current models. *Chemical Geology*, *265*(3-4), 321–334. doi:10.1016/j.chemgeo.2009.04.009

IDNR OSMRE. (2013). Illinois Abandoned Mine Land (AML) Reclamation Program. Retrieved from http://dnr.state.il.us/mines/aml/recpgm.htm

Johnson, D. B., & Hallberg, K. B. (2005). Acid mine drainage remediation options: a review. *The Science of the total environment*, *338*(1-2), 3–14. doi:10.1016/j.scitotenv.2004.09.002

Jolivet, J.-P., Chanéac, C., & Tronc, E. (2004a). Iron oxide chemistry. From molecular clusters to extended solid networks. *Chemical communications (Cambridge, England)*, (5), 481–7. doi:10.1039/b304532n

Jolivet, J.-P., Chanéac, C., & Tronc, E. (2004b). Iron oxide chemistry. From molecular clusters to extended solid networks. *Chemical communications (Cambridge, England)*, (5), 481–7. doi:10.1039/b304532n

Jong, T., & Parry, D. L. (2003). Removal of sulfate and heavy metals by sulfate reducing bacteria in short-term bench scale upflow anaerobic packed bed reactor runs. *Water research*, *37*(14), 3379–89. doi:10.1016/S0043-1354(03)00165-9

Kadota, H., & Ishida, Y. (1972). Production of Volatile Sulfur Compunds by Microorganisms. *Annual review of microbiology*, (16), 127–138.

Kim, J., Nielsen, U. G., & Grey, C. P. (2008). Local environments and lithium adsorption on the iron oxyhydroxides lepidocrocite (gamma-FeOOH) and goethite (alpha-FeOOH): a 2H and 7Li solid-state MAS NMR study. *Journal of the American Chemical Society*, *130*(4), 1285–95. doi:10.1021/ja0761028

Korose, C. P., & Elrick, S. D. (2010). Coal Geology of Illinois. *Keystone coal industry manual. Coal age, Jacksonville, Florida, Mining Media International*, 456–467.

Labrenz, M. (2000). Formation of Sphalerite (ZnS) Deposits in Natural Biofilms of Sulfate-Reducing Bacteria. *Science*, *290*(5497), 1744–1747. doi:10.1126/science.290.5497.1744

Lee, G., Bigham, J. M., & Faure, G. (2002). Removal of trace metals by coprecipitation with Fe, Al and Mn from natural waters contaminated with acid mine drainage in the Ducktown Mining District, Tennessee. *Applied Geochemistry*, *17*(5), 569–581. doi:10.1016/S0883-2927(01)00125-1

Lee, S. H., Doherty, T. V, Linhardt, R. J., & Dordick, J. S. (2009). Ionic liquid-mediated selective extraction of lignin from wood leading to enhanced enzymatic cellulose hydrolysis. *Biotechnology and bioengineering*, *102*(5), 1368–76. doi:10.1002/bit.22179

Lefticariu, L., Pratt, L. M., & Ripley, E. M. (2006). Mineralogic and sulfur isotopic effects accompanying oxidation of pyrite in millimolar solutions of hydrogen peroxide at temperatures from 4 to 150°C. *Geochimica et Cosmochimica Acta*, *70*(19), 4889–4905. doi:10.1016/j.gca.2006.07.026

Lindsay, M. B. J., Blowes, D. W., Ptacek, C. J., & Condon, P. D. (2011). Transport and attenuation of metal(loid)s in mine tailings amended with organic carbon: Column experiments. *Journal of contaminant hydrology*, *125*(1-4), 26–38. doi:10.1016/j.jconhyd.2011.04.004

Luan, F., Santelli, C. M., Hansel, C. M., & Burgos, W. D. (2012). Defining manganese(II) removal processes in passive coal mine drainage treatment systems through laboratory incubation experiments. *Applied Geochemistry*, *27*(8), 1567–1578. doi:10.1016/j.apgeochem.2012.03.010

Manahan, S. E. (2010). Phase Interactions in Aquatic Chemistry. In *Evrironmental Chemistry, 9th ed.* (pp. 107–108).

McCauley, C. a, O'Sullivan, A. D., Milke, M. W., Weber, P. a, & Trumm, D. a. (2009). Sulfate and metal removal in bioreactors treating acid mine drainage dominated with iron and aluminum. *Water research*, *43*(4), 961–70. doi:10.1016/j.watres.2008.11.029

Muyzer, G., & Stams, A. J. M. (2008). The ecology and biotechnology of sulphate-reducing bacteria. *Nature reviews. Microbiology*, *6*(6), 441–54. doi:10.1038/nrmicro1892

Myers, M. D. (2006). *National Field Manual for the Collection of Water-Quality Data: Chaper A4, Collection of Water Samples*.

Ňancucheo, I., Hedrich, S., & Johnson, D. (2012). New microbiological strategies that enable the selective recovery and recycling of metals from acid mine drainage and mine process waters. *Mineralogical Magazine*, *76*(7), 2683–2692. doi:10.1180/minmag.2012.076.7.04

Neculita, C.-M., Zagury, G. J., & Bussière, B. (2007). Passive treatment of acid mine drainage in bioreactors using sulfate-reducing bacteria: critical review and research needs. *Journal of environmental quality*. doi:10.2134/jeq2006.0066

Neculita, C.-M., Zagury, G. J., & Bussière, B. (2008). Effectiveness of sulfate-reducing passive bioreactors for treating highly contaminated acid mine drainage: II. Metal removal mechanisms and potential mobility. *Applied Geochemistry*, *23*(12), 3545–3560. doi:10.1016/j.apgeochem.2008.08.014

Nieto, J. M., Sarmiento, A. M., Canovas, C. R., Olias, M., & Ayora, C. (2013). Acid mine drainage in the Iberian Pyrite Belt: 1. Hydrochemical characteristics and pollutant load of the Tinto and Odiel rivers. *Environmental science and pollution research international*. doi:10.1007/s11356-013-1634-9

Nordstrom, D K, & Wilde, F. D. (2005). National Field Manual for the Collection of Water Quality Data (Vol. 2, pp. 1–22).

Nordstrom, Darrell Kirk, Alpers, C. N., Ptacek, C. J., & Blowes, D. W. (2000). Negative pH and Extremely Acidic Mine Waters from Iron Mountain, California. *Environmental Science & Technology*, *34*(2), 254–258. doi:10.1021/es990646v

Olías, M., Cánovas, C. R., Nieto, J. M., & Sarmiento, a. M. (2006). Evaluation of the dissolved contaminant load transported by the Tinto and Odiel rivers (South West Spain). *Applied Geochemistry*, *21*(10), 1733–1749. doi:10.1016/j.apgeochem.2006.05.009

Olías, M., Nieto, J. M., Sarmiento, a M., Cerón, J. C., & Cánovas, C. R. (2004). Seasonal water quality variations in a river affected by acid mine drainage: the Odiel River (South West Spain). *The Science of the total environment*, *333*(1-3), 267–81. doi:10.1016/j.scitotenv.2004.05.012

Oncel, M. S., Muhcu, a., Demirbas, E., & Kobya, M. (2013). A comparative study of chemical precipitation and electrocoagulation for treatment of coal acid drainage wastewater. *Journal of Environmental Chemical Engineering*. doi:10.1016/j.jece.2013.08.008

P., H., K., K.-N., M., L., & V.-P., S. (2002). Groundwater and surface water contamination in the area of the Hitura nickel mine, Western Finland. *Environmental Geology*, *42*(4), 313–329. doi:10.1007/s00254-002-0525-z

Priha, O., Nyyssönen, M., Bomberg, M., Laitila, A., Simell, J., Kapanen, A., & Juvonen, R. (2013). Application of denaturing high-performance liquid chromatography for monitoring sulfate-reducing bacteria in oil fields. *Applied and environmental microbiology*, *79*(17), 5186–96. doi:10.1128/AEM.01015-13

Pugh, C. W. (2013). *Effect of Substrate Composition on Microbial Diversity and Efficiency of in situ Pilot-Scale Passive Sulfate Reducing Bioreactors Treating Acid Mine Drainage*.

Rietra, R., Hiemstra, T., & van Riemsdijk WH. (1999). Sulfate Adsorption on Goethite. *Journal of colloid and interface science*, *218*(2), 511–521. doi:10.1006/jcis.1999.6408

Robinson-Lora, M. A., & Brennan, R. a. (2010). Chitin complex for the remediation of mine impacted water: Geochemistry of metal removal and comparison with other common substrates. *Applied Geochemistry*, *25*(3), 336–344. doi:10.1016/j.apgeochem.2009.11.016

Rose, S., & Ghazi, a. M. (1997). Release of Sorbed Sulfate from Iron Oxyhydroxides Precipitated from Acid Mine Drainage Associated with Coal Mining. *Environmental Science & Technology*, *31*(7), 2136–2140. doi:10.1021/es960970f

Rounds, R. S. A. (2012). *National field Maunual for the Collection of Water Quality Data. Chapter 6.6, Alkalinity and Acid Neutralizing Capacity* (Vol. 0, pp. 1–45).

Scientific, T. F. (2012). Dionex AS-DV Autosampler Operator ' s Manual, (065259).

Shange, R. S., Ankumah, R. O., Ibekwe, A. M., Zabawa, R., & Dowd, S. E. (2012). Distinct soil bacterial communities revealed under a diversely managed agroecosystem. *PloS one*, *7*(7), e40338. doi:10.1371/journal.pone.0040338

Skousen, J. (2002). OVERVIEW OF ACID MINE DRAINAGE TREATMENT WITH CHEMICALS, 1–17.

SMCRA. (1977). Surface Mining Control and Reclamation Act. *Public Law 95-87*.

SMEWW, S. M. for the E. of W. and W. W. (1980). Iron , Ferrous: 1,10-Phenanthroline Method (8146).

SMEWW, S. M. for the E. of W. and W. W. (2013). Aluminum Method 8012, 1–8.

Smith, P. A. (2002). Characterization of and Acid Mine Drainage Site in Southern Illinois. *Unpublished Work*.

USEPA. (2004). Reference Notebook, (September).

USEPA. (2013). Sulfide Methylene Blue Method (Method 8131), 1–6.

Vanholme, R., Demedts, B., Morreel, K., Ralph, J., & Boerjan, W. (2010). Lignin biosynthesis and structure. *Plant physiology*, *153*(3), 895–905. doi:10.1104/pp.110.155119

Walters, E. R., Pugh, C. W., Bender, K. S., & Lefticariu, L. (2013). Use of sulfur isotopes to quantify biological and abiotic processes contributing to sulfur cycling in an AMD treatment system Aproach & Methods Discussion & Conclusions, 62901.

Wang, H., Gong, L., Cravotta, C. a, Yang, X., Tuovinen, O. H., Dong, H., & Fu, X. (2013a). Inhibition of bacterial oxidation of ferrous iron by lead nitrate in sulfate-rich systems. *Journal of hazardous materials*, *244-245*, 718–25. doi:10.1016/j.jhazmat.2012.11.004

Wang, H., Gong, L., Cravotta, C. a, Yang, X., Tuovinen, O. H., Dong, H., & Fu, X. (2013b). Inhibition of bacterial oxidation of ferrous iron by lead nitrate in sulfate-rich systems. *Journal of hazardous materials*, *244-245*, 718–25. doi:10.1016/j.jhazmat.2012.11.004

Zagury, G. J., Neculita, C., & Management, M. W. (2007). PASSIVE TREATMENT OF ACID MINE DRAINAGE IN BIOREACTORS : SHORT REVIEW , APPLICATIONS , AND RESEARCH NEEDS, 1439–1446.

Zhang, P. C., & Sparks, D. L. (1990). Kinetics and Mechanisms of Sulfate Adsorption/Desorption on Goethite Using Pressure-Jump Relaxation, *1273*(1335), 1266–1273.

Zhu, M., Legg, B., Zhang, H., Gilbert, B., Ren, Y., Banfield, J. F., & Waychunas, G. a. (2012). Early stage formation of iron oxyhydroxides during neutralization of simulated acid mine drainage solutions. *Environmental science & technology*, *46*(15), 8140–7. doi:10.1021/es301268g

APPENDICES

Appendix Table 1: pH measurements of influent AMD and acid impoundments of each reactor (R1-R6) over the course of this experiment.

Date	Influent	Reactor R1 (LS)	Reactor R2 (10:90)	Reactor R3 (30:70)	Reactor R4 (50:50)	Reactor R5 (70:30)	Reactor R6 (90:10)
8/24/2012	2.75	2.97	2.75	2.84	2.76	2.72	2.92
8/31/2012	2.71	2.53	2.63	2.57	2.59	2.61	2.59
9/1/2012	2.89	2.67	3.01	2.82	2.99	3.04	2.73
9/12/2012	2.92	2.65	4.89	5.43	4.9	5.18	5.94
9/26/2012	2.71	2.66	2.81	4.22	4.56	3.98	5.05
10/10/2012	2.65	2.62	2.65	3.94	4.18	3.13	2.93
11/10/2012	2.74	2.55	2.47	4.52	4.21	3.18	2.64
12/10/2012	2.98	2.86	2.77	5.57	5.97	4.6	2.97
1/19/2013	2.82	2.8	3	3.57	4.16	4.64	4.47
2/4/2013	3	3.01	3.18	3.15	3.29	3.3	3.88
2/28/2013	3.18	3.14	3.12	3.2	3.95	3.53	3.24
3/23/2013	2.76	2.97	2.17	2.96	3.29	2.92	2.66
4/10/2013	2.83	2.64	2.88	2.74	2.89	2.66	2.52
4/24/2013	2.7	2.8	2.87	2.8	2.58	2.78	2.88
5/9/2013	2.82	2.71	2.78	2.61	2.59	2.42	2.81
5/23/2013	2.83	2.41	2.36	2.49	2.46	2.52	2.38
6/4/2013	2.75	2.25	2.25	2.43	2.51	2.49	2.3
6/18/2013	2.89	2.52	2.65	2.89	2.83	2.84	2.69
6/27/2013	2.83	2.47	2.38	2.93	2.61	2.57	2.46
7/6/2013	2.83	2.22	2.22	2.35	2.45	2.42	2.31
7/15/2013	2.91	2.35	2.37	2.51	2.51	2.56	2.44
7/24/2013	2.79	2.8	2.45	3.25	2.71	2.71	2.45
8/2/2013	2.52	2.41	2.34	2.88	2.55	2.62	2.45
8/13/2013	2.78	2.33	2.1	2.2	2.28	2.25	2.16
8/23/2013	2.8	2.34	2.16	2.31	2.73	2.26	2.2
9/5/2013	2.41	2.33	2.46	2.6	3.98	2.57	2.54

Appendix Table 2: pH measurements of effluent samples taken from each reactor (R1-R6) over the course of this experiment.

Date	Reactor R1 (LS)	Reactor R2 (10:90)	Reactor 3 (30:70)	Reactor R4 (50:50)	Reactor 5 (70:30)	Reactor 6 (90:10)
8/24/2012	4.06	4.83	4.87	4.63	4.36	4.68
8/31/2012	3.25	4.85	4.86	5.14	4.67	4.87
9/1/2012	3.15	4.91	4.79	5.33	4.93	4.94
9/12/2012	3.15	5.02	5.27	5.57	5.31	5.71
9/26/2012	3.37	5.46	5.4	5.78	5.41	5.83
10/10/2012	2.86	5.64	5.32	5.72	5.47	5.77
11/10/2012	2.63	5.78	5.83	5.92	5.55	5.92
12/10/2012	4.45	6.36	6.3	6.08	5.73	6.17
1/19/2013	3.37	5.45	5.53	5.58	5.73	5.99
2/4/2013	3.5	5.59	4.96	5.76	5.79	5.36
2/28/2013	4.18	6.13	5.06	6.36	6.2	6.37
3/23/2013	3.27	5.23	5.05	5.95	6.18	6.32
4/10/2013	3.27	4.4	5.13	5.85	5.73	5.83
4/24/2013	3.22	4.82	4.55	5.29	4.99	6.1
5/9/2013	3.33	4	4.45	4.54	5.47	5.51
5/23/2013	3.3	4.67	4.67	4.45	5.8	5.79
6/4/2013	3.07	3.82	4.39	4.17	5.67	4.5
6/18/2013	3.5	3.97	4.3	4.19	5.51	4.48
6/27/2013	3.27	3.91	4.32	4.17	5.14	4.28
7/6/2013	3.02	4.09	4.21	4.18	4.39	4.23
7/15/2013	3.35	4.04	4.24	4.29	4.72	4.23
7/24/2013	3.56	4.2	4.47	4.14	4.63	4.15
8/2/2013	3.38	3.98	4.47	4.05	4.96	4.03
8/13/2013	3.28	4.15	4.41	3.99	4.3	4.01
8/23/2013	2.78	3.76	4.14	3.93	3.74	3.37
9/5/2013	3.15	3.9	4.2	4.38	3.68	3.4

Appendix Table 3: Aluminum measurements of the influent AMD and the effluent samples taken from each reactor (R1-R6) over the course of this experiment.

Date	Influent AMD	Reactor R1 (LS)	Reactor R2 (10:90)	Reactor R3 (30:70)	Reactor R4 (50:50)	Reactor R5 (70:30)	Reactor R6 (90:10)
8/24/2012	241.46	59.769	90.35	84.8	84.105	49.286	104.9
8/31/2012	202.46	166.74	3.962	13.998	5.034	5.751	3.245
9/1/2012	133.52	158.23	1.092	6.469	0.738	1.456	40.976
9/12/2012	215.15	100.4	0	0	0.268	0.525	0.695
9/26/2012	254.7	190.57	0.315	0.315	0.766	0.135	0.226
10/10/2012	232.43	110.7	0	0.782	0	0	0
11/10/2012	224.826	102.82	4.992	4.784	4.056	4.992	5.408
12/10/2012	204.36	12.32	4.65	4.75	3.33	5.05	4.04
1/19/2013	198.93	135.64	4.12	3.56	4.77	3.97	4.37
2/4/2013	185.13	118.93	3.417	52.02	3.42	3.03	41.41
2/28/2013	180.336	85.28	2.91	23.348	0.676	0.988	1.196
3/23/2013	197.68	91.7	14.54	15.414	2.57	17.22	0.546
4/10/2013	191.58	89.15	16.12	0.18	0.4	0.19	0.3
4/24/2013	199.07	154.13	48.04	89.04	7.64	16.24	2.47
5/9/2013	165.74	125.64	106.883	31.91	47.24	1.25	3.72
5/23/2013	181.5	108.47	21.11	15.68	50.451	0.58	4.22
6/4/2013	179.68	143.02	87.033	47.034	71.958	3.115	31.36
6/18/2013	203.959	144.632	124.821	52.662	102.309	5.9295	56.079
6/27/2013	195.222	159.378	91.053	31.658	74.973	5.276	38.391
7/6/2013	209.241	149.745	57.385	53.978	51.556	13.165	53.767
7/15/2013	154.23	102.01	50.85	70.75	44.52	3.17	58.89
7/24/2013	209.1	127.4	90.5	41.1	78.2	8.29	98.8
8/2/2013	207.252	162.41	103.92	14.82	76.99	1.46	72.188
8/13/2013	186.93	135.07	37.79	9.35	51.66	20.4	42.81

Appendix Table 4: Iron measurements of the influent AMD and the effluent samples taken from each reactor (R1-R6) over the course of this experiment.

Date	Influent AMD	Reactor R1 (LS)	Reactor R2 (10:90)	Reactor R3 (30:70)	Reactor R4 (50:50)	Reactor R5 (70:30)	Reactor R6 (90:10)
8/24/2012	1175.60	624.21	373.15	427.86	428.48	391.66	469.87
8/31/2012	920.61	612.77	592.38	343.62	81.12	278.30	405.39
9/1/2012	483.81	667.26	459.26	350.27	422.66	378.98	811.62
9/12/2012	780.56	301.84	493.24	279.62	536.58	338.36	482.90
9/26/2012	878.68	200.64	489.72	436.26	387.42	420.20	278.52
10/10/2012	839.28	444.50	372.32	518.23	264.16	336.34	291.20
11/10/2012	910.14	77.38	0.16	13.85	39.01	7.50	1.92
12/10/2012	949.40	103.02	0.93	0.19	20.96	10.26	0.26
1/19/2013	891.14	664.04	604.82	572.39	684.71	221.83	22.34
2/4/2013	765.00	567.12	642.60	926.16	695.64	440.64	540.60
2/28/2013	889.20	375.44	608.40	1074.30	621.92	387.92	901.68
3/23/2013	1049.80	214.32	613.15	866.20	650.00	648.11	818.77
4/10/2013	916.70	393.72	689.52	454.92	707.88	326.40	656.88
4/24/2013	886.41	685.41	733.65	854.25	546.72	665.31	773.85
5/9/2013	833.15	716.57	719.58	795.96	741.69	515.57	763.80
5/23/2013	958.77	514.56	436.17	681.39	657.27	239.19	474.36
6/4/2013	902.49	343.71	472.35	677.37	695.46	251.25	395.97
6/18/2013	914.25	382.59	683.20	739.08	739.08	413.86	539.08
6/27/2013	878.37	621.09	560.79	822.09	741.69	486.42	412.05
7/6/2013	1026.10	441.20	498.88	776.46	775.26	404.81	436.37
7/15/2013	971.62	254.52	312.15	535.26	536.07	244.62	236.58
7/24/2013	1071.20	935.66	522.00	879.58	562.20	411.65	356.57
8/2/2013	896.68	766.19	520.39	833.95	398.58	200.60	232.56
8/13/2013	952.94	633.15	394.36	716.16	548.93	514.56	243.61
8/23/2013	968.62	763.60	373.66	609.43	753.55	460.29	258.89
9/5/2013	909.53	383.51	275.97	679.58	673.98	379.89	157.18

Appendix Table 5: Sulfate measurements of the influent AMD and the effluent samples taken from each reactor (R1-R6) over the course of this experiment.

Date	Influent	Reactor R1 (LS)	Reactor R2 (10:90)	Reactor R3 (30:70)	Reactor R4 (50:50)	Reactor R5 (70:30)	Reactor R6 (90:10)
8/24/2012	6120.58	3128.21	2721.54	4002.46	3684.70	3696.22	4448.64
8/31/2012	5321.25	3498.72	3179.47	3310.94	3141.55	3186.70	3118.49
9/1/2012	4601.79	3497.87	3348.54	3405.10	3404.96	3104.42	3592.30
9/12/2012	5236.86	3210.71	3374.04	3380.83	2820.50	3311.11	3150.61
9/26/2012	5030.03	3164.00	2187.00	2030.00	2803.00	1829.00	2097.00
10/10/2012	5245.13	3736.56	1723.00	2246.55	1694.17	1562.00	1707.00
11/10/2012	5215.35	3787.00	1722.98	2320.58	2401.25	2366.23	2187.22
12/10/2012	5085.35	3012.70	2216.03	2311.36	2510.90	2282.26	2161.70
1/19/2013	5080.04	4817.27	4322.50	4134.92	4257.89	2875.64	3151.43
2/4/2013	4482.36	4261.46	4097.52	4252.06	4038.75	3602.12	3837.23
2/28/2013	4897.00	3818.30	3792.61	4623.05	3587.14	3236.13	3972.40
3/23/2013	4490.48	3519.84	3196.54	3818.83	3427.40	3486.99	3741.83
4/10/2013	4875.36	3728.07	3942.12	3131.36	3660.84	2821.12	3545.02
4/24/2013	4622.72	4330.06	3779.14	4116.69	3248.01	3794.04	3746.05
5/9/2013	4576.99	4394.08	4103.45	3875.94	3904.89	3292.69	3784.94
5/23/2013	4980.23	4028.25	3305.10	3669.11	3698.07	2879.03	3309.23
6/4/2013	4748.26	3967.38	3640.16	3751.84	3830.44	3011.40	3445.74
6/18/2013	4971.46	4187.73	4273.87	4045.54	4177.91	3286.07	3842.02
6/27/2013	4886.80	4466.97	3983.49	4086.90	4165.50	3433.33	3569.84
7/6/2013	4825.24	4140.10	3582.24	3971.08	3966.94	3329.92	3449.88
7/15/2013	5159.69	3875.01	3507.79	3954.53	3846.98	3201.68	3391.96
7/24/2013	5198.73	4774.28	3984.32	4368.19	4017.41	3564.04	3848.64
8/2/2013	5058.52	4609.88	3749.64	4017.18	3642.63	2992.30	3346.28
8/13/2013	4935.04	4408.19	3659.09	3741.41	3996.60	3634.39	3482.10
8/23/2013	5124.37	5051.93	4109.38	4221.33	4800.03	4005.65	3910.16
9/5/2013	4844.49	4286.77	3531.49	4095.38	4753.93	3809.32	3601.47

Appendix Table 6: ORP measurements of the influent AMD and the effluent samples taken from each reactor (R1-R6) over the course of this experiment.

Date	Influent AMD	Reactor R1 (LS)	Reactor R2 (10:90)	Reactor R3 (30:70)	Reactor R4 (50:50)	Reactor R5 (70:30)	Reactor R6 (90:10)
8/24/2012	357.4	146.8	142.8	136.8	139.8	141.1	131.7
8/31/2012	394.8	152.3	12.1	18.9	-0.1	7	-16.5
9/1/2012	68.4	156.7	-0.9	13	-0.7	7.5	-17.2
9/12/2012	39.7	68.1	-48.9	-43.3	-67.4	-50.9	-67.4
9/26/2012	58.6	76.3	-117.9	-147	-141.2	-140.3	-135.1
10/10/2012	101.4	81	-134.3	-124.1	-137.3	-120.4	-122
11/10/2012	182.3	90.2	-145	-150.8	-141	-128.4	-150.5
12/10/2012	6.5	-98.4	-165.7	-166.2	-123.02	-123.1	-170.1
1/19/2013	30.7	22.06	-91.1	-96.5	-78.5	-82.8	-110.6
2/4/2013	39.3	-0.7	-30.5	-27.4	-28.1	-28.7	-27.1
2/28/2013	404.1	335	4.6	45	-1.7	-7.8	-15.3
3/23/2013	385.9	395	-31.9	-62.9	-49.6	-76.9	-44.5
4/10/2013	333.9	315.8	-43.2	-113.8	-87.9	-117.8	-72.4
4/24/2013	341.8	337.6	-16.2	-30.8	-69.2	-77.9	-65.8
5/9/2013	340.6	276.9	-41.5	-101.7	-76.9	-133.9	-82.9
5/23/2013	351.2	320.1	-104.5	-118.2	-110.7	-163.3	-104
6/4/2013	362.1	255.7	-338.7	-404.5	-397.7	-411.8	-403.2
6/18/2013	366.8	269.9	-168.2	-198.9	-190.9	-215.8	-169.6
6/27/2013	344.6	293.3	-171	-207.1	-197.4	-223.6	-203.9
7/6/2013	366.7	337.6	-168	-187.7	-174.3	-182.4	-165.5
7/15/2013	371.1	314.2	-176.1	-190.1	-196.7	-223.6	-183
7/24/2013	367.4	250.9	-102.2	-118	-111.3	-136	-114.2
8/2/2013	370.3	88.2	-199.1	-219.7	-201.2	-237.6	-194
8/13/2013	358.8	293.17	-215.2	-293.9	-216.8	-215.6	-209
8/23/2013	380.2	354.6	-159.7	-188.2	-142.2	-152.2	-122.1
9/5/2013	468.8	356.7	-142.6	-176	-168.7	-136.2	-73.9

Appendix Table 7: ORP measurements of the acid impoundment of each reactor (R1-R6) over the course of this experiment.

Date	Reactor R1 (LS)	Reactor R2 (10:90)	Reactor R3 (30:70)	Reactor R4 (50:50)	Reactor R5 (70:30)	Reactor R6 (90:10)
8/24/2012	363.7	392.6	384.5	392.9	394.8	372.5
8/31/2012	70	39.3	89	88.8	99.4	96.1
9/1/2012	68	-31.1	23.2	-31.4	-11.4	73.2
9/12/2012	58.1	-51.3	-54.6	-59.7	-82.4	-65.9
9/26/2012	259.9	228.4	-106	-92.8	-81.3	-112.4
10/10/2012	127.2	276.1	-109.3	-95.5	62.8	182.2
11/10/2012	236.3	288.1	-128.1	-118.5	-70.5	134.4
12/10/2012	91.2	116.7	-116.5	-121.7	-114.6	9.4
1/19/2013	128.1	34.3	52.2	-34.2	-93.8	-89.2
2/4/2013	61.1	13.4	3.95	-6.1	-3.6	267.9
2/28/2013	445	451.5	400.8	335.2	390.5	408
3/23/2013	410.3	439.3	384.7	361.7	413.1	466.3
4/10/2013	433.2	396.6	416.7	408	463.6	481.6
4/24/2013	386.8	374.5	389.2	431.7	396.5	374.3
5/9/2013	400.9	381.9	402.1	411.7	472.7	380.2
5/23/2013	437.7	477.3	421.8	435	473	480.1
6/4/2013	277	421.1	400.3	401.9	422.5	450.6
6/18/2013	456.3	414.3	388.3	395	417.6	426
6/27/2013	427.5	455.7	347	412.4	433.6	473.6
7/6/2013	519.8	531.9	460.9	419.6	452.9	521.6
7/15/2013	463.6	530.6	428.3	431	447	507
7/24/2013	388.8	435.2	292.3	425	432.7	479.3
8/2/2013	413.9	442.5	340.7	459.3	521.1	522
8/13/2013	412.9	519.3	504.8	458.9	508.8	541.3
8/23/2013	407.8	520.8	432.9	383	482.2	544.4
9/5/2013	474.3	522.9	424.2	-67.9	446.8	508.7

Appendix Table 8: Sulfide measurements of the influent AMD and the effluent samples taken from each reactor (R1-R6) over the course of this experiment.

Date	Influent	Reactor 1 (LS)	Reactor 2 (10:90)	Reactor 3 (30:70)	Reactor 4 (50:50)	Reactor 5 (70:30)	Reactor 6 (90:10)
8/24/2012	0.005	0	0.002	0.005	0.002	0.001	0.003
8/31/2012	0	0.005	0.249	0.785	0.099	0.432	0.027
9/1/2012	0.004	0.007	0.288	0.795	0.108	0.576	0.028
9/12/2012	0.006	0.011	1.4	2.34	0.3	1.86	0.17
9/26/2012	0.006	0.021	0.258	3.39	0.1155	4.14766	0.1115
10/10/2012	0.0075	0.018	0.18	3.7575	0.176	4.07563	0.206
11/10/2012	0.003	0.006	1.9875	2.4	0.308	6.85	11
12/10/2012	0.005	0.049	5	15.8	0.3	0.4	19
1/19/2013	0	0.004	0.002	0.004	0.004	0	0.038
2/4/2013	0	0.001	0.001	0.026	0.004	0.003	0
2/28/2013	0.003	0.002	0.002	0.091	0.004	0.005	0.007
3/23/2013	0.001	0.005	0.009	0.088	0.005	0.003	0.003
4/10/2013	0	0.006	0.097	0.008	0.026	0.008	0.004
4/24/2013	0	0.002	0.486	0.534	0.184	0.51	0.014
5/9/2013	0.012	0.008	0.616	0.501	0.421	0.189	0.018
5/23/2013	0	0	7.46	7.14	7.2	0.55	0.005
6/4/2013	0.008	0	7.7	7.06	11.2	0.352	4.4
6/18/2013	0	0	8.28	6.72	12.78	0.668	4.63
6/27/2013	0.002	0	5.94	4.4	6.84	0.574	5.21
7/6/2013	0.002	0.004	6.7	4.94	6.48	5.72	6.23
7/15/2013	0.002	0.005	4.12	7.4	6.44	3.47	6.18
7/24/2013	0.005	0.002	9.14	5.68	9.4	7.64	6.21
8/2/2013	0.002	0.004	6.14	4.02	5.44	2.14	3.88
8/13/2013	0	0	6.34	2.8	7.28	4.94	4.94
8/23/2013	0	0.004	6.8	8.74	0.003	8.41	6.85
9/5/2013	0	0.001	10.15	6.42	1.72	8.3	5.83

Appendix Table 9: Nickel Concentrations of the influent AMD and the effluent samples taken from each reactor (R1-R6) over the course of this experiment.

Date	Influent AMD	Reactor R1 (LS)	Reactor R2 (10:90)	Reactor R3 (30:70)	Reactor R4 (50:50)	Reactor R5 (70:30)	Reactor R6 (90:10)
8/24/2012	2.729	2.597	2.125	2.181	2.209	1.948	2.358
8/31/2012	1.754	1.87	1.478	1.761	1.496	1.642	1.422
9/1/2012	1.137	1.805	1.438	1.771	1.278	1.695	1.888
9/12/2012	2.004	1.888	1.344	1.159	1.099	1.36	1.205
9/26/2012	1.813	2.22	0.571	0.116	0.026	0.153	0
10/10/2012	1.82	2.025	0.068	0.206	0.073	0.094	0
11/10/2012	2.013	3.918	0	0	0.01	0.015	0
12/10/2012	2.6185	3.119	0	0	0	0.055	0
1/19/2013	2.6485	2.623	0.255	0.046	0	0	0
2/4/2013	2.459	2.352	0.342	0.641	0.149	0.124	2.455
2/28/2013	2.615	2.584	0.05	0.564	0	0	0
3/23/2013	1.425	1.789	0.247	0.086	0.097	0.014	0
4/10/2013	2.634	2.173	0.783	0.062	0.144	0	0
4/24/2013	1.3895	1.128	0.495	0.381	0.126	0.347	0.177
5/9/2013	1.43	1.013	0.709	0.228	0.356	0.044	0.04
5/23/2013	1.438	1.201	0.26	0.067	0.202	0.06	0.084
6/4/2013	1.52	1.84	0.69	0.2	0.44	0.1	0.35
6/18/2013	1.538	1.697	0.703	0.23	0.299	0.131	0.33
6/27/2013	1.43	1.41	0.58	0.17	0.23	0.15	0.25
7/6/2013	2.488	2.613	0.667	0.232	0.286	0.226	0.402
7/15/2013	1.532	1.907	0.434	0.078	0.044	0.044	0.247
7/24/2013	3.353	2.716	1.166	0.259	0.344	0.287	0.89
8/2/2013	2.562	2.166	0.899	0.234	0.348	0.244	0.597
8/13/2013	2.266	2.082	0.75	0.264	0.472	0.477	0.681
8/23/2013	2.255	2.264	1.243	0.255	2.968	0.683	1.302
9/5/2013	2.433	3.254	1.127	0.333	0.486	0.652	1.094

Appendix Table 10: Zinc Concentrations of the influent AMD and the effluent samples taken from each reactor (R1-R6) over the course of this experiment.

Date	Influent AMD	Reactor R1 (LS)	Reactor R2 (10:90)	Reactor R3 (30:70)	Reactor R4 (50:50)	Reactor R5 (70:30)	Reactor R6 (90:10)
8/24/2012	4.202	3.177	2.363	2.112	2.271	2.273	2.304
8/31/2012	3.405	3.259	2.676	3.106	0.314	4.044	1.624
9/1/2012	2.27	3.228	1.54	2.384	1.348	3.901	2.961
9/12/2012	3.535	2.961	1.989	1.047	0.212	1.342	0.811
9/26/2012	3.538	3.27	0.207	0.117	0.076	0.103	0.09
10/10/2012	3.597	3.587	0.263	0.035	0.07	0.126	0.032
11/10/2012	3.611	3.197	1.231	0.168	0.059	0.106	0.067
12/10/2012	3.245	1.563	0.128	0.041	0.03	0.045	0.024
1/19/2013	3.0385	4.131	0.002	0.218	0.008	0.034	0.03
2/4/2013	3.104	3.449	0.06	0.179	0.026	0.087	2.224
2/28/2013	2.96	2.93	0.024	0.023	0.029	0.021	0.012
3/23/2013	3.0785	2.9555	0	0	0	0	0
4/10/2013	3.171	2.66	0	0	0	0	0
4/24/2013	3.156	3.147	0.008	0.147	0	0.04	0
5/9/2013	3.07	2.93	0.09	0	0	0	0
5/23/2013	3.3	2.78	0	0	0	0	0.05
6/4/2013	3.44	3.26	0.06	0	0	0	0
6/18/2013	3.762	3.479	0.055	0	0	0	0
6/27/2013	3.32	3.27	0	0	0	0	0
7/6/2013	3.396	3.095	0	0	0.062	0	0
7/15/2013	3.429	2.782	0	0	0	0	0.046
7/24/2013	3.676	3.212	0	0	0	0	0.145
8/2/2013	3.464	3.33	0.061	0	0.059	0	0.072
8/13/2013	3.407	3.101	0	0	0	0	0.106
8/23/2013	3.448	3.395	0.003	0.034	6.338	0.099	0.392
9/5/2013	3.43	3.348	0.088	0.051	0.029	0.094	0.334

Appendix Table 11: Dissolved Oxygen (DO) Concentrations (ppm) of the influent AMD and the acid impoundments samples taken from each reactor (R1-R6) over the course of this experiment.

Date	Influent AMD	Reactor R1 (LS)	Reactor R2 (10:90)	Reactor R3 (30:70)	Reactor R4 (50:50)	Reactor R5 (70:30)	Reactor R6 (90:10)
8/24/2012	5.83	1.25	0.51	0.42	0.86	0.12	0.18
8/31/2012	4.56	0	0	0.95	0.15	0.78	0.42
9/1/2012	2.89	0	0	0.62	0	0	0
9/12/2012	1.01	4.16	0.67	0.57	1.42	0.55	0.85
9/26/2012	1.9	1.7	0.72	0.65	1.52	1.6	0.6
10/10/2012	6.78	6.54	5.26	1.97	2.05	1.75	1.34
11/10/2012	2.15	13.8	6.52	2.38	1.56	1.89	2.58
12/10/2012	2.07	6.12	11.25	8.2	8.25	6.36	8.6
1/19/2013	2.76	16.35	7.35	6.21	10.04	4.04	1.8
2/4/2013	7.95	9.05	14.85	11.12	10.02	10.4	11
2/28/2013	9.1	13.72	15.53	15.06	12.63	12.43	10.44
3/23/2013	7.76	6.15	10.29	5.59	10.12	13.42	11.3
4/10/2013	1.54	0	0.85	0	0.64	0.27	1.36
4/24/2013	11.63	11.67	13.45	9.85	9.06	11.5	6.38
5/9/2013	7.33	2.17	5.01	1.26	1.49	1.16	4.03
5/23/2013	2.1	1.64	1.43	0.97	1.64	1.49	1.59
6/4/2013	5.55	0.48	0.54	0.4	0.34	0.44	0.32
6/18/2013	1.53	3.53	3.37	3.05	1.86	2.24	2.85
6/27/2013	2.81	2.37	2.46	2.97	2.74	2.52	2.66
7/6/2013	1.66	3.96	0.92	0.61	0.73	0.54	0.94
7/15/2013	2.35	1.35	1.24	0.48	0.38	0.29	0.38
7/24/2013	3.29	1.1	2.56	2.6	3.23	3.11	2.24
8/2/2013	1.58	1.08	1.46	1.07	1.42	2.99	6.06
8/13/2013	3.8	1.97	1.12	2.32	1.57	3.76	2.66
8/23/2013	0.42	0.87	0.47	0.4	1.25	0.54	0.37
9/5/2013	1.21	1.94	0.38	0.6	0.66	1.03	1.09

Appendix Table 12: Dissolved Oxygen (DO) Concentrations (ppm) of the and the effluent samples taken from each reactor (R1 -R6) over the course of this experiment.

Date	Reactor R1 (LS)	Reactor R2 (10:90)	Reactor R3 (30:70)	Reactor R4 (50:50)	Reactor R5 (70:30)	Reactor R6 (90:10)
8/24/2012	3	0.013	0	0	0	0
8/31/2012	1.89	0	0	0	0	0
9/1/2012	0.85	0	0	0	0	0
9/12/2012	1.2	2.71	3.7	2.63	5.28	1.52
9/26/2012	2.58	2	1.98	1.38	2.12	1.43
10/10/2012	6.75	1.91	1.76	0.67	1.98	1.34
11/10/2012	7.55	2.11	1.4	0.97	1	1.08
12/10/2012	0.9	0.63	0.5	0	0.43	0.09
1/19/2013	1.29	0.68	1.04	1.2	0.76	0.6
2/4/2013	3.19	4	3.48	2.32	3.13	2.51
2/28/2013	1.07	0.65	1.41	0.93	0.52	1.74
3/23/2013	0.32	1.72	0.72	0.66	0.69	0.51
4/10/2013	0.71	1.84	1	0.83	1.22	1.09
4/24/2013	7.95	10.07	10.07	5.05	3.25	6.75
5/9/2013	4.68	4.39	4.01	3.41	2.65	4.31
5/23/2013	1.11	1.68	3.38	3.44	2.91	4.28
6/4/2013	1.62	1.69	1.73	2.54	2.19	2.11
6/18/2013	1.58	3.94	2.74	4.41	4.21	3.93
6/27/2013	2.52	7.66	6.46	3.91	4.65	6.02
7/6/2013	0.57	1.3	0.82	1.75	2.73	2.48
7/15/2013	1.77	1.32	1.47	1.23	1.04	1.58
7/24/2013	1.28	7.29	3.79	5.15	1.76	2.37
8/2/2013	2.26	5.74	3.91	3.06	3.09	2.95
8/13/2013	2.39	3.03	1.48	1.62	4.04	1.82
8/23/2013	0.41	3.33	1.18	3.84	2.4	3.05
9/5/2013	6.32	6.46	0.63	0.22	1.8	2.26

Appendix Table 13: Manganese concentrations (ppm) of the influent AMD and the effluent samples taken from each reactor (R1-R6) over the course of this experiment.

Date	Influent AMD	Reactor R1 (LS)	Reactor R2 (10:90)	Reactor R3 (30:70)	Reactor R4 (50:50)	Reactor R5 (70:30)	Reactor R6 (90:10)
8/24/2012	48.436	43.914	47.064	47.107	51.361	54.661	56.141
8/31/2012	49.053	48.591	47.614	53.979	58.725	60.693	60.631
9/12/2012	42.29	39.382	45.322	54.75	42.88	63.624	43.534
9/26/2012	37.6	36.977	31.027	34.033	33.64	33.432	25.625
10/10/2012	41.596	41.82	35.028	38.027	35.977	36.117	34.981
11/10/2012	51.792	44.859	21.486	35.901	41.08	38.854	32.282
12/10/2012	47.59	39.107	29.29	33.229	35.653	35.633	29.431
1/19/2013	43.771	51.455	59.36	53.938	59.679	50.753	43.24
2/4/2013	42.126	48.613	50.592	46.696	48.185	45.39	43.105
2/28/2013	40.648	41.642	46.862	44.741	39.957	45.115	46.426
3/23/2013	35.6	35.8	37.6	36.6	33.8	38	37.2
4/10/2013	41.221	36.863	38.964	33.782	33.436	32.314	37.434
4/24/2013	40.471	41.112	40.492	40.713	38.565	40.527	39.646
5/9/2013	40.3305	39.4155	38.4535	39.275	39.901	38.013	38.8
5/23/2013	42.435	40.12	37.5755	38.893	39.594	33.954	37.075
6/4/2013	44.01	44.16	42.6	43.61	43.36	39.59	42.5
6/18/2013	42.642	43.627	43.706	43.359	43.942	41.09	42.413
6/27/2013	43.76	45.07	44.82	45.27	45.42	44.26	44.01
7/6/2013	43.268	42.745	42.378	43.359	43.504	41.543	41.392
7/15/2013	46.114	43.135	44.723	46.883	46.23	41.239	42.445
7/24/2013	47.874	45.854	45.647	48.562	48.16	43.496	44.16
8/2/2013	46.036	44.804	44.26	47.336	46.491	40.26	42.13
8/13/2013	44.823	43.336	41.949	45.647	43.979	42.552	39.959
8/23/2013	44.818	44.169	42.495	45.527	45.014	43.883	41.907
9/5/2013	47.019	46.673	44.622	47.789	48.211	45.587	42.978

Appendix Table 14: Copper concentrations (ppm) of the influent AMD and the effluent samples taken from each reactor (R1-R6) over the course of this experiment.

Date	Influent AMD	Reactor R1 (LS)	Reactor R2 (10:90)	Reactor R3 (30:70)	Reactor R4 (50:50)	Reactor R5 (70:30)	Reactor R6 (90:10)
8/24/2012	0.063	0.017	0.028	0.028	0.048	0.012	0.04
8/31/2012	0.036	0.018	0.014	0.06	0.041	0.076	0.014
9/1/2012	0.036	0.086	0.014	0.068	0.029	0.076	0
9/12/2012	0.023	0	0.019	0.023	0	0.029	0
9/26/2012	0.089	0.056	0	0	0	0	0
10/10/2012	0.03	0.03	0	0	0	0	0
11/10/2012	0.038	0.025	0	0	0	0	0
12/10/2012	0.0385	0	0	0	0	0	0
1/19/2013	0.037	0.045	0	0.095	0.03	0	0
2/4/2013	0.029	0	0	0	0	0	0
2/28/2013	0.044	0	0	0	0	0	0
3/23/2013	0.041	0.024	0.017	0	0	0	0
4/10/2013	0.038	0	0	0	0	0	0
4/24/2013	0.0395	0.027	0	0	0	0	0
5/9/2013	0.048	0.018	0	0	0	0	0
5/23/2013	0.045	0.011	0	0	0	0	0
6/4/2013	0.029	0.018	0	0	0	0.003	0
6/18/2013	0.037	0.024	0.011	0.011	0.014	0.004	0.014
6/27/2013	0.015	0.006	0	0.006	0	0	0.003
7/6/2013	0.032	0.028	0	0	0	0	0
7/15/2013	0.028	0.011	0	0	0	0	0
7/24/2013	0.027	0.006	0	0	0	0	0
8/2/2013	0.032	0.011	0	0	0	0	0
8/13/2013	0.015	0	0	0	0	0	0

Appendix Table 15: Cadmium concentrations (ppm) of the influent AMD and the effluent samples taken from each reactor (R1-R6) over the course of this experiment.

Date	Influent AMD	Reactor R1 (LS)	Reactor R2 (10:90)	Reactor R3 (30:70)	Reactor R4 (50:50)	Reactor R5 (70:30)	Reactor R6 (90:10)
8/24/2012	0.026	0.016	0.015	0.012	0.014	0.016	0.021
8/31/2012	0.021	0.017	0.005	0.009	0.005	0.01	0.007
9/1/2012	0.016	0.017	0.005	0.009	0.004	0.01	0.01
9/12/2012	0.019	0.01	0.004	0.006	0.003	0.007	0.003
9/26/2012	0.046	0.02	0	0	0	0	0
10/10/2012	0.017	0.008	0	0	0	0	0
11/10/2012	0.022	0.015	0	0	0	0	0
12/10/2012	0.02	0.011	0	0	0.004	0.004	0
1/19/2013	0.018	0.014	0	0	0	0	0
2/4/2013	0.018	0.013	0	0	0	0	0
2/28/2013	0.017	0.011	0	0	0	0	0
3/23/2013	0.017	0.01	0	0	0	0	0
4/10/2013	0.0195	0.013	0	0	0	0	0
4/24/2013	0.018	0.017	0	0	0	0	0
5/9/2013	0.02	0.02	0	0	0	0	0
5/23/2013	0.02	0.02	0	0	0	0	0
6/4/2013	0.016	0.013	0	0	0	0	0
6/18/2013	0.017	0.013	0	0	0	0	0
6/27/2013	0.017	0.013	0	0	0	0	0
7/6/2013	0.019	0.016	0.004	0.003	0.004	0.004	0.003
7/15/2013	0.016	0.009	0	0	0	0	0
7/24/2013	0.017	0.014	0	0	0	0	0
8/2/2013	0.018	0.014	0	0	0	0	0
8/13/2013	0.015	0.013	0	0	0	0	0
8/23/2013	0.019	0.017	0	0	0.055	0	0
9/5/2013	0.018	0.017	0	0	0	0	0

Appendix Table 16: Calcium concentrations (ppm) of the influent AMD and the effluent samples taken from each reactor (R1-R6) over the course of this experiment.

Date	Influent AMD	Reactor R1 (LS)	Reactor R2 (10:90)	Reactor R3 (30:70)	Reactor R4 (50:50)	Reactor R5 (70:30)	Reactor R6 (90:10)
8/24/2012	129.16	580.61	810.58	778.96	967.41	1012.5	768.98
8/31/2012	168.06	273.94	1163.3	2241	1869.9	2241	1161.3
9/1/2012	163.07	288.08	1157.1	2365.8	1361.4	1243.6	682.45
9/12/2012	243.54	446.16	1458.8	3063.1	913.66	3153.3	848.76
9/26/2012	171.6	269.06	640.2	706.42	584.98	748.82	478.28
10/10/2012	145.81	255.63	595.09	643.34	533.73	760.66	469.46
11/10/2012	178.88	361.92	551.2	561.6	522.08	678.08	488.8
12/10/2012	169.68	454.5	529.24	547.42	484.8	702.96	490.86
1/19/2013	201.82	319.87	548.45	563.48	539.53	541.34	517.96
2/4/2013	165.24	380.48	538.56	438.6	536.52	514.08	412.08
2/28/2013	137.28	276.64	472.16	403.52	470.08	448.04	503.36
3/23/2013	127.905	252.145	368.575	394.01	352.825	432.59	432.295
4/10/2013	168.92	365.16	493.68	514.08	507.96	505.92	532.44
4/24/2013	150.75	283.41	430.14	253.26	255.27	440.19	486.42
5/9/2013	117.585	285.17	229.14	328.64	311.55	396.98	415.07
5/23/2013	150.75	301.5	402	454.26	399.99	466.32	504.51
6/4/2013	94.47	120.6	188.94	263.31	211.05	305.52	275.37
6/18/2013	135.54	195.74	226.53	285.42	248.03	344.51	288.23
6/27/2013	106.53	184.92	209.04	293.46	285.42	369.84	321.6
7/6/2013	129.24	218.09	278.59	284.82	283.81	326.42	260.7
7/15/2013	54.361	225.63	255.07	258.29	284.82	299.49	264.72
7/24/2013	99.99	193.31	245.42	329.24	295.47	345.52	266.93
8/2/2013	141.8	219.17	250.85	350.14	288.64	369.64	337.88
8/13/2013	145.12	220.1	279.59	337.88	250.85	307.13	300.09
8/23/2013	122.61	154.17	253.86	258.89	178.89	257.28	249.64
9/5/2013	123.41	184.72	270.95	250.45	349.34	282	304.11

Appendix Table 17: Magnesium concentrations (ppm) of the influent AMD and the effluent samples taken from each reactor (R1-R6) over the course of this experiment.

Date	Influent AMD	Reactor R1 (LS)	Reactor R2 (10:90)	Reactor R3 (30:70)	Reactor R4 (50:50)	Reactor R5 (70:30)	Reactor R6 (90:10)
8/24/2012	240.35	231.92	328.43	356.51	402.06	407.47	371.28
8/31/2012	249.81	264.58	377.94	457.81	423.07	447.62	365.46
9/1/2012	178.26	264.99	382.72	458.64	419.12	395.62	218.46
9/12/2012	209.66	218.46	344.52	461.12	231.22	441.1	231
9/26/2012	199.32	219.12	221.1	246.62	203.94	229.46	188.26
10/10/2012	226.3	238.58	245.02	263.12	234.83	270.19	229.84
11/10/2012	224.64	243.36	222.56	226.72	224.64	241.28	222.56
12/10/2012	206.04	262.6	220.18	226.24	214.12	246.44	224.22
1/19/2013	188.58	279.38	320.83	280.63	314.19	327.65	304.68
2/4/2013	189.72	242.76	255	220.32	234.6	234.6	201.96
2/28/2013	187.2	222.56	245.44	214.24	201.76	253.76	226.72
3/23/2013	207.25	216.01	213.225	203	196.285	206.33	209.81
4/10/2013	200.85	210.12	201.96	191.76	185.64	191.76	212.16
4/24/2013	190.95	205.02	201	196.98	205.02	208.01	201
5/9/2013	191.455	211.05	202.01	208.04	211.05	211.05	211.05
5/23/2013	217.08	229.14	194.97	219.09	217.08	213.06	215.07
6/4/2013	211.05	257.28	223.11	225.12	219.09	225.12	227.13
6/18/2013	215.94	241.19	243.61	228.34	237.78	231.15	223.11
6/27/2013	213.06	249.24	243.21	245.22	235.17	248.21	249.24
7/6/2013	220.3	252.46	253.26	240.8	247.23	241.2	241.2
7/15/2013	215.94	247.85	252.05	238.39	242	234.37	242.41
7/24/2013	218.97	223.82	241.8	243.41	255.87	244.62	245.82
8/2/2013	217.15	232.5	242.61	257.28	262.71	252.66	259.49
8/13/2013	211.85	231.55	238.19	248.84	233.96	227.13	240.2
8/23/2013	218.09	227.73	246.43	247.63	231.35	235.97	248.21
9/5/2013	215.07	261.5	267.13	255.27	253.66	255.67	278.18

Appendix Table 18: Strontium concentrations (ppm) of the influent AMD and the effluent samples taken from each reactor (R1-R6) over the course of this experiment.

Date	Influent AMD	Reactor R1 (LS)	Reactor R2 (10:90)	Reactor R3 (30:70)	Reactor R4 (50:50)	Reactor R5 (70:30)	Reactor R6 (90:10)
8/24/2012	0.021	2.724	2.805	2.31	2.433	1.415	2.261
8/31/2012	0.032	0.42	2.812	6.364	6.163	5.05	3.505
9/1/2012	0.077	0.435	3.079	6.642	3.594	5.259	2.578
9/12/2012	0.143	2.578	7.371	13.521	4.335	11.114	4.975
9/26/2012	0.035	0.763	3.251	3.01	2.739	2.798	2.495
10/10/2012	0.026	0.369	2.82	1.84	1.945	2.914	1.774
11/10/2012	0.002	0.423	1.519	0.969	1.297	1.434	0.863
12/10/2012	0	0.949	1.373	1.068	1.097	1.828	0.903
1/19/2013	0	0.157	1.057	1.066	1.096	1.059	0.888
2/4/2013	0	0.155	0.712	0.292	0.647	0.619	0.313
2/28/2013	0	0.29	0.985	0.453	0.868	1.045	0.97
3/23/2013	0.013	0.22	0.565	0.406	0.556	0.684	0.911
4/10/2013	0	0.226	0.506	0.829	0.757	0.894	0.89
4/24/2013	0	0.132	0.386	0.256	1.074	0.392	0.801
5/9/2013	0	0.12	0.1	0.41	0.28	0.61	0.66
5/23/2013	0.015	0.27	0.57	0.7	0.42	0.86	0.94
6/4/2013	0.02	0.19	0.26	0.46	0.24	0.76	0.53
6/18/2013	0.032	0.248	0.177	0.382	0.235	0.695	0.402
6/27/2013	0.03	0.17	0.31	0.52	0.31	0.64	0.57
7/6/2013	0	0.154	0.321	0.349	0.314	0.455	0.374
7/15/2013	0	0.34	0.412	0.392	0.406	0.739	0.432
7/24/2013	0	0.13	0.202	0.406	0.344	0.453	0.3
8/2/2013	0	0.126	0.217	0.563	0.358	0.563	0.365
8/13/2013	0	0.114	0.275	0.549	0.213	0.304	0.29
8/23/2013	0	0.155	0.293	0.47	0.193	0.306	0.324
9/5/2013	0	0.214	0.444	0.394	0.397	0.425	0.545

Appendix Table 19: Alkalinity (meq as CaCO3) of the influent AMD and the effluent samples taken from each reactor (R1-R6) over the course of this experiment.

Date	Influent AMD	Reactor R1 (LS)	Reactor R2 (10:90)	Reactor R3 (30:70)	Reactor R4 (50:50)	Reactor R5 (70:30)	Reactor R6 (90:10)
8/24/2012	0	0	685	615	320	0	430
8/31/2012	0	0	1710	2135	2655	2875	1640
9/1/2012	0	0	1685	2250	2190	3050	480
9/12/2012	0	0	1400	4250	745	4220	890
9/26/2012	0	0	570	710	630	920	535
10/10/2012	0	0	610	630	395	1070	460
11/10/2012	0	0	230	215.5	197	350	227.97
12/10/2012	0	0	168	148	82	266	176
1/19/2013	0	0	221.6	261.2	282.4	838.8	593.6
2/4/2013	0	0	258.4	24	185.6	274.8	22.8
2/28/2013	0	0	92.4	23.2	241.2	435.4	225.2
3/23/2013	0	0	31.2	22.4	111.2	216.4	289.6
4/10/2013	0	0	0	142.8	90.4	299.2	303.6
4/24/2013	0	0	26.8	18.8	116.4	27.2	171.6
5/9/2013	0	0	0	0	13.2	178.4	174
5/23/2013	0	0	27.2	33.6	0	224	196.8
6/4/2013	0	0	0	0	0	194.4	0
6/18/2013	0	0	0	0	0	109.2	0
6/27/2013	0	0	0	0	0	101.2	0
7/6/2013	0	0	0	0	0	0	0
7/15/2013	0	0	0	0	0	100.4	0
7/24/2013	0	0	0	0	0	38.8	0
8/2/2013	0	0	0	0	0	102.8	0
8/13/2013	0	0	0	0	0	0	0
8/23/2013	0	0	0	0	0	0	0
9/5/2013	0	0	0	0	0	0	0

Appendix Table 20: Chloride concentrations (ppm) of the influent AMD and the effluent samples taken from each reactor (R1-R6) over the course of this experiment.

Date	Influent AMD	Reactor R1 (LS)	Reactor R2 (10:90)	Reactor R3 (30:70)	Reactor R4 (50:50)	Reactor R5 (70:30)	Reactor R6 (90:10)
8/24/2012	14.85	12.44	1298.67	2280.85	1519.36	2165.18	1992.03
8/31/2012	15.99	11.37	1184.38	3112.65	1781.80	2597.09	1386.59
9/1/2012	11.77	10.42	N/D	N/D	N/D	N/D	N/D
9/12/2012	11.77	10.42	1089.35	2290.60	256.41	2186.03	374.67
9/26/2012	13.37	11.58	181.44	395.86	79.55	523.69	93.40
10/10/2012	22.15	4.41	385.34	295.38	8.38	520.52	43.38
11/10/2012	10.97	11.46	6.04	83.74	18.49	180.21	39.81
12/10/2012	9.21	4.05	37.06	43.88	32.76	13.95	15.58
1/19/2013	67.86	33.80	185.06	93.34	84.74	208.28	99.78
2/4/2013	2.74	24.02	23.84	11.92	100.04	14.48	25.58
2/28/2013	8.49	9.83	10.54	8.70	7.87	32.97	31.04
3/23/2013	10.20	10.98	5.42	5.70	5.68	12.25	8.87
4/10/2013	10.20	9.87	7.40	30.80	7.80	11.60	10.00
4/24/2013	6.82	4.66	6.36	5.94	8.61	8.52	6.85
5/9/2013	10.54	10.22	8.50	6.32	11.25	7.55	11.27
5/23/2013	13.81	8.23	8.20	8.78	10.15	7.38	13.07
6/4/2013	13.31	11.96	12.92	12.99	16.99	17.94	49.58
6/18/2013	12.53	13.89	11.30	12.29	11.75	10.23	7.58
6/27/2013	12.76	10.85	6.36	8.11	10.24	12.52	7.15
7/6/2013	11.57	10.85	13.38	8.77	8.61	8.52	7.61
7/15/2013	11.67	10.98	11.72	8.99	11.05	8.79	10.26
7/24/2013	14.52	13.86	11.13	12.00	14.65	5.30	7.23
8/2/2013	13.95	12.72	10.64	8.19	11.63	10.00	8.71
8/13/2013	13.25	18.74	5.97	9.32	6.65	7.15	7.65
8/23/2013	10.32	9.19	12.67	8.54	10.75	14.83	6.92
9/5/2013	10.31	8.78	9.13	9.74	9.51	9.20	9.58

Appendix Table 21: Fluoride concentrations (ppm) of the influent AMD and the effluent samples taken from each reactor (R1-R6) over the course of this experiment.

Date	Influent AMD	Reactor R1 (LS)	Reactor R2 (10:90)	Reactor R3 (30:70)	Reactor R4 (50:50)	Reactor R5 (70:30)	Reactor R6 (90:10)
8/24/2012	9.20	4.63	1249.20	1867.58	1113.57	2057.86	1608.89
8/31/2012	9.72	6.58	1578.98	2314.93	2176.98	2021.57	1291.23
9/1/2012	8.29	5.45	1652.63	2267.45	2195.80	2078.97	1569.34
9/12/2012	8.29	5.45	1264.21	1564.99	1338.11	1563.32	31.87
9/26/2012	7.81	6.41	204.61	313.93	175.38	261.57	38.27
10/10/2012	18.81	3.48	0.15	178.88	167.66	358.02	27.70
11/10/2012	8.36	8.00	101.28	73.25	6.70	300.67	17.30
12/10/2012	4.69	1.92	43.08	31.29	11.02	439.64	1.92
1/19/2013	26.94	16.44	21.00	71.02	24.38	161.30	22.58
2/4/2013	0.12	9.70	14.66	0.00	21.40	6.14	14.14
2/28/2013	6.75	5.16	1.82	5.85	1.10	27.84	2.63
3/23/2013	4.52	5.86	2.04	2.65	1.26	4.64	2.22
4/10/2013	22.60	8.40	22.60	10.20	12.00	9.00	15.20
4/24/2013	7.54	6.13	5.56	6.45	9.65	9.09	8.55
5/9/2013	9.16	10.54	10.29	5.38	10.88	8.21	9.05
5/23/2013	16.13	9.80	3.23	5.70	9.75	1.60	2.14
6/4/2013	17.71	9.98	13.89	6.89	10.85	1.93	6.18
6/18/2013	17.97	13.29	11.00	9.73	12.28	2.34	5.52
6/27/2013	21.69	16.99	10.51	8.44	13.05	5.76	5.72
7/6/2013	21.07	12.92	14.66	6.71	11.02	3.97	6.76
7/15/2013	22.10	10.88	8.57	9.87	6.58	3.80	6.62
7/24/2013	8.56		13.16	13.15	13.66	4.72	3.15
8/2/2013	16.40	11.11	10.99	4.24	5.19	1.30	4.26
8/13/2013	19.57	15.99	4.22	5.13	4.96	3.46	4.24
8/23/2013	10.14	8.23	9.45	7.06	16.21	8.30	5.88
9/5/2013	10.82	11.85	9.79	9.56	8.04	9.84	6.97

Appendix Table 22: Sodium concentrations (ppm) of the influent AMD and the effluent samples taken from each reactor (R1-R6) over the course of this experiment.

Date	Influent AMD	Reactor R1 (LS)	Reactor R2 (10:90)	Reactor R3 (30:70)	Reactor R4 (50:50)	Reactor R5 (70:30)	Reactor R6 (90:10)
8/24/2012	30.08	29.61	6.48	2.25	2.36	2.32	3.07
8/31/2012	30.84	31.11	7.89	2.85	3.67	2.30	12.63
9/1/2012	16.72	29.41	283.48	631.07	233.88	549.89	25.29
9/12/2012	28.10	25.29	23.38	3.11	36.35	4.28	84.74
9/26/2012	162.36	72.16	95.04	126.50	41.14	95.48	84.92
10/10/2012	28.70	26.62	38.90	58.45	32.66	78.42	35.15
11/10/2012	33.03	31.65	33.90	50.05	36.67	72.34	50.13
12/10/2012	28.21	28.62	28.38	44.26	31.82	66.32	44.34
1/19/2013	24.74	33.13	36.29	35.83	37.08	64.67	52.10
2/4/2013	26.28	31.68	31.05	28.97	30.13	36.84	27.44
2/28/2013	47.84	27.04	29.12	27.04	22.88	33.28	24.96
3/23/2013	27.17	23.55	24.15	25.55	22.84	24.55	23.54
4/10/2013	25.92	23.58	24.50	22.11	21.64	24.50	25.36
4/24/2013	28.61	30.04	29.92	29.62	29.15	29.98	29.91
5/9/2013	25.33	25.13	25.13	26.93	25.93	26.93	26.73
5/23/2013	31.09	29.78	27.59	29.33	29.09	29.25	28.86
6/4/2013	36.12	36.92	35.76	36.92	36.22	37.12	36.57
6/18/2013	32.64	34.30	34.22	34.45	34.88	34.65	34.82
6/27/2013	36.27	36.17	38.78	36.37	36.82	35.51	37.12
7/6/2013	32.95	34.07	34.88	34.45	34.70	34.83	34.58
7/15/2013	30.41	30.90	33.17	33.57	33.37	32.36	33.12
7/24/2013	30.20	30.08	31.10	34.49	33.45	33.45	32.40
8/2/2013	30.28	30.40	31.12	33.89	33.89	33.71	33.33
8/13/2013	28.22	28.54	28.96	32.36	30.25	29.15	31.06
8/23/2013	31.55	31.92	32.78	35.66	33.58	34.07	35.05
9/5/2013	32.50	34.82	36.52	36.33	36.10	37.70	38.65

Appendix Table 23: Potassium concentrations (ppm) of the influent AMD and the effluent samples taken from each reactor (R1-R6) over the course of this experiment.

Date	Influent AMD	Reactor R1 (LS)	Reactor R2 (10:90)	Reactor R3 (30:70)	Reactor R4 (50:50)	Reactor R5 (70:30)	Reactor R6 (90:10)
8/24/2012	8.08	5.74	443.45	270.74	350.51	337.24	314.70
8/31/2012	6.91	7.00	15.76	44.23	23.78	36.19	16.90
9/1/2012	5.61	6.92	16.05	41.85	19.33	16.56	4.14
9/12/2012	3.37	3.08	566.28	2191.60	35.20	1919.10	77.88
9/26/2012	3.75	4.29	58.96	145.64	27.72	174.24	61.60
10/10/2012	4.52	4.79	37.44	104.42	30.37	170.98	49.50
11/10/2012	6.80	6.73	22.73	63.13	29.72	162.74	93.58
12/10/2012	6.71	6.12	20.77	28.47	27.69	N/D	23.80
1/19/2013	7.67	7.37	9.32	19.53	12.62	12.82	17.78
2/4/2013	6.82	7.55	8.55	9.90	23.81	31.85	19.38
2/28/2013	6.42	6.35	8.70	9.06	8.91	31.75	22.28
3/23/2013	10.19	5.75	7.12	8.36	8.27	14.63	17.16
4/10/2013	7.17	7.25	7.97	8.46	8.85	21.42	23.13
4/24/2013	7.97	8.18	8.59	8.53	8.77	10.61	12.39
5/9/2013	7.61	7.25	7.11	8.11	7.44	10.70	10.40
5/23/2013	8.07	7.33	7.03	8.84	7.81	12.68	10.88
6/4/2013	8.01	8.14	8.64	9.50	8.11	12.30	11.36
6/18/2013	8.35	8.67	9.18	9.72	9.19	12.51	11.18
6/27/2013	7.27	8.02	8.46	8.72	7.98	9.70	10.46
7/6/2013	8.30	8.31	9.05	9.00	8.85	11.00	10.87
7/15/2013	8.74	8.35	9.28	9.55	9.46	12.01	11.33
7/24/2013	8.88	8.93	9.19	9.99	9.59	12.06	10.73
8/2/2013	9.04	9.00	9.29	10.44	9.99	12.91	11.01
8/13/2013	9.04	8.80	9.35	10.23	9.20	10.88	10.21
8/23/2013	9.04	8.50	8.38	9.53	9.56	10.08	9.57
9/5/2013	7.98	7.80	8.92	9.38	9.74	10.43	9.02

VITA

Graduate School
Southern Illinois University

Evan R. Walters

ewalt@siu.edu

Southern Illinois University Carbondale
Bachelor of Science, Geology, 2011

Thesis Title:
SULFATE REDUCING BIOREACTOR DEPENDENCE ON ORGANIC SUBSTRATES FOR LONG-TERM REMEDIATION OF ACID MINE DRAINAGE: FIELD EXPERIMENTS

Major Professor: Dr. Liliana Lefticariu

Presentations:

1. Walters, E.R., Pugh, C.W., Bender, K.S., Lefticariu, L. (2012) Geochemical and microbial community dynamics of a remediation system treating coal-derived mine drainage. GSA Annual Meeting, in Charlotte, North Carolina, USA, 4–7 November 2012.

2. Lefticariu, L., Walters, E.R., Pugh, C.W., Bender, K.S. (2012) Stable isotope and microbial indicators of sulfur cycle pathways in an AMD treatment system. GSA Annual Meeting, in Charlotte, North Carolina, USA, 4–7 November 2012.

3. Behum, P.T., Lefticariu L., Walters, E.R., Kiser, R. (2013) Passive treatment of coal-mine drainage by a sulfate-reducing bioreactor in the Illinois Coal Basin. 34th West Virginia Mine Drainage Task Force Symposium, Morgantown, WV, USA, March 26-27, 2013.

4. Walters, E. R., Pugh, C. W., Bender, K. S., & Lefticariu, L. (2013) Use of sulfur isotopes to quantify biological and abiotic processes contributing to sulfur cycling in an AMD treatment system. Annual International Mine Water Association Conference – Reliable Mine Water Technology" Golden, Colorado, USA, August 5 - 9, 2013.

5. Walters, E. R., Pugh, C. W., Bender, K. S., & Lefticariu, L. (2013) Use of sulfur isotopes to quantify biological and abiotic processes contributing to sulfur cycling in an AMD treatment system. The 23rd Annual Goldschmidt Conference, Florence, Italy, August 25-30, 2013.

Publications:

6. Walters, E. R., Behum, P. T., Lefticariu, L. **(2013)** Sulfate Reducing Bioreactor Dependence on Organic Substrates for Long-Term Remediation of Acid Mine Drainage: Field Experiments. – In: Brown, A.; Figueroa, L. & Wolkersdorfer, Ch.: Reliable Mine Water Technology (Vol I). p. 747 – 748; Denver, Colorado, USA (Publication Printers).

7. Behum, P.T., Lefticariu L., Walters, E.R., Kiser, R. **(2013)** Passive treatment of coal-mine drainage by a sulfate-reducing bioreactor in the Illinois Coal Basin. Reclamation Matters, Spring 2013, 33-37.